Coherent generation and control of electro-magnetic fields in atomic systems

A thesis submitted in partial fulfilment of the requirements for the award of

DOCTOR OF PHILOSOPHY

by

Nawaz Sarif Mallick

Department of Physics
Indian Institute of Technology Guwahati
Guwahati 781039, India.

February 2020

Dedicated to my family

Declaration

I hereby declare that the contents of this thesis are original and have not been submitted for consideration for any other degree or qualification in this, or any other university. This dissertation is my own work and contains nothing which is the outcome of work done by others, except for the collaboration as specified in the text and acknowledgements.

Nawaz Sarif Mallick
February 2020

Certificate

This is to certify that the work contained in the thesis entitled "**Coherent generation and control of electro-magnetic fields in atomic systems**" submitted by Nawaz Sarif Mallick in the partial fulfillment of the requirement for the award of the degree of Doctor of Philosophy in Physics, Department of Physics, Indian Institute of Technology Guwahati, is a record of the candidate's own work carried out by him under my supervision and guidance. The matter embodied in this report has not been submitted in part or full to any other university or institute for the award of any degree.

Dr. Tarak Nath Dey
Professor
Department of Physics
Indian Institute of Technology Guwahati
Guwahati - 781039
Assam, India.

February 2020

Acknowledgements

First and foremost, I would like to thank my thesis supervisor Prof. Tarak Nath Dey for his continuous support and help throughout the period of my research. This work would not be possible without his guidance and encouragement. I am greatly indebted to him for giving me the opportunity to carry out my research work under his supervision.

I would also like to thank my doctoral committee members Dr. Malay Kumar Nandy (Chairperson), Dr. Gagan Kumar and Dr. Ashish Kumar Gupta for their insightful comments and constructive suggestions. I sincerely thank my co-author Dr. Kanhaiya Pandey for his valuable contributions and insightful discussions.

I acknowledge the computational and other facilities provided by the department and institute for smooth conduct of the research. I take this opportunity to sincerely acknowledge the financial assistance from MHRD which helped me in completing my research work successfully.

I extend my special thanks to the group members Rajitha-di, Sandeep-da and Nilamoni for their insightful discussions on different research topics. Further, I thank Rashidul-da, Kartik-da, pulak-da, Sourav-da, Robin, Indu, Gobinda for their encouragement and entertaining company during the PhD period.

Finally, I remember the blessings of my family members. I am deeply indebted to my parents and sister for their constant support, love and encouragement throughout this period.

Nawaz Sarif Mallick

Abstract

The work in this thesis deals with the coherent interaction of electro-magnetic fields with atoms. The coherent light-atom interaction induces atomic coherences among the various energy states of an atom. This induced atomic coherence can be used to control the basic properties of the medium such as absorption, dispersion and diffraction. Hence manipulation of atomic coherence is the key behind the various novel phenomena such as electro-magnetically induced transparency, electro-magnetically induced absorption, and electro-magnetically induced gain. In chapter 1, we study how the atomic coherence is utilized to manipulate the optical properties of a coherently prepared atomic medium. We discuss various essential concepts and mathematical techniques to understand the semiclassical density matrix formalism of coherent light-matter interaction. We demonstrate how to derive and solve the Hamiltonian for two-level and three-level system and extract necessary informations. The propagation of optical fields through a material medium is described by the fundamental equations of James Clerk Maxwell. Next, we present various solutions of paraxial wave equation in free-space.

In chapter 2, we present an efficient scheme for the generation and control of a non-degenerate four-wave mixing (FWM) signal in a N-type inhomogeneously broadened ^{87}Rb atomic system. We observe the propagation dynamics of the generated FWM signal along with the probe pulse under the condition of electromagnetically induced transparency. The FWM signal acquiring the scaled shape of probe field travels through the medium without changing its shape and intensity. We have also shown that a time dependent control field permits the storage and retrieval of these optical signals without losing their identity.

In chapter 3, we study the generation of orbital angular momentum (OAM) based on four-wave mixing (FWM) process in a diamond-type homogeneously broadened ^{85}Rb atomic system. We use density matrix formalism at weak field limit to explain the origin of vortex translation between different optical fields and generated signal. We show how the singularities which are omnipresent in phase of the input optical vortex beams can be profoundly mapped to atomic coherence that hold the origin of OAM translation. This translation process works well even for moderately intense probe and control field which enhances medium nonlinearity.

In chapter 4, we study a five level M-system whose two unpopulated ground states are coupled by a microwave field. The key feature which makes the M-system more efficient in comparison to routinely studied closed loop Λ-system is the absence of MW field induced population transfer even at high intensities of the latter. The limitation of closed loop Λ systems due to MW induced population redistribution among the ground states, which reduces the atomic coherences, can be overcome in the M-system. We examine lineshape of probe absorption as a function of its detuning in the presence of both control and MW fields. The MW field facilitates the narrowing of the probe absorption lineshape in M-systems which is in contrast to closed loop Λ-systems.
In chapter 5, we demonstrate an efficient scheme to build a microwave assisted optical waveguide in an inhomogeneously broadened vapor medium that is made of active ^{87}Rb atoms and inactive buffer gas atoms. We exploit the sensitive behaviour of MW field coupled between highly excited Rydberg states to create distinctly responsive and tunable atomic waveguide. The buffer gas induced collision further manipulates the features of the waveguide by widening the spatial transparency window and enhancing the contrast of the refractive index. We numerically solve Maxwell's equations to demonstrate diffractionless propagation of 5 μm narrow paraxial light beam of arbitrary mode to several Rayleigh lengths. The presence of buffer gas significantly enhances output intensity of diffraction controlled light beam from 10% to 40%.

Contents

List of figures

Chapter 1

Introduction

The coherent interaction of light fields with atoms allure significant experimental and theoretical attention over the past few decades. This coherent interaction creates a well defined phase relation among the coupled atomic states which is widely known as atomic coherence. Atomic coherence plays the key roles in precise control over the optical property of an atomic medium. The coherence in an atomic ensemble builds up in two different ways. Firstly, the coherence is induced among the energy states of a single atom and all the atoms within the ensemble behave individually. Secondly, the coherence is induced between the energy state of two or more atoms and all the atoms within the ensemble behave collectively. We can observe this atomic coherence only when it leads to quantum interference between the excitation pathways. For constructive quantum interference, the electro-magnetic (EM) field is absorbed by the atomic ensemble and is scattered immediately by the system due to the short lifetime of excited states (nano-second) in comparison to ground states lifetime (milli-second). For destructive quantum interference, the absorption of EM field is cancelled which makes an usually opaque medium transparent within a certain spectral range at the resonant frequency of a transition. This remarkable phenomena was named electromagnetically induced transparency (EIT) [1–3] by Harris and co-workers in 1990. The reason behind the cancellation of absorption in EIT can be explained with the concept of dark-state [2] which is one of the eigen state of system Hamiltonian having zero eigen value. In dressed state picture, the dark state containing a ground state and an excited state is responsible for EIT phenomenon because it does not interact with the intermediate state through the probe EM field. EIT has been studied mostly in gaseous atomic system. However, there are other platforms in which EIT phenomenon has been observed such as molecular system [4, 5], solid-state system [6, 7], superconducting system [8, 9], plasmonic system [10, 11], metamaterial system [10, 12], opto-mechanical system [13, 14], photonic crystal system [15, 16] and resonator system [17, 3].

The EIT phenomenon in atomic system has paid great attention due to its potential applications in wide variety of fields like controlling the group velocity of light [18–20], coherent storage and retrieval of light [21, 22], high resolution spectroscopy [23, 24], enhancement of third or higher-order nonlinear processes [25, 26], elimination of optical diffraction [27–29], generation of structured beam [30, 31] *etc.* Further, the study of EIT in Rydberg atomic system opens up a new avenue for coherent light-atom interaction. The properties of Rydberg atoms are exaggerated due to its large principal quantum number relative to a ground-state atoms [32]. These atoms possess large dipole moment and long radiative lifetime [32]. Rydberg atoms interact with each other due to their large dipole moment and the interaction depends on inter-atomic separation. For small separation dipole-dipole interaction dominates and for large separation Van-der-Waals interaction dominates [33]. Rydberg atom based EIT systems are employed to study photon-photon interaction via Rydberg blockade [34, 35], quantum gates [36] and photon transistor [37]. In multi-level atomic system, EIT suppresses linear susceptibility and enhances nonlinear susceptibility which conduct us to use nonlinear optical regime in the investigation of many nonlinear optical phenomena such as Kerr nonlinearity [25, 38], self-phase modulation (SPM) [39], cross-phase modulation (XPM) [40], four wave mixing (FWM) [26, 41, 42] *etc.* The EIT based FWM process generates new electromagnetic field with a new frequency from the interaction of three electromagnetic fields in nonlinear atomic system. The generation and control of FWM signal in atomic system has important applications in signal processing, optical communication as well as in quantum information science [43, 44]. Most applications of EIT has been shown in open loop atomic energy states (Λ, V, Ξ) which interact only with optical fields. The microwave (MW) coupling between the hyperfine ground states is a powerful implementation to control the EIT features of an atomic system. The amplitude, detuning and relative phase between optical and MW field modifies the EIT features which ensures various applications like subluminal to superluminal light propagation [45], efficient storage and retrieval of light pulse [46] and Raman sub-harmonics generations [47]. Therefore, the interaction of optical and MW field with the multi-level atomic system is an interesting subject for investigation.

In this thesis, we thoroughly discuss how the atomic coherence can be utilized to manipulate the optical properties of a coherently prepared atomic medium. We further study the pulse and beam propagation dynamics through the atomic medium. We demonstrate that propagation dynamics are precisely governed by the absorptive, dispersive and diffractive properties of the medium. These properties are induced into the medium by the coherent interaction of EM fields and atomic system. The whole interaction process and propagation dynamics are described by the Maxwell-Bloch equation. In the next section, we discuss some essential basic concepts and

mathematical tools to understand the semiclassical theory of light-matter interaction. We also demonstrate how to derive and solve the Hamiltonian for two-level and three-level system and extract necessary informations.

1.1 Theoretical background of light-matter interaction

In this section, we discuss the techniques required to understand the coherent light-matter interaction. We incorporate semi-classical interaction framework that perfectly handles this kind of problems. In this framework, light is described as a classical field which satisfies the Maxwell's wave equations whereas the matter is treated as a quantum system having discrete energy levels. Most of the experimental findings related to the light-matter interaction have been successfully explained using the semi-classical theory.

1.1.1 Polarization and susceptibility of the medium

Here, we study the response of an atomic ensemble placed in an electric field. The electric field distorts the positive and negative charge distribution of each individual atom. A primary measure of this distortion is the electric dipole moment ($\boldsymbol{p}$) induced in the i-th atom

$$\boldsymbol{p}_i = q_i \boldsymbol{r}_i \tag{1.1}$$

where q_i is the electric charge whose location is denoted by the position vector $\boldsymbol{r}_i$. An isolated atom does not possess permanent dipole moment because the center of the negative charge overlaps with the centre of the nuclear charge. However, the presence of an external electric field, $\mathbf{E}$ give rise to a shift in the center of the negative charges relative to the nucleus. In linear optics, the strength of the induced dipole moment is directly proportional to the electric field

$$\boldsymbol{p} = \alpha \mathbf{E} \tag{1.2}$$

where, α is the atomic polarizability. The macroscopic electric polarization, $\mathbf{P}$ is obtained by summing such dipoles over the volume V of the atomic ensemble and dividing by the volume

$$\mathbf{P} = \frac{\sum \boldsymbol{p}_i}{V} \tag{1.3}$$

Thus, the applied electric field induces the polarization in the dielectric material. In order to understand its behavior, we require a relation between the induced polarization

and the electric field. The induced polarization thoroughly depends on the strength of the electric field. In case of a weak electric field, we consider only the linear effects of the field and neglect all the higher order effects. For intense electric field, the induced polarization varies nonlinearly on the electric field amplitude. We can write total medium's polarization, $\mathbf{P}(\mathbf{r},t)$ as the sum of linear and nonlinear parts

$$\mathbf{P}(\mathbf{r},t) = \mathbf{P}_L(\mathbf{r},t) + \mathbf{P}_{NL}(\mathbf{r},t). \tag{1.4}$$

The linear and nonlinear polarizations are expressed as

$$\mathbf{P}_L = \chi^{(1)}\mathbf{E}, \tag{1.5}$$

$$\mathbf{P}_{NL} = \chi^{(2)}\mathbf{EE} + \chi^{(3)}\mathbf{EEE} + \cdots, \tag{1.6}$$

where various electric susceptibilities, $\chi^{(j)}$ correspond to linear ($j = 1$) and j^{th} order ($j = 2, 3, \cdots$) nonlinear polarizations. Now, we study these susceptibilities more closely in order to understand their significance.

First Order Susceptibility

First order susceptibility, $\chi^{(1)}$ also known as linear susceptibility. It has dominant contribution to $\mathbf{P}$. $\chi^{(1)}$ is a second rank tensor relating the three vector polarization components with the three components of the vector electric field

$$\begin{pmatrix} P_x \\ P_y \\ P_z \end{pmatrix} = \begin{pmatrix} \chi^{(1)}_{xx} & \chi^{(1)}_{xy} & \chi^{(1)}_{xz} \\ \chi^{(1)}_{yx} & \chi^{(1)}_{yy} & \chi^{(1)}_{yz} \\ \chi^{(1)}_{zx} & \chi^{(1)}_{zy} & \chi^{(1)}_{zz} \end{pmatrix} \begin{pmatrix} E_x \\ E_y \\ E_z \end{pmatrix}$$

There are nine susceptibility coefficients, $\chi^{(1)}_{ij}$ ($i, j \in \{x, y, z\}$) which can be represented in the following form

$$P_i = \sum_j \chi^{(1)}_{ij} E_j. \tag{1.7}$$

First order susceptibility, $\chi^{(1)}$ governs many important optical properties of the material such as absorption, refraction and diffraction.

Second Order Susceptibility

Second order susceptibility, $\chi^{(2)}$ is the first nonlinear term that contributes to $\mathbf{P}$. $\chi^{(2)}$ is a third rank tensor comprising of twenty seven components. In a $\chi^{(2)}$ media, the three polarization components couple with the nine components of the products of the

electric field components in the following manner

$$P_i = \sum_{jk} \chi^{(2)}_{ijk} E_j E_k. \tag{1.8}$$

Second order susceptibility, $\chi^{(2)}$ is responsible for various nonlinear effects such as second-harmonic generation and sum-frequency generation. However, $\chi^{(2)}$ exists only for media that lack an inversion symmetry.

Third Order Susceptibility

Third order susceptibility, $\chi^{(3)}$ is a fourth rank tensor with 81 coefficients. In a $\chi^{(3)}$ media, the components of polarization and field relate in the following manner

$$P_i = \sum_{jkl} \chi^{(3)}_{ijkl} E_j E_k E_l. \tag{1.9}$$

Third order susceptibility, $\chi^{(3)}$ gives rise to significant and interesting nonlinear phenomena such as third harmonic generation (THG), four-wave mixing (FWM), self-phase modulation (SPM), cross-phase modulation (XPM).

1.1.2 Atom-field interaction Hamiltonian

In this section, we study the interaction between the classical EM field and alkali metal atoms. All alkali atoms have a single valence electron in their outermost shell while inner shells are nearly filled. This makes alkali atoms to behave as a single electron atoms with an effective screened core nucleus. This single electron is bound to the nucleus by Coulomb potential $V(\mathbf{r})$. The position vector, $\mathbf{r}$ indicates the location of the electron with respect to the nucleus. In presence of $V(\mathbf{r})$, the Hamiltonian of such bound electron having mass m and charge $-e$ is expressed as

$$H_0 = \frac{\mathbf{p}^2}{2m} + V(\mathbf{r}). \tag{1.10}$$

where $\mathbf{p}$ is the canonical momentum of the electron. Now, this electron is exposed to an external classical EM field. The electric field, $\mathbf{E}$ and magnetic induction, $\mathbf{B}$ associated with the classical field can be expressed in terms of the scalar and vector potentials $\Phi(\mathbf{r}, t)$ and $\mathbf{A}(\mathbf{r}, t)$ as

$$\mathbf{E}(\mathbf{r}, t) = -\nabla\Phi(\mathbf{r}, t) - \frac{1}{c}\frac{\partial}{\partial t}\mathbf{A}(\mathbf{r}, t), \tag{1.11}$$

$$\mathbf{B}(\mathbf{r}, t) = \nabla \times \mathbf{A}(\mathbf{r}, t). \tag{1.12}$$

We use Eq. (1.11) and Eq. (1.12) to obtain the Lorentz force

$$F = -e[\mathbf{E} + \frac{1}{c}(\mathbf{v} \times \mathbf{B})]. \tag{1.13}$$

Next, we find the following modified Hamiltonian from the Lorentz force Eq. (1.13) and classical Lagrange's equation

$$H^{'} = \frac{1}{2m}\left[\mathbf{p} + \frac{e}{c}\mathbf{A}(\mathbf{r},t)\right]^2 - e\Phi(\mathbf{r},t). \tag{1.14}$$

The total Hamiltonian of atom-field system in the presence of a classical EM field takes the following form

$$H = \frac{1}{2m}\left[\mathbf{p} + \frac{e}{c}\mathbf{A}(\mathbf{r},t)\right]^2 - e\Phi(\mathbf{r},t) + V(\mathbf{r}). \tag{1.15}$$

We carry out quantization of Eq. (1.15) by replacing the classical variable with the corresponding quantum operator. Therefore, momentum, $\mathbf{p}$ is replaced by the momentum operator, $\hat{\mathbf{p}} = -i\hbar\nabla$ where $\hbar = h/2\pi$ is the reduced Planck's constant. Now, we derive the same Hamiltonian for a quantum system under the condition of gauge invariance. The dynamics of a quantum system is described by the non-relativistic Schrödinger equation

$$i\hbar\frac{\partial}{\partial t}\Psi(\mathbf{r},t) = H_0\Psi(\mathbf{r},t), \tag{1.16}$$

where $\Psi(\mathbf{r},t)$ is the wave function of the quantum system and the quantity, $|\Psi(\mathbf{r},t)|^2$ represents the probability density of finding an electron at position $\mathbf{r}$ and time t. The motion of an electron in presence of $V(\mathbf{r})$ is described by

$$i\hbar\frac{\partial}{\partial t}\Psi(\mathbf{r},t) = \left[\frac{-\hbar^2}{2m}\nabla^2 + V(\mathbf{r})\right]\Psi(\mathbf{r},t). \tag{1.17}$$

The standard solution of Eq. (1.17) can be written as

$$\Psi(\mathbf{r},t) = \psi(\mathbf{r},t)e^{i\chi}, \tag{1.18}$$

where χ is an arbitrary scalar function. This type of solution does not influence the probability density, $|\Psi(\mathbf{r},t)|^2$. However, if the phase part is a function of both space and time *i.e.* $\chi(\mathbf{r},t)$, then the solution

$$\Psi(\mathbf{r},t) = \psi(\mathbf{r},t)e^{i\chi(\mathbf{r},t)} \tag{1.19}$$

does not satisfy the Schrödinger Eq. (1.16). But the probability density, $|\Psi(\mathbf{r},t)|^2$ still remains invariant. Therefore, we must transform the Schrödinger equation in order to achieve phase invariance. The transformed Schrödinger equation is given by

$$i\hbar\frac{\partial}{\partial t}\Psi(\mathbf{r},t) = \left\{\frac{1}{2m}\left[-i\hbar\nabla + \frac{e}{c}\mathbf{A}(\mathbf{r},t)\right]^2 - e\Phi(\mathbf{r},t) + V(\mathbf{r})\right\}\Psi(\mathbf{r},t), \tag{1.20}$$

where $\Phi(\mathbf{r},t)$ and $\mathbf{A}(\mathbf{r},t)$ are scalar and vector potential of the external EM field respectively. Eq. (1.20) remains invariant under the following gauge transformation of $\Phi(\mathbf{r},t)$ and $\mathbf{A}(\mathbf{r},t)$

$$\Phi(\mathbf{r},t) \rightarrow \Phi^{'}(\mathbf{r},t) = \Phi(\mathbf{r},t) + \frac{\hbar}{e}\frac{\partial\chi(\mathbf{r},t)}{\partial t}, \tag{1.21}$$

$$\mathbf{A}(\mathbf{r},t) \rightarrow \mathbf{A}^{'}(\mathbf{r},t) = \mathbf{A}(\mathbf{r},t) - \frac{\hbar c}{e}\nabla\chi(\mathbf{r},t). \tag{1.22}$$

We further simplify (Eq. 1.20) using the Coulomb gauge condition *i.e.* $\Phi(\mathbf{r},t) = 0$ and $\nabla\cdot\mathbf{A}(\mathbf{r},t) = 0$. The total Hamiltonian under the gauge condition reduces to

$$\hat{H} = -\frac{\hbar^2}{2m}\nabla^2 + V(\mathbf{r}) - \frac{ie\hbar}{2mc}\mathbf{A}(\mathbf{r},t)\cdot\nabla + \frac{e^2}{2mc^2}\mathbf{A}(\mathbf{r},t)\cdot\mathbf{A}(\mathbf{r},t). \tag{1.23}$$

In Eq. (1.23), $-(\hbar^2/2m)\nabla^2$ is the kinetic energy operator and $V(\mathbf{r})$ is the Coulomb potential field experienced by the electron. The unperturbed Hamiltonian of the system is given by $H_0 = -(\hbar^2/2m)\nabla^2 + V(\mathbf{r})$. The last two terms of Eq. (1.23) represent the interaction of external EM field and atom. Next, we implement an important approximation known as "electric dipole approximation" which leads to significant simplification of the total Hamiltonian shown in Eq. (1.23).

Electric Dipole Approximation

We can express a plane electro-magnetic wave by the following form of vector potential

$$\mathbf{A}(\mathbf{r_0}+\mathbf{r},t) = \mathbf{A}(t)exp[i\mathbf{k}\cdot(\mathbf{r_0}+\mathbf{r})], \tag{1.24}$$

where $\mathbf{r_0}$ is location of nucleus of the atom. In "electric dipole approximation", we consider that the wavelength of the interacting EM field is much larger than the typical size of the atom. The mathematical representation of this approximation is given by

$$kr \ll 1 \qquad \text{where} \qquad k = \frac{2\pi}{\lambda} \tag{1.25}$$

This approximation essentially indicates that the spatial variation of EM field is nearly constant over the dimension of an atom. The typical atomic size is of the order of Bohr radius *i.e.* 0.53 Å whereas the wavelength of the EM field is 780 nm. Therefore, we can safely use the approximation to simplify our problems. The vector potential under electric dipole approximation can be written as

$$\begin{aligned}\mathbf{A}(\mathbf{r_0}+\mathbf{r},t) &= \mathbf{A}(t)exp[i\mathbf{k}\cdot(\mathbf{r_0}+\mathbf{r})], &(1.26)\\ &= \mathbf{A}(t)exp(i\mathbf{k}\cdot\mathbf{r_0})[1+i\mathbf{k}\cdot\mathbf{r}+\cdots], &(1.27)\\ &\approx \mathbf{A}(t)exp(i\mathbf{k}\cdot\mathbf{r_0}). &(1.28)\end{aligned}$$

The atom-field interaction Hamiltonian shown in Eq. (1.23) simplifies under electric dipole approximation as

$$\hat{H} = -\frac{\hbar^2}{2m}\nabla^2 + V(\mathbf{r}) - \frac{ie\hbar}{2mc}\mathbf{A}(\mathbf{r_0},t)\cdot\nabla + \frac{e^2}{2mc^2}\mathbf{A}^2(\mathbf{r_0},t). \tag{1.29}$$

We perform the following gauge transformation, $\chi(\mathbf{r},t) = -(e/\hbar c)\mathbf{A}(\mathbf{r_0},t)\cdot\mathbf{r}$ such that the wave function $\Psi(\mathbf{r},t)$ transforms into the new form

$$\Psi(\mathbf{r},t) = exp\left[-\frac{ie}{\hbar c}\mathbf{A}(\mathbf{r_0},t)\right]\psi(\mathbf{r},t). \tag{1.30}$$

We can write the electric field, $\mathbf{E}$ in terms of vector potential as

$$\mathbf{E}(\mathbf{r_0},t) = -\frac{1}{c}\frac{\partial}{\partial t}\mathbf{A}(\mathbf{r_0},t). \tag{1.31}$$

Putting all these together, we simplify the Schrödinger equation as

$$\begin{aligned}i\hbar\frac{\partial}{\partial t}\psi(\mathbf{r},t) &= \left\{-\frac{\hbar^2}{2m}\nabla^2 + V(\mathbf{r}) + e\mathbf{r}\cdot\mathbf{E}(\mathbf{r_0},t)\right\}\psi(\mathbf{r},t), &(1.32)\\ &= (H_0+H_I)\psi(\mathbf{r},t). &(1.33)\end{aligned}$$

where H_0 is the unperturbed Hamiltonian and H_I is the interaction Hamiltonian. The interaction Hamiltonian, H_I can be expressed in terms of the dipole operator, $\mathbf{d} = -e\mathbf{r}$ as

$$H_I = e\mathbf{r}\cdot\mathbf{E} = -\mathbf{d}\cdot\mathbf{E} \tag{1.34}$$

1.1.3 Density matrix formalism

Atomic ensemble is a suitable platform for the investigation of various quantum effects from both theoretical and experimental perspective. The low dephasing rate of the

induced atomic coherence makes this a well known platform. The atoms in the ensemble are treated quantum mechanically. In quantum description, each atom has discrete energy levels and each level is represented by a unique wave function, $|\psi\rangle$. The evolution of $|\psi\rangle$ corresponding to an energy state is described by the Schrödinger equation

$$i\hbar\frac{\partial|\psi\rangle}{\partial t} = H|\psi\rangle\,. \tag{1.35}$$

where H is the total Hamiltonian of the quantum system. The detail form of H is shown in the last subsection. We can extract various informations about the atomic system by solving Eq. (1.35). However, the situation gets complicated in presence of incoherent processes such as damping due to radiative and non-radiative processes. In such cases, the wave function formalism does not provide complete information about the system. The density matrix approach handles the situation in a sophisticated way than the wave function approach. Next, we discuss the basic features of density matrix formalism and how to apply this approach in light-atom interaction problem.

In this thesis, we consider an atomic ensemble in which all atoms are identical. These atoms follow the same equation of motion but thay have different stages of evolution. The density matrix operator, ρ for this ensemble of atom is described as

$$\rho = \sum_{\alpha} P_{\alpha}|\psi_{\alpha}\rangle\langle\psi_{\alpha}|\,, \tag{1.36}$$

where P_{α} represents the probability of the system to be in state $|\psi_{\alpha}\rangle$. Note that the probability parameter, P_{α} obeys the following condition

$$\sum_{\alpha} P_{\alpha} = 1. \tag{1.37}$$

The density operator shown in Eq. (1.36) is considered when we don't know which of the states $|\psi_{\alpha}\rangle$ exactly represent the system. This is an example of a mixed state. On the other hand, a pure state, $|\psi_p\rangle$ describes the state of the system. The density operator for a pure state is given by

$$\rho = |\psi_p\rangle\langle\psi_p|\,. \tag{1.38}$$

The density matrix element $\rho_{\alpha\alpha'}$ is computed as $\rho_{\alpha\alpha'} = \langle\alpha|\rho|\alpha'\rangle$. The diagonal element $\rho_{\alpha\alpha} = \langle\alpha|\rho|\alpha\rangle$ is referred to as population in the state $|\alpha\rangle$. The off-diagonal element $\rho_{\alpha\alpha'}$ $(\alpha \neq \alpha')$ is referred to as coherence between the states $|\alpha\rangle$ and $|\alpha'\rangle$. The coherence term basically represents the relative phase information between the coupled states. If

we write the state vector as a superposition of basis states with explicit phases

$$|\psi\rangle = \sum_{\alpha} |c_\alpha| e^{i\phi_\alpha} |\alpha\rangle \,, \tag{1.39}$$

then the coherence term, $\rho_{\alpha\alpha'}$ clearly shows the relative phase

$$\rho_{\alpha\alpha'} = |c_\alpha c_{\alpha'}| e^{i(\phi_\alpha - \phi_{\alpha'})}. \tag{1.40}$$

Some important properties of density matrix operator are listed below

$$(i) \quad \text{Normalization condition : } Tr[\rho] = 1 \tag{1.41}$$

$$(ii) \quad \text{For a pure state : } Tr[\rho^2] = 1 \tag{1.42}$$

$$(iii) \quad \text{For a mixed state : } Tr[\rho^2] < 1 \tag{1.43}$$

Now, we discuss how to study the expectation value and time evolution using density matrix formalism. The expectation value of an observable is expressed as

$$\langle Q \rangle = \sum_{\alpha} P_\alpha \langle \psi_\alpha | Q | \psi_\alpha \rangle \,, \tag{1.44}$$

$$= \sum_{\alpha} P_\alpha \sum_{n} \langle \psi_\alpha | Q | n \rangle \langle n | \psi_\alpha \rangle \,, \tag{1.45}$$

$$= \sum_{n} \sum_{\alpha} P_\alpha \langle n | \psi_\alpha \rangle \langle \psi_\alpha | Q | n \rangle \,, \tag{1.46}$$

$$= \sum_{n} \langle n | \sum_{\alpha} P_\alpha | \psi_\alpha \rangle \langle \psi_\alpha | Q | n \rangle \,, \tag{1.47}$$

$$= \sum_{n} \langle n | \rho Q | n \rangle \,, \tag{1.48}$$

$$= Tr[\rho Q]. \tag{1.49}$$

In Eq. (1.45), we use the completeness relation, $\sum_n |n\rangle \langle n| = 1$. Eq. (1.49) is a simple form of expectation value of any observable in terms of density matrix operator. Hence, density matrix formalism is a powerful approach to pull out required information about the system without the wave function.

Liouville's equation

Liouville's equation describes the time evolution of the density matrix operator. In order to derive Liouville's equation of motion, we perform a time derivative of Eq.

(1.36) as shown below

$$\frac{\partial \rho}{\partial t} = \sum_{\alpha} P_{\alpha} \left(|\dot{\psi_{\alpha}}\rangle \langle \psi_{\alpha}| + |\psi_{\alpha}\rangle \langle \dot{\psi_{\alpha}}| \right), \tag{1.50}$$

$$= -\frac{i}{\hbar} \sum_{\alpha} P_{\alpha} \left(H |\psi_{\alpha}\rangle \langle \psi_{\alpha}| - |\psi_{\alpha}\rangle \langle \psi_{\alpha}| H \right), \tag{1.51}$$

$$= -\frac{i}{\hbar} \left(H\rho - \rho H \right), \tag{1.52}$$

$$= -\frac{i}{\hbar} [H, \rho]. \tag{1.53}$$

We obtain Eq. (1.51) using the Schrödinger equation shown in Eq. (1.35). Eq. (1.53) is known as Liouville or Von Neumann equation of motion which describes only the coherent interaction processes. In a actual system, various decay mechanisms such spontaneous emission, collisional dephasing also influence the time evolution of the density matrix operator. So we include these decay processes in the modified Liouville's equation

$$\frac{\partial \rho}{\partial t} = -\frac{i}{\hbar} [H, \rho] + \mathcal{L}\rho. \tag{1.54}$$

The last term of Eq. (1.54) *i.e.* $\mathcal{L}\rho$ is an operator which incorporates all the incoherent processes of the system. We make use of Eq. (1.54) throughout the thesis to study the dynamics of atomic coherence and population in different atom-field configurations.

1.2 Interaction of light with a two-level atomic system

In this section, we study the interaction of a single electro-magnetic field with two-level atomic system. We consider this simple atom-field configuration because it assists us to understand many essential features of coherent interaction under certain realistic approximations. An atomic system is approximated as two level system in spite of the fact that the atom possesses many discrete energy levels. A two-level atomic system is realized when the frequency of the incident electro-magnetic field is in resonance or nearly resonance with two energy levels of the atom and all other energy levels are distinctly detuned. In Fig. 1.1, we show a two-level atomic system which includes excited state $|2\rangle$ and ground state $|1\rangle$. The transition $|1\rangle \leftrightarrow |2\rangle$ is electric dipole allowed. Two states $|1\rangle$ and $|2\rangle$ are coupled by an incident electric field which is defined as

$$\mathbf{E}_p(\mathbf{r}, t) = \hat{\mathbf{e}}_p \mathcal{E}_p(\mathbf{r}) e^{i(\mathbf{k}_p \cdot \mathbf{r} - \omega_p t)} + c.c, \tag{1.55}$$

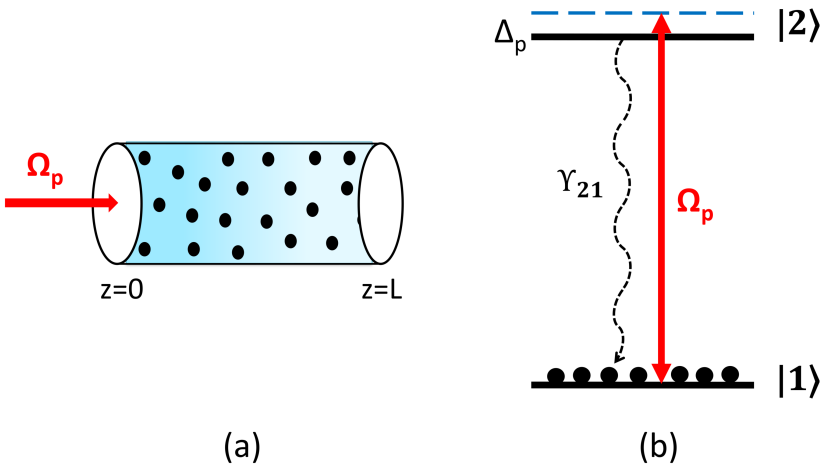

Fig. 1.1 (a) A simple interaction model of light with a two-level atomic system. (b) The energy level diagram of a two-level atomic system. The excited state $|2\rangle$ and ground state $|1\rangle$ are coupled by a monochromatic laser field Ω_p. The spontaneous decay rates from excited state to ground state is γ_{21}.

where $\hat{\mathbf{e}}_p$, $\mathcal{E}_p(\mathbf{r})$, $\mathbf{k}_p$, ω_p are the polarization unit vector, slowly varying amplitude, wave vector and frequency of the field respectively. The unperturbed Hamiltonian (H_0) of the system is given by

$$H_0 = \hbar\omega_{21} |2\rangle \langle 2| . \tag{1.56}$$

The interaction Hamiltonian (H_I) is expressed as

$$H_I = -\mathbf{d} \cdot \mathbf{E}_p(\mathbf{r}, t), \tag{1.57}$$

where $\mathbf{d}$ is electric field induced dipole moment of the system. Now we include all interaction terms and write Eq. (1.57) in the following form

$$\begin{aligned} H_I = &- \left[\mathbf{d}_{21} \cdot \hat{\mathbf{e}}_p \mathcal{E}_p(\mathbf{r}) e^{i(\mathbf{k}_p \cdot \mathbf{r} - \omega_p t)} + \mathbf{d}_{21} \cdot \hat{\mathbf{e}}_p \mathcal{E}_p^*(\mathbf{r}) e^{-i(\mathbf{k}_p \cdot \mathbf{r} - \omega_p t)}\right] |2\rangle \langle 1| \\ &- \left[\mathbf{d}_{12} \cdot \hat{\mathbf{e}}_p \mathcal{E}_p(\mathbf{r}) e^{i(\mathbf{k}_p \cdot \mathbf{r} - \omega_p t)} + \mathbf{d}_{12} \cdot \hat{\mathbf{e}}_p \mathcal{E}_p^*(\mathbf{r}) e^{-i(\mathbf{k}_p \cdot \mathbf{r} - \omega_p t)}\right] |1\rangle \langle 2| , \end{aligned} \tag{1.58}$$

where $\mathbf{d}_{ij} = \langle i| \mathbf{d} |j\rangle$ is the transition dipole moment between the states $|i\rangle \leftrightarrow |j\rangle$ and $*$ denotes the complex conjugate. Eq. (1.58) can be reshaped in the following form

$$H_I = -\left[\Omega_p e^{-i\omega_p t} + \tilde{\Omega}_p e^{i\omega_p t}\right] |2\rangle \langle 1| - \left[\Omega_p^* e^{i\omega_p t} + \tilde{\Omega}_p^* e^{-i\omega_p t}\right] |1\rangle \langle 2| , \tag{1.59}$$

where Ω_p and $\tilde{\Omega}_p$ are known as Rabi frequency. They are defined as

$$\Omega_p = \frac{\mathbf{d}_{21} \cdot \hat{\mathbf{e}}_p}{\hbar} \mathcal{E}_p(\mathbf{r}) e^{i\mathbf{k}_p \cdot \mathbf{r}}, \quad \text{and} \quad \tilde{\Omega}_p = \frac{\mathbf{d}_{21} \cdot \hat{\mathbf{e}}_p}{\hbar} \mathcal{E}_p^*(\mathbf{r}) e^{-i\mathbf{k}_p \cdot \mathbf{r}}. \tag{1.60}$$

The total Hamiltonian of the system, $H = H_0 + H_I$ is given by

$$H = \hbar\omega_{21} |2\rangle \langle 2| - \left[\Omega_p e^{-i\omega_p t} + \tilde{\Omega}_p e^{i\omega_p t}\right] |2\rangle \langle 1| - \left[\Omega_p^* e^{i\omega_p t} + \tilde{\Omega}_p^* e^{-i\omega_p t}\right] |1\rangle \langle 2| . \tag{1.61}$$

Rotating wave approximation

We use rotating wave approximation to remove the time dependence of the system Hamiltonian shown in Eq. (1.61). We perform the following unitary transformation in order to get the effective Hamiltonian, H_{eff}

$$H_{eff} = U^\dagger H U - i\hbar U^\dagger \frac{\partial U}{\partial t}, \tag{1.62}$$

where U is defined as

$$U = \hbar\omega_p |2\rangle \langle 2| . \tag{1.63}$$

Now the transformed effective Hamiltonian H_{eff} takes the following form

$$H_{eff}/\hbar = -\Delta_p |2\rangle \langle 2| - \left[\Omega_p + \tilde{\Omega}_p e^{2i\omega_p t}\right] |2\rangle \langle 1| - \left[\Omega_p^* + \tilde{\Omega}_p^* e^{-2i\omega_p t}\right] |1\rangle \langle 2| . \tag{1.64}$$

In Eq. (1.64), the term related to $\tilde{\Omega}_p$ oscillates with very high frequency *i.e.* $2\omega_p$. $\tilde{\Omega}_p$ significantly contributes in H_{eff} only when $\tilde{\Omega}_p \approx 2\omega_p$. Therefore, in optical frequency domain where $\tilde{\Omega}_p \ll 2\omega_p$, we can safely neglect $\tilde{\Omega}_p$. In optical physics, this approximation is named as rotating wave approximation (RWA). Under this approximation, the effective Hamiltonian becomes explicitly time independent as shown below

$$H_{eff} = -\hbar\Delta_p |2\rangle \langle 2| - \hbar\Omega_p |2\rangle \langle 1| - \hbar\Omega_p^* |1\rangle \langle 2| . \tag{1.65}$$

1.2.1 Dynamics of population and coherence in a two-level system

The state vector, $|\psi\rangle$ of the two-level system can be written as a linear combination of the two constituent states $|1\rangle$ and $|2\rangle$

$$|\psi\rangle = c_1 |1\rangle + c_2 |2\rangle . \tag{1.66}$$

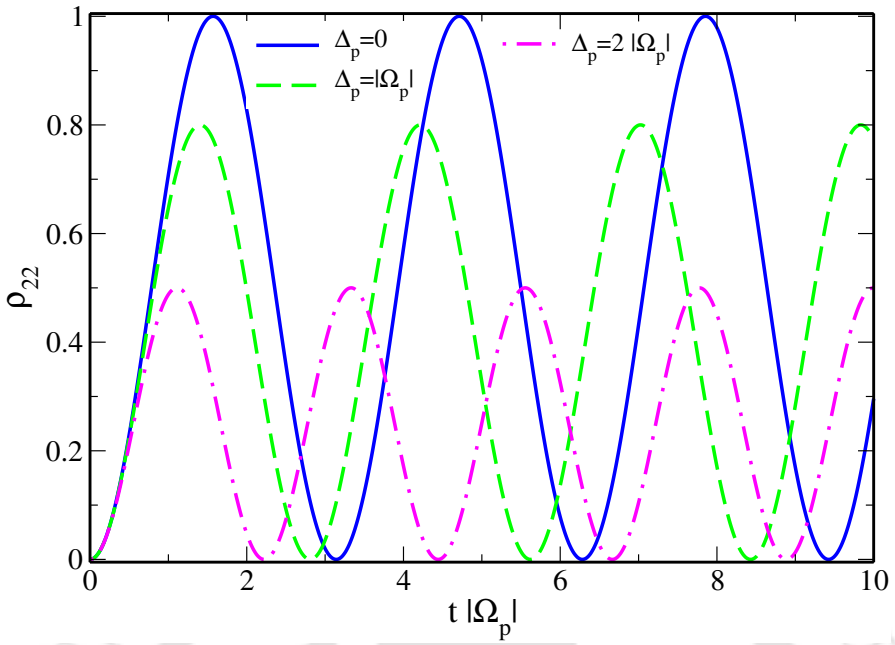

Fig. 1.2 Rabi oscillation of excited state population is plotted for three different values of probe field detuning *i.e.* $\Delta_p = 0$, $\Delta_p = |\Omega_p|$, $\Delta_p = 2|\Omega_p|$.

The density operator, ρ of the system is derived in the following way

$$\begin{aligned}\rho &= |\psi\rangle\langle\psi|, \\ &= (c_1|1\rangle + c_2|2\rangle)(c_1^*\langle 1| + c_2^*\langle 2|), \\ &= |c_1|^2|1\rangle\langle 1| + c_1c_2^*|1\rangle\langle 2| + c_1^*c_2|2\rangle\langle 1| + |c_2|^2|2\rangle\langle 2|, \\ &= \rho_{11}|1\rangle\langle 1| + \rho_{12}|1\rangle\langle 2| + \rho_{21}|2\rangle\langle 1| + \rho_{22}|2\rangle\langle 2|. \end{aligned} \tag{1.67}$$

The diagonal density matrix elements $\rho_{11} = |c_1|^2$ and $\rho_{22} = |c_2|^2$ show the population of ground state $|1\rangle$ and excited state $|2\rangle$ respectively. The off-diagonal density matrix elements $\rho_{12} = c_1c_2^*$ and $\rho_{21} = c_1^*c_2$ indicate the induced atomic coherence between the states $|1\rangle$ and $|2\rangle$.

We study the evolution of atomic populations and coherence using the following Liouville's equation

$$\frac{\partial\rho}{\partial t} = -\frac{i}{\hbar}[H_{eff}, \rho]. \tag{1.68}$$

The equation of motion for atomic population and coherence in the two-level system are given by

$$\dot{\rho}_{11} = i\Omega_p^*\rho_{21} - i\Omega_p\rho_{12}, \tag{1.69}$$

$$\dot{\rho}_{21} = i\Delta_p\rho_{21} + i\Omega_p(\rho_{11} - \rho_{22}), \tag{1.70}$$

$$\dot{\rho}_{12} = -i\Delta_p\rho_{12} - i\Omega_p^*(\rho_{11} - \rho_{22}), \tag{1.71}$$

$$\dot{\rho}_{22} = -i\Omega_p^* \rho_{21} + i\Omega_p \rho_{12}. \tag{1.72}$$

These coupled equations are known as optical Bloch equations (OBE). We obtain the solution of these coupled equations under a initial condition that atoms are initially in the ground state *i.e.* $\rho_{11}(t=0) = 1$. Now, the solutions for atomic population $\rho_{22}(t)$ and coherence $\rho_{21}(t)$ are then given by

$$\rho_{22}(t) = \frac{4|\Omega_p|^2}{\Omega^2} \sin^2\left(\frac{\Omega t}{2}\right), \tag{1.73}$$

$$\rho_{21}(t) = \frac{2|\Omega_p|}{\Omega^2} \sin\left(\frac{\Omega t}{2}\right) \left\{ \Delta_p \sin\left(\frac{\Omega t}{2}\right) + i\Omega \cos\left(\frac{\Omega t}{2}\right) \right\}, \tag{1.74}$$

where $\Omega = \sqrt{\Delta_p^2 + 4|\Omega_p|^2}$ is called the generalized Rabi frequency of the system. In Fig. 1.3, we plot the time variation of excited state population ρ_{22} for three different values of probe field detuning *i.e.* $\Delta_p = 0$, $\Delta_p = |\Omega_p|$, $\Delta_p = 2|\Omega_p|$. For $\Delta_p = 0$, the population oscillates between its maximum value $\rho_{22} = 1$ and minimum value $\rho_{22} = 0$ with oscillation frequency $\Omega = 2|\Omega_p|$. This population oscillation is called Rabi oscillation. The frequency of Rabi oscillation is enhanced with the increase of probe field detuning as shown with dashed green and dash dot magenta curve in Fig. 1.3. At the same time, the amplitude of population oscillation is reduced with the increase of Ω. The experimental observation of Rabi oscillation is recorded in Rubidium vapor using nano second pulse [48].

1.2.2 Effect of decoherence on dynamics of population and coherence

Here, we study how the decoherence of an atomic system affects the evolution of atomic population and coherence. The atoms in the system switch its energy state due to various mechanism such as spontaneous emission and collision with other atoms. These decoherence mechanisms significantly manipulate the population and induced coherence of the system. We use the following form of Liouville's equation to derive the equation of motion in two-level system

$$\frac{\partial \rho}{\partial t} = -\frac{i}{\hbar}[H_{eff}, \rho] + \mathcal{L}\rho, \tag{1.75}$$

where $\mathcal{L}\rho$ is the Liouville operator which describes various decoherence processes. For a two-level atomic system, the expression of $\mathcal{L}\rho$ is given by

$$\mathcal{L}\rho = -\frac{\gamma_{21}}{2}(|2\rangle\langle 2|\rho - 2|1\rangle\langle 1|\rho_{22} + \rho|2\rangle\langle 2|), \tag{1.76}$$

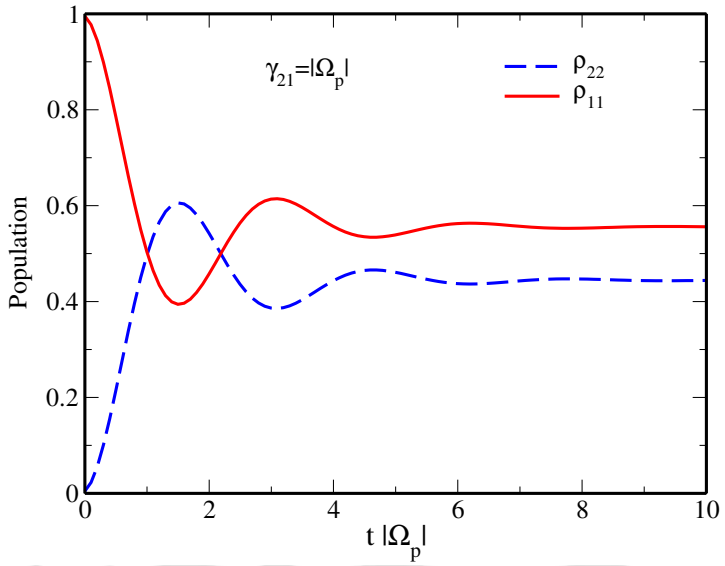

Fig. 1.3 The temporal behaviour of excited state population ρ_{22} and ground state population ρ_{11} are shown in presence of spontaneous decay.

where γ_{21} is the spontaneous decay rates from excited state $|2\rangle$ to ground state $|1\rangle$. The density matrix equations of the two-level system in presence of decoherence can be written as

$$\dot{\rho}_{11} = \gamma_{21}\rho_{22} + i\Omega_p^*\rho_{21} - i\Omega_p\rho_{12}, \tag{1.77}$$

$$\dot{\rho}_{21} = -\left(\frac{\gamma_{21}}{2} - i\Delta_p\right)\rho_{21} + i\Omega_p(\rho_{11} - \rho_{22}), \tag{1.78}$$

$$\dot{\rho}_{12} = -\left(\frac{\gamma_{21}}{2} + i\Delta_p\right)\rho_{12} - i\Omega_p^*(\rho_{11} - \rho_{22}), \tag{1.79}$$

$$\dot{\rho}_{22} = -\gamma_{21}\rho_{22} - i\Omega_p^*\rho_{21} + i\Omega_p\rho_{12}. \tag{1.80}$$

The presence of decoherence restricts the pure oscillatory behavior of the atomic population and drives the system in a steady state after a certain interaction time $t \gg 1/\gamma_{21}$. In Fig. 1.3, we show the temporal behaviour of excited state population ρ_{22} and ground state population ρ_{11} in presence of spontaneous decay. Fig. 1.3 clearly demonstrates that population oscillation of both the states attain a constant value after a certain time. Next, we study the two-level system under this steady state condition *i.e.* $\dot{\rho}_{ij} = 0$. The exact solution of population ρ_{22} and coherence ρ_{21} in steady state are given by

$$\rho_{22} = \frac{4|\Omega_p|^2}{(\gamma_{21}^2 + 4\Delta_p^2) + 8|\Omega_p|^2}, \tag{1.81}$$

$$\rho_{21} = \frac{i\Omega_p(2\gamma_{21} + i\,4\Delta_p)}{(\gamma_{21}^2 + 4\Delta_p^2) + 8|\Omega_p|^2}. \tag{1.82}$$

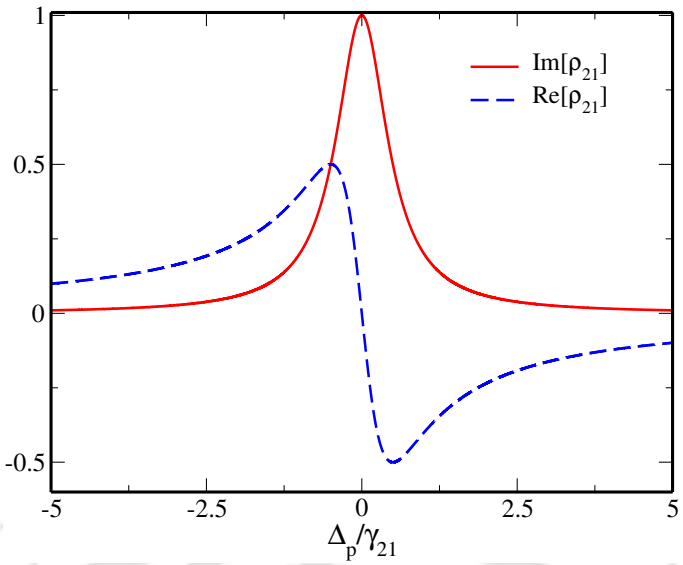

Fig. 1.4 Imaginary and real part of the normalized atomic coherence ρ_{21} are shown as a function of probe field detuning. The parameter is $\Omega_p = 0.01\gamma_{21}$.

Now, the induced polarization of the medium having atom number density $\mathcal{N}$ and dipole operator $\hat{\mathbf{d}}$ is defined as

$$\begin{aligned} \mathbf{P} = \mathcal{N}\langle\hat{\mathbf{d}}\rangle &= \mathcal{N}Tr[\rho\hat{\mathbf{d}}], \\ &= \mathcal{N}(d_{12}\rho_{21} + h.c.). \end{aligned} \tag{1.83}$$

The susceptibility of the medium is obtained from the induced polarization as these two parameters are related by $\mathbf{P} = \chi\mathbf{E}$. The expression of susceptibility is given by

$$\begin{aligned} \chi(\omega_p) &= \frac{\mathcal{N}|d_{21}|^2}{\hbar\Omega_p}\rho_{21}, \\ &= \frac{\mathcal{N}|d_{21}|^2}{\hbar\Omega_p}\frac{i\Omega_p(2\gamma_{21} + i\,4\Delta_p)}{(\gamma_{21}^2 + 4\Delta_p^2) + 8|\Omega_p|^2}. \end{aligned} \tag{1.84}$$

Note that Eq. (1.85) is an exact solution of medium susceptibility which includes both linear and nonlinear terms of Rabi frequency (Ω_p) and probe detuning (Δ_p). Under weak probe approximation, the susceptibility expression only retains the linear part of Ω_p and Δ_p. The linear susceptibility of the medium is given by

$$\chi(\omega_p) = \frac{\mathcal{N}|d_{21}|^2}{\hbar\Omega_p}\rho_{21}; \qquad \rho_{21} = \frac{i\Omega_p}{\frac{\gamma_{21}}{2} - i\Delta_p}. \tag{1.85}$$

In Fig. 1.4, we plot the imaginary and real part of the normalized atomic coherence ρ_{21} as a function of probe field detuning (Δ_p). In Fig. 1.4, the imaginary part of the

coherence indicates the absorption profile whereas real part of the coherence shows the dispersion profile. It can be seen from Fig. 1.4, the atomic medium experiences huge absorption accompanied with a steep anomalous dispersion at resonance *i.e.* $\Delta_p = 0$. Therefore, a light pulse propagating through such two-level atomic system encounters very high absorption. In the next section, we discuss how an additional EM field converts this absorptive medium into a transparent atomic medium.

1.3 Interaction of light with a three-level atomic system

In this section, we study the interaction of two electro-magnetic fields with three-level atomic system. In a three-level Λ-type configuration, two optical fields couple one excited state $|3\rangle$ with two closely spaced ground states $|1\rangle$ and $|2\rangle$. As shown in Fig. 1.5, a weak probe field of frequency ω_p and a strong control field of frequency ω_c drive the electric dipole allowed transitions $|3\rangle \leftrightarrow |1\rangle$ and $|3\rangle \leftrightarrow |2\rangle$ respectively. The probe and control fields are expressed by

$$\mathbf{E}_p(\mathbf{r},t) = \hat{\mathbf{e}}_p \mathcal{E}_p(\mathbf{r}) e^{i(\mathbf{k}_p\cdot\mathbf{r}-\omega_p t)} + c.c, \tag{1.86}$$

$$\mathbf{E}_c(\mathbf{r},t) = \hat{\mathbf{e}}_c \mathcal{E}_c(\mathbf{r}) e^{i(\mathbf{k}_c\cdot\mathbf{r}-\omega_c t)} + c.c, \tag{1.87}$$

where $\mathcal{E}_p(\mathbf{r})$ and $\mathcal{E}_c(\mathbf{r})$ are the slowly varying envelope functions, $\hat{\mathbf{e}}_p$ and $\hat{\mathbf{e}}_c$ are unit polarization vectors, $\mathbf{k}_p$ and $\mathbf{k}_c$ are the wave vectors of the probe and control field respectively. The unperturbed Hamiltonian of the system is written as

$$H_0 = \hbar\omega_{31} |3\rangle\langle 3| + \hbar\omega_{32} |2\rangle\langle 2| . \tag{1.88}$$

The interaction between the electro-magnetic fields and three-level atomic system is expressed by the following interaction Hamiltonian

$$\begin{aligned} H_I &= -\mathbf{d}\cdot[\mathbf{E}_p(\mathbf{r},t) + \mathbf{E}_c(\mathbf{r},t)] , \\ H_I &= -\left[\Omega_p e^{-i\omega_p t} + \tilde{\Omega}_p e^{i\omega_p t}\right] |3\rangle\langle 1| - \left[\Omega_c e^{-i\omega_c t} + \tilde{\Omega}_c e^{i\omega_c t}\right] |3\rangle\langle 2| + h.c. \end{aligned} \tag{1.89}$$

The probe and control field Rabi frequencies in Eq. (1.89) are defined as

$$\Omega_p = \frac{\mathbf{d}_{31}\cdot\hat{\mathbf{e}}_p}{\hbar}\mathcal{E}_p(\mathbf{r}) e^{i\mathbf{k}_p\cdot\mathbf{r}} \quad \text{and} \quad \tilde{\Omega}_p = \frac{\mathbf{d}_{31}\cdot\hat{\mathbf{e}}_p}{\hbar}\mathcal{E}_p^*(\mathbf{r}) e^{-i\mathbf{k}_p\cdot\mathbf{r}}, \tag{1.90}$$

$$\Omega_c = \frac{\mathbf{d}_{32}\cdot\hat{\mathbf{e}}_c}{\hbar}\mathcal{E}_c(\mathbf{r}) e^{i\mathbf{k}_c\cdot\mathbf{r}} \quad \text{and} \quad \tilde{\Omega}_c = \frac{\mathbf{d}_{32}\cdot\hat{\mathbf{e}}_c}{\hbar}\mathcal{E}_c^*(\mathbf{r}) e^{-i\mathbf{k}_c\cdot\mathbf{r}}. \tag{1.91}$$

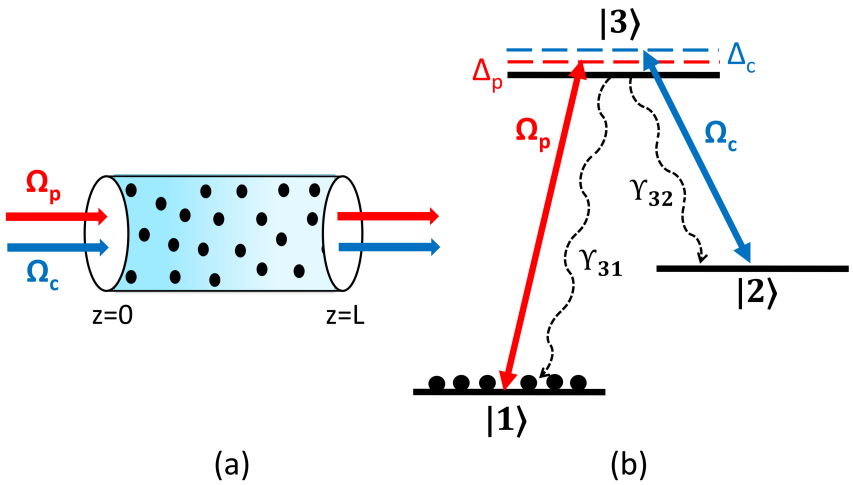

Fig. 1.5 (a) A simple interaction model of light with a three-level atomic system. (b) The energy level diagram of a three-level atomic system. The excited state $|3\rangle$ is coupled with ground states $|1\rangle$ and $|2\rangle$ by two monochromatic laser field Ω_p, Ω_c respectively. The spontaneous decay rates from excited state to ground states are γ_{31} and γ_{32}.

$\mathbf{d}_{31} = \langle 3|\,\mathbf{d}\,|1\rangle$, $\mathbf{d}_{32} = \langle 3|\,\mathbf{d}\,|2\rangle$ are the transition dipole moments between the states $|3\rangle \leftrightarrow |1\rangle$ and $|3\rangle \leftrightarrow |2\rangle$ respectively. The total Hamiltonian of the three level system is given by

$$H = H_0 + H_I. \tag{1.92}$$

Now, in order to make the above Hamiltonian time-independent, we perform the following unitary transformation

$$H_{eff} = U^{\dagger} H U - i\hbar U^{\dagger} \frac{\partial U}{\partial t}, \tag{1.93}$$

where U is defined as

$$U = e^{-\frac{i}{\hbar}(\hbar\omega_p|3\rangle\langle 3| + \hbar(\omega_p - \omega_c)|2\rangle\langle 2|)t}. \tag{1.94}$$

The effective Hamiltonian under unitary transformation and rotating wave approximation is expressed as

$$\begin{aligned} H_{eff} = &-\hbar\Delta_p\,|3\rangle\langle 3| - \hbar(\Delta_p - \Delta_c)\,|2\rangle\langle 2| - \hbar\Omega_p\,|3\rangle\langle 1| \\ &- \hbar\Omega_p^*\,|1\rangle\langle 3| - \hbar\Omega_c\,|3\rangle\langle 2| - \hbar\Omega_c^*\,|2\rangle\langle 3|\,. \end{aligned} \tag{1.95}$$

In Eq. (1.95), $\Delta_p = \omega_p - \omega_{31}$, $\Delta_c = \omega_c - \omega_{32}$ are the probe and control field detuning respectively. We employ this effective Hamiltonian in the Liouville's equation to study the dynamics of the three level system.

1.3.1 Dynamics of population and coherence in a three-level system

The dynamics of the population and coherence in the three-level atomic system is governed by the Liouville's equation

$$\frac{\partial \rho}{\partial t} = -\frac{i}{\hbar}[H_{eff}, \rho] + \mathcal{L}\rho. \tag{1.96}$$

The last term of Eq. (1.96) *i.e.* $\mathcal{L}\rho$ is the Liouville operator which describes various incoherent processes and is given by

$$\begin{aligned}\mathcal{L}\rho = &-\frac{\gamma_{31}}{2}(|3\rangle\langle 3|\rho - 2|1\rangle\langle 1|\rho_{33} + \rho|3\rangle\langle 3|) \\ &-\frac{\gamma_{32}}{2}(|3\rangle\langle 3|\rho - 2|2\rangle\langle 2|\rho_{33} + \rho|3\rangle\langle 3|),\end{aligned} \tag{1.97}$$

where γ_{31}, γ_{32} correspond to spontaneous decay rates from excited state $|3\rangle$ to ground states $|1\rangle$ and $|2\rangle$ respectively. Now, the equation of motion for the diagonal and off-diagonal density matrix elements are obtained from Eq. (1.96) and are given by

$$\begin{aligned}\dot{\rho}_{31} &= -\left(\frac{\gamma_{31}}{2} - i\Delta_p\right)\rho_{31} + i\Omega_c\rho_{21} + i\Omega_p(\rho_{11} - \rho_{22}), \\ \dot{\rho}_{32} &= -\left(\frac{\gamma_{32}}{2} - i\Delta_c\right)\rho_{32} + i\Omega_p\rho_{12} + i\Omega_c(\rho_{22} - \rho_{33}), \\ \dot{\rho}_{21} &= -\left[\gamma_c - i(\Delta_p - \Delta_c)\right]\rho_{21} - i\Omega_p\rho_{23} + i\Omega_c^*\rho_{31}, \\ \dot{\rho}_{11} &= \gamma_{31}\rho_{33} + i\Omega_p^*\rho_{31} - i\Omega_p\rho_{13}, \\ \dot{\rho}_{22} &= \gamma_{32}\rho_{33} + i\Omega_c^*\rho_{32} - i\Omega_c\rho_{23}, \\ \dot{\rho}_{33} &= -\dot{\rho}_{11} - \dot{\rho}_{22}.\end{aligned} \tag{1.98}$$

The decoherence rate of the ground state coherence ρ_{21} is given by γ_c. We consider that total population of the three-level atomic system is conserved *i.e.* $\rho_{11} + \rho_{22} + \rho_{33} = 1$. The remaining off-diagonal density matrix elements in Eq. (1.98) can be derived from $\rho_{ij} = \rho_{ji}^*$.

1.3.2 Steady-state solution

In this section, we employ a perturbative approach to solve the density matrix equations under steady state condition *i.e.* $\dot{\rho} = 0$. In perturbative approach, we consider a weak probe field so that we can expand the density matrix to the first order in probe as

$$\rho_{ij} = \rho_{ij}^{(0)} + \Omega_p\rho_{ij}^{(1)} + \Omega_p^*\rho_{ij}^{(2)}, \tag{1.99}$$

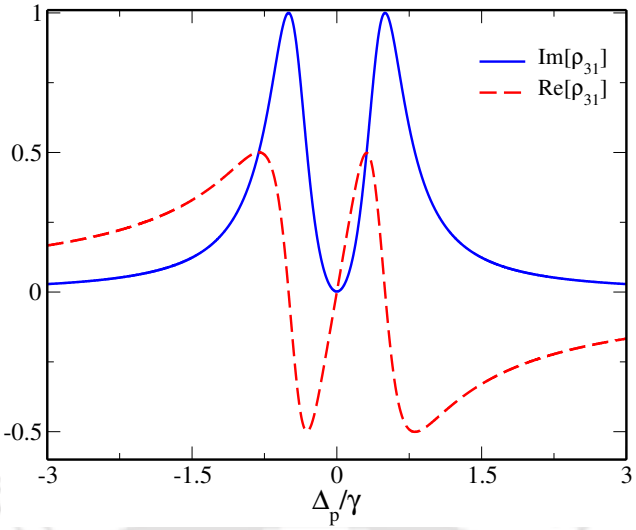

Fig. 1.6 Imaginary and real part of the normalized atomic coherence ρ_{31} are plotted as a function of probe field detuning. The parameters are $\Omega_p = 0.01\gamma$, $\Omega_c = 0.5\gamma$, $\Delta_c = 0$, $\gamma_{31} = \gamma_{32} = \gamma$, $\gamma_c = 0.001\gamma$.

where $\rho_{ij}^{(0)}$ represents the solution in the absence of probe field. We consider entire population are in in ground state $|1\rangle$ in absence of Ω_p such that $\rho_{11}^{(0)} = 1$. The $\rho_{ij}^{(1)}$ and $\rho_{ij}^{(2)}$ describe the first order solutions at positive and negative frequency of the probe field respectively. Now, we implement Eq. (1.99) into the density matrix equations and equate the coefficients of Ω_p to obtain a set of 8 coupled equations. We solve steady state of these coupled equations in order to obtain the atomic coherence $\rho_{31}^{(1)}$. The steady state solution of the atomic coherence ρ_{31} under weak probe approximation is given by

$$\rho_{31} = \Omega_p \rho_{31}^{(1)} = \frac{i\Omega_p}{(\frac{\gamma_{31}}{2} - i\Delta_p) + \frac{|\Omega_c|^2}{\gamma_c - i(\Delta_p - \Delta_c)}}. \tag{1.100}$$

The linear susceptibility of the three-level atomic system is described in terms of atomic coherence ρ_{31} by the following expression

$$\chi(\omega_p) = \frac{\mathcal{N}|d_{31}|^2}{\hbar\Omega_p}\rho_{31}. \tag{1.101}$$

In Fig. 1.6, we plot the imaginary and real part of the normalized atomic coherence ρ_{31} as a function of probe field detuning. The imaginary part of the coherence, Im$[\rho_{31}]$ clearly shows that the absorption completely disappears at a position where two photon resonance condition $(\Delta_p - \Delta_c) = 0$ is satisfied. This implies that the coherently prepared atomic medium becomes transparent to a weak probe field in the presence of a strong control field. This phenomena of absorption cancellation at the line centre is called *electromagnetically induced transparency* (EIT). The EIT

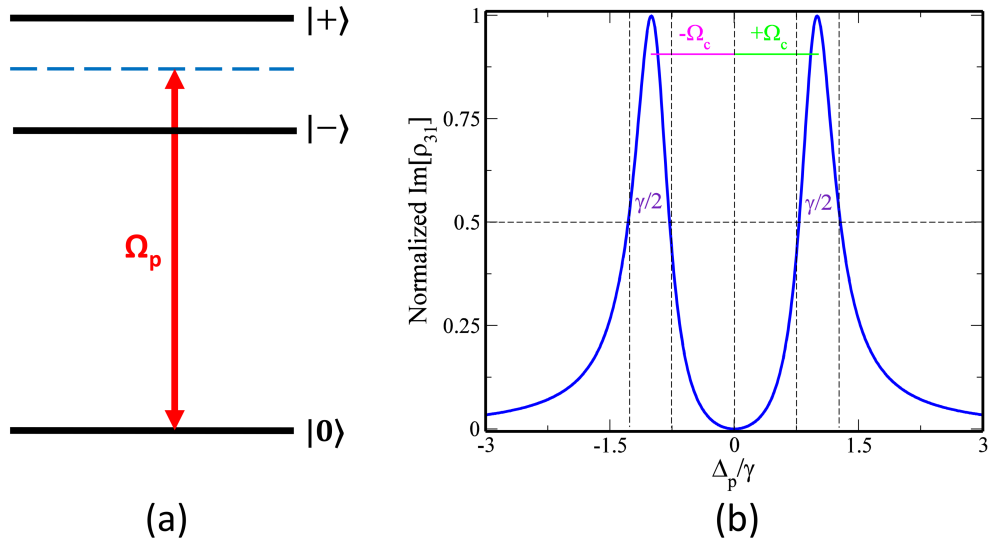

Fig. 1.7 (a) Schematic diagram of dressed states. (b) The characteristics of EIT window and two absorption peaks are shown from the dressed state analysis. The value of Ω_c is 1.0γ. Therefore, two absorption peaks are located at $\Delta_p = \pm 1.0\gamma$.

phenomena can be explained with the help of quantum interference theory. It is familiar that the transition amplitudes of several possible atomic transitions between the coupled energy states can interfere either constructively or destructively [49]. For a three-level Λ-type system, the atom in state $|1\rangle$ can be excited to the state $|3\rangle$ via two possible pathways. One is the direct path $|1\rangle \rightarrow |3\rangle$ and the other one is indirect path $|1\rangle \rightarrow |3\rangle \rightarrow |2\rangle \rightarrow |3\rangle$. At two photon resonance condition, the transition amplitudes corresponding to these two transition pathways interfere destructively. Therefore, the absorption of the probe field is cancelled and the EIT window is created at the line centre *i.e.* $\Delta_p = 0$. Simultaneously, real part of the coherence, $\mathrm{Re}[\rho_{31}]$ shows a steep normal dispersion within the transparency window. The steepness of this dispersion curve can be enhanced further by increasing the control field strength. In 1986, Agarwal first acknowledges the possibility of controlling dispersive and absorptive properties of a medium with the help of an extra resonant laser field [50]. Much later in 1991, Stevan Harris's group properly demonstrates the EIT phenomena in a Λ-system [51]. Since then EIT has been extensively studied in a wide variety of fields due to its potential applications. There are many articles in literature which nicely review all successive EIT based applications [1–3].

1.3.3 Dressed state analysis of three-level Λ system

In this section, we explain the reason behind the cancellation of absorption in EIT with dressed state analysis. Under the weak probe approximation ($\Omega_p \ll \Omega_c$) the

dressed states of a three-level Λ system are given by

$$|0\rangle = |1\rangle\,, \tag{1.102}$$

$$|+\rangle = \frac{1}{\sqrt{2}}(|3\rangle + |2\rangle), \tag{1.103}$$

$$|-\rangle = \frac{1}{\sqrt{2}}(|3\rangle - |2\rangle). \tag{1.104}$$

In dressed state picture, $|1\rangle$ becomes the dark state whereas $|2\rangle$ and $|3\rangle$ are dressed in two superposition states $|+\rangle$ and $|-\rangle$ due to the strong control field Ω_c. The superposition states $|+\rangle$ and $|-\rangle$ are separated by an amount $\pm\Omega_c$ from the excited state $|3\rangle$. Therefore, the transition from $|0\rangle$ to the dressed states $|+\rangle$ and $|-\rangle$ generates two absorption peaks at $\Delta_p = \pm\Omega_c$ as shown in Fig. 1.7. The transition from $|0\rangle$ to $|3\rangle$ does not take place which results in a decrease of absorption at $\Delta_p = 0$. The width of the transparency window increases with the increase of control field intensity because the spacing between the absorption peak enhances with Ω_c. Note that the linewidth of two absorption peaks is $\gamma/2$ and it does not change with the variation of Ω_c.

1.4 Basic propagation equation in a dielectric medium

The propagation of classical EM fields through a material medium is perfectly described by the fundamental equations of James Clerk Maxwell. In this thesis, we consider the Gaussian unit system because of symmetry properties and physical usefulness. Now, the Maxwell's equations for the medium can be written as

$$\text{Gauss's law for electrostatics :} \qquad \nabla.\mathbf{D} = 4\pi\varrho, \tag{1.105}$$

$$\nabla.\mathbf{B} = 0, \tag{1.106}$$

$$\text{Faraday's law :} \qquad \nabla \times \mathbf{E} = -\frac{1}{c}\frac{\partial \mathbf{B}}{\partial t}, \tag{1.107}$$

$$\text{Ampere's law :} \qquad \nabla \times \mathbf{H} = \frac{4\pi}{c}\mathbf{J} + \frac{1}{c}\frac{\partial \mathbf{D}}{\partial t}. \tag{1.108}$$

where ϱ is the free charge density, $\mathbf{J}$ is the free current density, and c is the speed of light in vacuum. The electric and magnetic field vectors of light are denoted by $\mathbf{E}$ and $\mathbf{H}$ [52]. The electric displacement vector, $\mathbf{D}$ and the magnetic induction vector, $\mathbf{B}$ inside the material medium are coupled by the following equations

$$\mathbf{D} = \mathbf{E} + 4\pi\mathbf{P}, \tag{1.109}$$

$$\mathbf{B} = \mathbf{H} + 4\pi\mathbf{M}. \tag{1.110}$$

where **P** and **M** are the electric and magnetic polarization of the medium respectively. In free space, both **P** and **M** become zero. In material medium, **P** and **M** appear as an influence of the matter on the field. In Eq. (1.109), electric dipole moment is the dominant quantity at optical frequency and contributions from all higher order terms such as electric quadrapole, electric octupole moments have been excluded. Further, in this thesis, we consider a non-magnetic ($\mathbf{M} = 0$) and non-conducting ($\mathbf{J} = 0$) medium which does not possess any free charges ($\varrho = 0$). Now, using Eq. (1.108) and the curl of Eq. (1.107), we obtain the following equation

$$\nabla \times \nabla \times \mathbf{E} = -\frac{1}{c^2}\frac{\partial^2}{\partial t^2}(\mathbf{E} + 4\pi\mathbf{P}). \tag{1.111}$$

We further simplify Eq. (1.111) by applying the vector identity

$$\nabla \times \nabla \times \mathbf{E} = \nabla(\nabla.\mathbf{E}) - \nabla^2\mathbf{E}. \tag{1.112}$$

The first term on right-hand side vanishes because of unavailability of free charges ($\varrho = 0$). We combine Eq. (1.112) and Eq. (1.111) to obtain the following form of the wave equation for electric field

$$\nabla^2\mathbf{E} - \frac{1}{c^2}\frac{\partial^2\mathbf{E}}{\partial t^2} = \frac{4\pi}{c^2}\frac{\partial^2\mathbf{P}}{\partial t^2}. \tag{1.113}$$

Eq. (1.113) is known as Maxwell's wave equation in a material medium. This equation describes the propagation dynamics of a field through the medium. The optical properties of the medium such as absorption and refractive index modify the evolution of the electric field. The source term on the right-hand side of Eq. (1.113) incorporates nonlinear responses of the medium. Hence, Maxwell's wave equation becomes nonlinear in the presence of a polarized medium. The exact solution of nonlinear wave equation requires strenuous effort. So, we employ few reasonable approximations to simplify the wave equation. We consider a quasi-monochromatic wave propagating in the z-direction through a dielectric medium. The electric field and induced medium polarization due to this field can be described as

$$\mathbf{E}(x, y, z, t) = \hat{\mathbf{e}}\mathcal{E}(x, y, z, t)e^{i(kz-\omega t)} + c.c. \tag{1.114}$$

$$\mathbf{P}(x, y, z, t) = \hat{\mathbf{e}}\mathcal{P}(x, y, z, t)e^{i(kz-\omega t)} + c.c. \tag{1.115}$$

where $\hat{\mathbf{e}}$ is the direction of polarization, ω is the carrier frequency, $k = \omega/c$ is the wave number. $\mathcal{E}(x, y, z, t)$ and $\mathcal{P}(x, y, z, t)$ are the envelope functions of the electric field and polarization. The complex conjugate (c.c.) term has been added to the complex electric field and polarization expression to make it real. The required space and time

derivatives of Eq. (1.113) are given by

$$\nabla^2\mathbf{E} = \hat{\mathbf{e}}(\nabla_\perp^2\mathcal{E} + \frac{\partial^2\mathcal{E}}{\partial z^2} + 2ik\frac{\partial\mathcal{E}}{\partial z} - k^2\mathcal{E})e^{i(kz-\omega t)} + c.c. \tag{1.116}$$

$$\frac{\partial^2\mathbf{E}}{\partial t^2} = \hat{\mathbf{e}}(\frac{\partial^2\mathcal{E}}{\partial t^2} - 2i\omega\frac{\partial\mathcal{E}}{\partial t} - \omega^2\mathcal{E}) + c.c. \tag{1.117}$$

$$\frac{\partial^2\mathbf{P}}{\partial t^2} = \hat{\mathbf{e}}(\frac{\partial^2\mathcal{P}}{\partial t^2} - 2i\omega\frac{\partial\mathcal{P}}{\partial t} - \omega^2\mathcal{P}) + c.c. \tag{1.118}$$

where the second order partial derivative in the (x, y) plane *i.e.* $\nabla_\perp^2 = (\partial^2/\partial x^2 + \partial^2/\partial y^2)$ is the transverse Laplacian operator and represents the variation of the field in the transverse direction. Now, we propose an important approximation which leads to significant mathematical simplifications to the wave Eq. (1.113). We assume that the variations of envelope functions $\mathcal{E}(x, y, z, t)$ and $\mathcal{P}(x, y, z, t)$ in space and time are very small within the optical period and optical wavelength. The mathematical representations of this assumption are shown by the following inequalities

$$\left|\frac{\partial^2\mathcal{E}}{\partial z^2}\right| \ll \left|k\frac{\partial\mathcal{E}}{\partial z}\right| \ll \left|k^2\mathcal{E}\right|, \qquad \left|\frac{\partial^2\mathcal{P}}{\partial z^2}\right| \ll \left|k\frac{\partial\mathcal{P}}{\partial z}\right| \ll \left|k^2\mathcal{P}\right|, \tag{1.119}$$

$$\left|\frac{\partial^2\mathcal{E}}{\partial t^2}\right| \ll \left|\omega\frac{\partial\mathcal{E}}{\partial t}\right| \ll \left|\omega^2\mathcal{E}\right|, \qquad \left|\frac{\partial^2\mathcal{P}}{\partial t^2}\right| \ll \left|\omega\frac{\partial\mathcal{P}}{\partial t}\right| \ll \left|\omega^2\mathcal{P}\right|. \tag{1.120}$$

The above approximation is known as the *"slowly varying envelope approximation"* (SVEA). The SVEA approximation plays a key role in laser physics and light propagation problems [53]. The inequalities in Eq. (1.119) and Eq. (1.120) suggest that we can neglect the higher order derivatives with respect to z and t. We apply this approximation on Eq. (1.116), Eq. (1.117), Eq. (1.118) and substitute the derivatives into the wave Eq. (1.113). For a slowly varying electric field envelope the wave equation reshape into the following form

$$\frac{1}{2ik}\nabla_\perp^2\mathcal{E} + \frac{\partial\mathcal{E}}{\partial z} + \frac{1}{c}\frac{\partial\mathcal{E}}{\partial t} = 2\pi ik\mathcal{P}. \tag{1.121}$$

Eq. (1.121) efficiently governs the propagation dynamics of slowly varying electric field envelope $\mathcal{E}(x, y, z, t)$ through the dielectric medium.

1.4.1 Propagation equation for light pulse

For a light pulse, the transverse variation of the field is very small in comparison with the variation along the propagation direction. Therefore, we can safely ignore the first term of Eq. (1.121). The propagation equation for the light pulse reduces to

$$\frac{\partial\mathcal{E}}{\partial z} + \frac{1}{c}\frac{\partial\mathcal{E}}{\partial t} = 2\pi ik\mathcal{P}. \tag{1.122}$$

We solve the pulse propagation Eq. (1.122) in a reference frame moving with the velocity of light in vacuum c. We transform to new variables

$$\tau = t - \frac{z}{c}, \quad \xi = z. \tag{1.123}$$

so that

$$\frac{\partial}{\partial z} + \frac{1}{c}\frac{\partial}{\partial t} = \frac{\partial}{\partial \xi}, \quad \frac{\partial}{\partial t} = \frac{\partial}{\partial \tau}. \tag{1.124}$$

In new frame, Eq. (1.122) simplifies into the following form

$$\frac{\partial \mathcal{E}}{\partial \xi} = 2\pi i k \mathcal{P}. \tag{1.125}$$

Eq. (1.125) governs the propagation of light pulse $\mathcal{E}(\xi, \tau)$ through the atomic medium [54]. The polarization $\mathcal{P}(\xi, \tau)$ in Eq. (1.125) is the source term which determines how the light pulse propagates through the material medium.

1.4.2 Propagation equation for light beam

We now study the propagation equation of a light beam. In case of a continuous wave quasi-monochromatic field, the amplitude $\mathcal{E}(x, y, z)$ does not vary with time *i.e.* $\partial\mathcal{E}/\partial t = 0$. Therefore, the propagation equation for a light beam is given by

$$\frac{1}{2ik}\nabla_\perp^2 \mathcal{E} + \frac{\partial \mathcal{E}}{\partial z} = 2\pi i k \mathcal{P}. \tag{1.126}$$

The above form of wave equation is known as paraxial wave equation. We can further expressed Eq. (1.126) in terms of Rabi frequency Ω as shown below

$$\frac{\partial \Omega}{\partial z} = \frac{i}{2k}\nabla_\perp^2 \Omega + 2\pi i k \chi \Omega, \tag{1.127}$$

where χ is the susceptibility of the medium. The first term on right hand side is a second order partial derivative in the xy plane *i.e.* $\nabla_\perp^2 = (\partial^2/\partial x^2 + \partial^2/\partial y^2)$ which describes inherent optical diffraction of the light beam. The second term on right hand side incorporates the dispersion and absorption profile of the medium.

1.5 Solution of paraxial wave equation in free-space

In this section, we study various solutions of paraxial wave equation in free-space. We completely ignore the source term *i.e.* $\mathcal{P} = 0$ in free-space wave equation for the

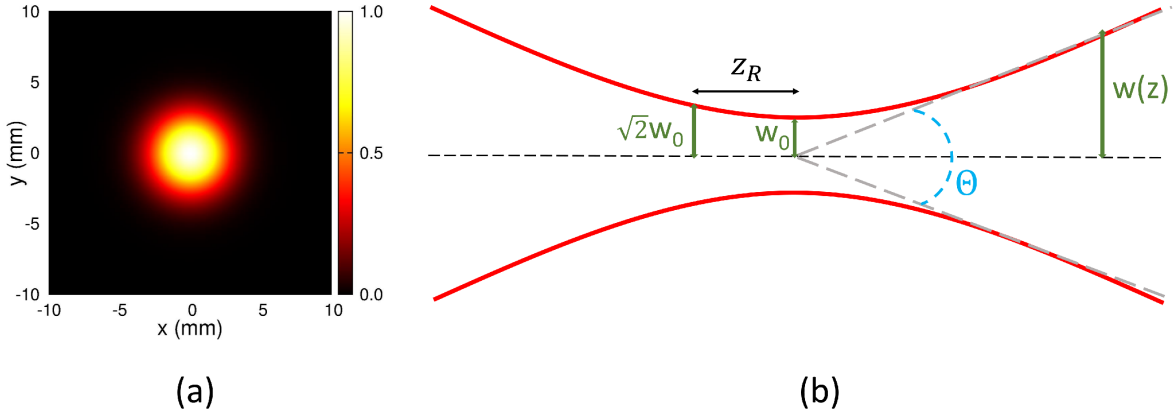

Fig. 1.8 (a) Intensity profile of a Gaussian beam in transverse plane. (b) The variation of Gaussian beam width $w(z)$ along the propagation axis. The minimum beam waist is w_0. The Rayleigh length z_R of the Gaussian beam is the distance from the minimum beam waist where the beam width $w(z)$ is increased by a factor of the square root of 2 *i.e.* $w(z_R) = \sqrt{2}w_0$. The divergence angle of the beam is given by Θ.

electric field. Thus the paraxial wave equation in free-space is given by

$$\frac{\partial^2 \mathcal{E}}{\partial x^2} + \frac{\partial^2 \mathcal{E}}{\partial y^2} + 2ik\frac{\partial \mathcal{E}}{\partial z} = 0. \tag{1.128}$$

In Eq. (1.128), we consider that the variation of electric field $\mathcal{E}(x, y, z)$ along the z-axis are very small as compared to transverse directions (x, y) within a distance of the order of a wavelength. This consideration can be demonstrated mathematically in the following form

$$\left|\frac{\partial^2 \mathcal{E}}{\partial z^2}\right| \ll \left|\frac{\partial^2 \mathcal{E}}{\partial x^2}\right|, \left|\frac{\partial^2 \mathcal{E}}{\partial y^2}\right|, \left|k\frac{\partial \mathcal{E}}{\partial z}\right| \tag{1.129}$$

Eq. (1.129) is known as paraxial wave approximation. Eq. (1.128) offers an infinite set of functions as a solution such as Gaussian, Laguerre-Gaussian and Hermite-Gaussian modes. Next, we study some of these solutions of the paraxial wave equation in great detail.

Gaussian mode

The Gaussian mode is a basic solution of the paraxial wave equation. In Fig. 1.8(a), we show the intensity profile of a Gaussian mode in transverse plane. The complex

electric field amplitude of Gaussian mode can be expressed as

$$\mathcal{E}(x,y,z) = \mathcal{E}_0 \frac{w_0}{w(z)} \exp\left[-\frac{(x^2+y^2)}{w^2(z)} + \frac{ik(x^2+y^2)}{2R(z)} - ikz - i\tan^{-1}\left(\frac{z}{z_R}\right)\right],$$
$$w(z) = w_0\sqrt{1+\left(\frac{z}{z_R}\right)^2}, \quad R(z) = z + \frac{z_R^2}{z}, \quad z_R = \pi w_0^2/\lambda. \tag{1.130}$$

In Eq. (1.130), $w(z)$ represents the spot size of the beam. The minimum value of spot size is w_0 which occurs at $z = 0$. The quantity $R(z)$ is known as radius of curvature of the beam's wavefront. The parameter z_R is called Rayleigh length. Its value implies the distance on z-axis from minimum beam waist to the point at which the beam width $w(z)$ becomes $\sqrt{2}w_0$. Rayleigh length depends on the minimum beam waist w_0 and wavelength of light beam λ. In Fig. 1.8(b), we portray the variation of Gaussian beam width $w(z)$ along the propagation axis. Fig. 1.8(b) clearly indicates that size of the beam $w(z)$ increases with distance as the Gaussian mode propagates along z-axis. The divergence angle of a Gaussian mode for a distance $z \gg z_R$ is given by

$$\Theta = 2\theta = 2\frac{w(z)}{z},$$
$$\approx 2\frac{w_0}{z_R} = \frac{2\lambda}{\pi w_0}. \tag{1.131}$$

Eq. (1.131) clearly shows that divergence angle Θ is inversely proportional to the minimum beam waist w_0. Therefore, a Gaussian mode with a narrow spot size spreads rapidly as it moves away from the beam waist w_0.

Hermite-Gaussian mode

The paraxial wave equation in Cartesian coordinate offers a family of solutions known as Hermite-Gaussian modes. The transverse electric field distribution of Hermite-Gaussian mode is given by the product of a Gaussian function and a Hermite polynomial along with a phase term

$$\mathcal{E}(x,y,z) = \mathcal{E}_0 \frac{w_0}{w(z)} H_n\left(\frac{\sqrt{2}x}{w(z)}\right) H_m\left(\frac{\sqrt{2}y}{w(z)}\right) \exp\left[-\frac{(x^2+y^2)}{w^2(z)}\right]$$
$$\times \exp\left[-i(n+m+1)\tan^{-1}\left(\frac{z}{z_R}\right)\right], \tag{1.132}$$

where H_n and H_m are the n^{th} and m^{th} order Hermite polynomials. The indices m and n are non-negative integers. The first few Hermite polynomials are shown as a

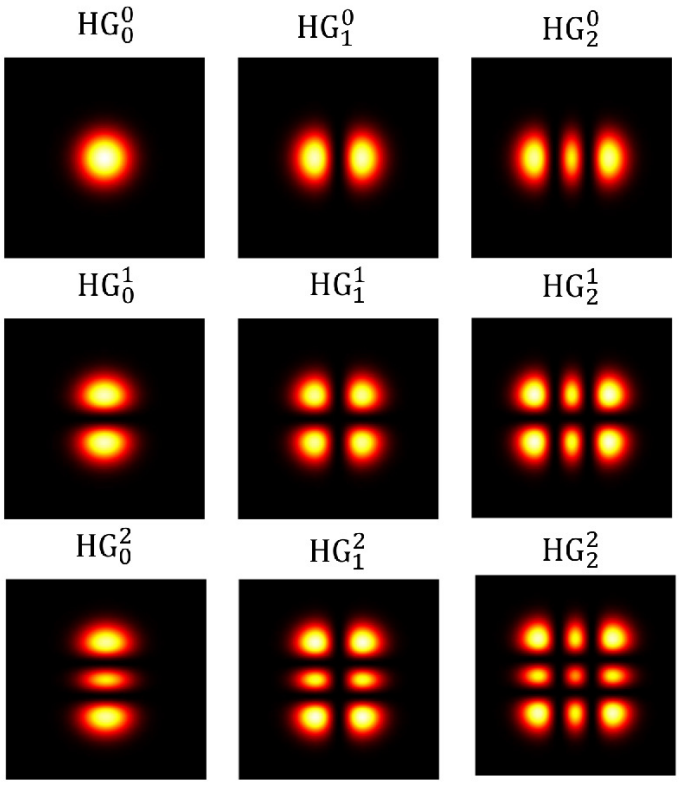

Fig. 1.9 Intensity profiles of various Hermite-Gaussian modes HG_n^m are plotted at $z = 0$. The mode numbers n and m determine the shape of a specific profile in x and y plane respectively.

function of $\zeta = \sqrt{2}x/w(z)$

$$\begin{aligned} H_0(\zeta) &= 1, \\ H_1(\zeta) &= 2\zeta, \\ H_2(\zeta) &= 4\zeta^2 - 2, \\ H_3(\zeta) &= 8\zeta^3 - 12\zeta. \end{aligned} \tag{1.133}$$

The polynomials shown in Eq. (1.133) determine the shape of the beam profile in the x and y direction. Intensity profiles of various Hermite-Gaussian modes HG_n^m are shown in Fig. 1.9. The intensity distribution clearly indicates that each mode has n nodes along the vertical direction and m nodes along the horizontal direction. For $n = 0$ and $m = 0$, we obtain the intensity distribution of a Gaussian mode. This HG_0^0 mode is also called the fundamental mode.

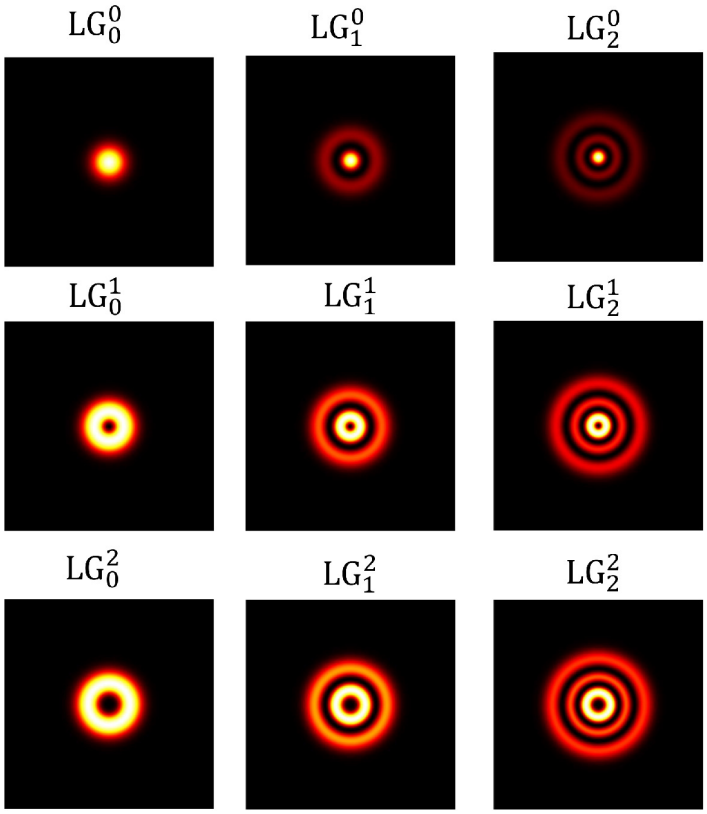

Fig. 1.10 Intensity profiles of various Laguerre-Gaussian modes LG_m^l are plotted at $z = 0$. The mode numbers m and l determine the shape of a specific intensity profile in x and y plane respectively. LG_0^0 mode represents intensity distribution of the fundamental mode. The other LG_m^l modes display concentric ring-shaped intensity distribution. A particular LG_m^l mode includes $(m+1)$ rings except LG_0^0 mode.

Laguerre-Gaussian mode

Laguerre-Gaussian modes are the general solution of paraxial wave equation in cylindrical coordinate. The paraxial wave equation in cylindrical coordinate (r, ϕ, z) can be written as

$$\frac{1}{r}\frac{\partial}{\partial r}\left(r\frac{\partial \mathcal{E}}{\partial r}\right) + \frac{1}{r^2}\frac{\partial^2 \mathcal{E}}{\partial \phi^2} + 2ik\frac{\partial \mathcal{E}}{\partial z} = 0, \tag{1.134}$$

where we have considered the following relation

$$\frac{\partial^2}{\partial x^2} + \frac{\partial^2}{\partial y^2} \equiv \frac{1}{r}\frac{\partial}{\partial r}\left(r\frac{\partial}{\partial r}\right) + \frac{1}{r^2}\frac{\partial^2}{\partial \phi^2}. \tag{1.135}$$

Now, the solution of Eq. (1.134) is expressed as

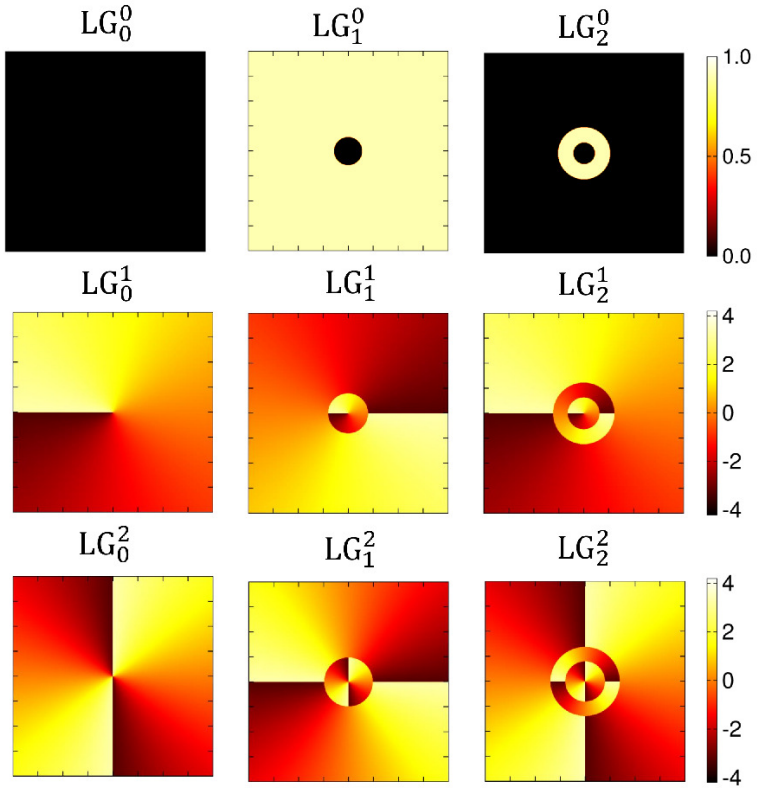

Fig. 1.11 Phase profiles of various Laguerre-Gaussian modes LG_m^l are plotted at $z = 0$. The mode numbers m and l determine the shape of a specific phase profile in x and y plane respectively. The total phase change in the transverse plane is given by $2\pi l$.

$$\begin{aligned}\mathcal{E}(r,\phi,z) = \mathcal{E}_0 \frac{w_0}{w(z)} \left(\frac{r\sqrt{2}}{w(z)}\right)^{|l|} \exp\left[-\frac{r^2}{w^2(z)}\right] L_m^l\left[\frac{2r^2}{w^2(z)}\right] e^{il\phi} \\ \times \exp\left[\frac{ikr^2}{2R(z)}\right] \exp\left[-i(2m+|l|+1)\tan^{-1}\left(\frac{z}{z_0}\right)\right]; \\ r = \sqrt{x^2+y^2}, \quad \phi = \tan^{-1}\left(\frac{y}{x}\right), \end{aligned} \tag{1.136}$$

where L_m^l are the generalized Laguerre polynomials with l is an integer and m is a non-negative integer. A few Laguerre polynomials are shown below

$$\begin{aligned} L_0^l(\zeta) &= 1, \\ L_1^l(\zeta) &= -\zeta + l + 1, \\ L_2^l(\zeta) &= \frac{1}{2}[\zeta^2 - 2(l+2)\zeta + (l+1)(l+2)]. \end{aligned} \tag{1.137}$$

In Fig. 1.10, we show the intensity profiles of various Laguerre-Gaussian modes LG_m^l at $z = 0$. The phase profiles of the corresponding Laguerre-Gaussian modes LG_m^l can be found in Fig. 1.11. The Laguerre-Gaussian modes display concentric ring-shaped

intensity distribution. The number of ring is determined by the mode index m. Any particular LG_m^l mode in Fig. 1.10 includes $(m+1)$ rings except LG_0^0 mode which represents intensity distribution of the fundamental mode like HG_0^0 mode. The other mode index l decides the structure of azimuthal phase term $e^{il\phi}$ as shown in Fig. 1.11. The total phase change in the transverse plane is given by $2\pi l$.

1.6 Orbital angular momentum of light

It is evident from Maxwell's wave equations that light carries both energy and linear momentum [52]. Apart from linear momentum, a light beam also possesses two different type of angular momentum *i.e.* spin angular momentum (SAM) and orbital angular momentum (OAM). The SAM has two values $\pm\hbar$ depending on the handedness of circularly polarized light, where $\hbar$ is the Planck constant. Whereas the OAM of light can have value ranges from $[-\infty, +\infty]$ and it appears due to the spiral motion of wavefront along the direction of beam propagation like a corkscrew. In the following, we demonstrate the appearance of OAM in a light beam using the linear momentum density [55, 56] which is defined as

$$\mathbf{p} = \frac{c}{4\pi}\langle \mathbf{E} \times \mathbf{B} \rangle. \tag{1.138}$$

We first derive the electric field ($\mathbf{E}$) and magnetic field ($\mathbf{B}$) of the light beam from a linearly polarised vector potential [56]

$$\mathbf{A}(x, y, z) = \hat{\mathbf{x}} u(x, y, z) e^{i(kz - \omega t)}, \tag{1.139}$$

where $\hat{\mathbf{x}}$ is the unit vector in the x-direction. The expression $u(x, y, z)$ represents the distribution of the field amplitude which satisfies the paraxial wave equation. We use the following two equations to obtain the expressions of $\mathbf{E}$ and $\mathbf{B}$

$$\mathbf{B}(x, y, z) = \nabla \times \mathbf{A}(x, y, z), \tag{1.140}$$

$$\nabla \times \mathbf{B}(x, y, z) = \frac{1}{c}\frac{\partial \mathbf{E}(x, y, z)}{\partial t}. \tag{1.141}$$

Note that in Eq. (1.141), we have used $\mathbf{D} = \mathbf{E}$ and $\mathbf{B} = \mathbf{H}$ because in free space both the electric and magnetic polarizations are zero. Now, we substitute $\mathbf{A}(x, y, z)$ in Eq. (1.140) and derive the expressions of $\mathbf{B}$ and $\mathbf{E}$ as shown below

$$\mathbf{B}(x, y, z) = ik\left(u\hat{\mathbf{y}} + \frac{i}{k}\frac{\partial u}{\partial y}\hat{\mathbf{z}}\right)e^{i(kz - \omega t)}, \tag{1.142}$$

$$\mathbf{E}(x,y,z) = ik(u\hat{\mathbf{x}} + \frac{i}{k}\frac{\partial u}{\partial x}\hat{\mathbf{z}})e^{i(kz-\omega t)}. \tag{1.143}$$

Next, we substitute Eq. (1.142) and Eq. (1.143) into Eq. (1.138) and calculate the linear momentum density which is basically the time averaged Poynting vector [56]

$$\mathbf{p} = \frac{c}{4\pi}\langle \mathbf{E}\times\mathbf{B}\rangle, \tag{1.144}$$

$$= \frac{c}{8\pi}(\mathbf{E}^*\times\mathbf{B} + \mathbf{E}\times\mathbf{B}^*), \tag{1.145}$$

$$= \frac{ick}{8\pi}(u\nabla u^* - u^*\nabla u) + \frac{ck^2|u|^2}{4\pi}\hat{\mathbf{z}}. \tag{1.146}$$

We consider u as a cylindrically symmetric field amplitude *i.e.* $u(r,\phi,z)$ which describes a Laguerre-Gaussian beam (LG^l_m)

$$u(r,\phi,z) = u_0(r,z)e^{il\phi}e^{\frac{ikr^2z}{2(z^2+z_0^2)}}e^{i(2m+l+1)\tan^{-1}(\frac{z}{z_R})}. \tag{1.147}$$

The phase part of $u(r,\phi,z)$ is very important and plays the key role in spiral motion of wavefront. Now, we substitute Eq. (1.147) into substitute Eq. (1.146) and obtain the linear momentum density as

$$\mathbf{p} = \frac{ck}{8\pi}\Big(\frac{2krz}{z^2+z_0^2}|u|^2\hat{\mathbf{r}} + \frac{2l}{r}|u|^2\hat{\boldsymbol{\phi}}\Big) + \frac{c}{4\pi}k^2|u|^2\hat{\mathbf{z}}. \tag{1.148}$$

In Eq. (1.148), $\hat{\mathbf{r}}$, $\hat{\boldsymbol{\phi}}$ and $\hat{\mathbf{z}}$ are the unit vectors along the r-, ϕ- and z-direction of a cylindrical coordinate system. Note that the linear momentum density possesses all three non-zero components along $\hat{\mathbf{r}}$, $\hat{\boldsymbol{\phi}}$ and $\hat{\mathbf{z}}$ direction

$$p_r = \frac{ck}{4\pi}\frac{krz}{z^2+z_0^2}|u|^2; \quad p_\phi = \frac{ck}{4\pi}\frac{l}{r}|u|^2; \quad p_z = \frac{c}{4\pi}k^2|u|^2 \tag{1.149}$$

The r-component of linear momentum density p_r relates to the beam spreading whereas the z-component p_z represents the linear momentum along the propagation direction [56]. The ϕ-component of linear momentum density p_ϕ spirals along the propagation direction and gives rise to OAM in the light beam [56]. In the following, we derive the angular momentum density, $\mathbf{L}$ from the linear momentum density, $\mathbf{p}$

$$\mathbf{L} = \mathbf{r}\times\mathbf{p},$$

$$\mathbf{L} = \frac{ck}{4\pi}\Big(-\frac{lz}{r}|u|^2\hat{\boldsymbol{r}} - \frac{krz_0^2}{z^2+z_0^2}|u|^2\hat{\phi} + l|u|^2\hat{\mathbf{z}}\Big). \tag{1.150}$$

It is evident from Eq. (1.150) that the angular momentum along the beam axis appears due to the non-zero ϕ-component such that $L_z = rp_\phi$. The ratio of angular momentum

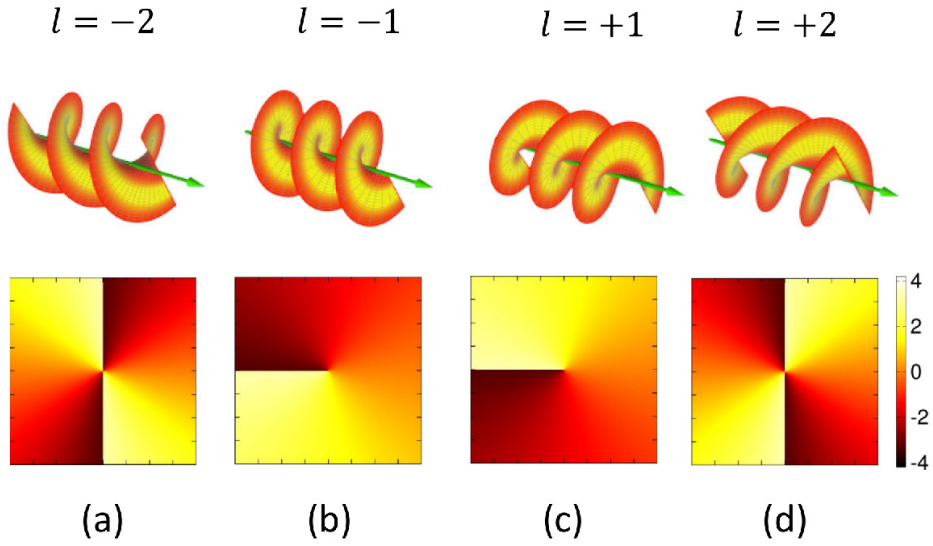

Fig. 1.12 The wavefront and azimuthal phase structure of OAM carrying vortex beam are shown. The value of OAM $|l|$ decides the number of intertwined helices in the wavefront and the number of phase singularity in the azimuthal phase structure. The sign of l determines the rotational direction of wavefront. The parameters are (a) $m = 0$, $l = -2$ (b) $m = 0$, $l = -1$ (c) $m = 0$, $l = +1$ (d) $m = 0$, $l = +2$.

to that of energy per unit length of beam [56] is obtained by integrating over x-y plane as shown below

$$\frac{L_z}{\mathrm{W}} = \frac{L_z}{cp_z} = \frac{\int\int rdrd\phi(\mathbf{r} \times \langle \mathbf{E} \times \mathbf{B} \rangle)_z}{c\int\int rdrd\phi\langle \mathbf{E} \times \mathbf{B} \rangle_z} = \frac{l}{\omega} \tag{1.151}$$

Eq. (1.151) shows that the light beam possesses an orbital angular momentum of l per photon. Note that the angular momentum can not be due to spin because the considered light beam is not circularly polarized. Therefore, it is justified that the Laguerre-Gaussian beam possesses a well-defined orbital angular momentum.

The OAM carrying light beam is also called vortex beam and they are distinguished as having an donut-shaped spatial profile with a central dark spot. The main feature of a vortex beam is the azimuthal phase dependence accounted by $e^{il\phi}$ term where l is the OAM of the beam. The wavefront of the vortex beam is composed of $|l|$ intertwined helices with a handedness given by the sign of l as shown in Fig. 1.12. Further, the azimuthal phase structure of the vortex beam carries phase singularity which depicts the location of undefined phase. Fig. 1.12 clearly indicates that the number of phase singularity is determined by the OAM of the beam. The most well known beam which carry OAM is Laguerre-Gaussian modes.

In 1992, Les Allen *et al.* pioneers the concept of optical OAM [56]. They demonstrate that a Laguerre-Gaussian laser mode has a well-defined OAM equal to $l\hbar$ per photon.

Since then the OAM of light has gained tremendous interest because it brings a new degree of freedom for photons and offers a huge space of variables theoretically ranges from $[-\infty, +\infty]$ [57–59]. The high dimensionality of OAM state is highly beneficial for light based communication [60, 61] and quantum information processing jobs [57]. The OAM carrying Laguerre-Gaussian light beam is also suitable for optical tweezer [62–67]. An optical tweezer is a tightly focused laser beam which traps and manipulates micro- to nano-scale particles at the beam focus. In 1995, Rubinsztein-Dunlop *et al.* trap and rotate a microscopic particle within the dark central minimum of a LG_m^l beam [62]. Further, this vortex beam works as an efficient tool for the fabrication of chiral nano-structures [68, 69]. A further significant application of vortex beam is the stimulated emission depletion (STED) based super-resolution microscopy. In this technique, the donut-shaped intensity profile of vortex laser beam suppresses fluorescence emission everywhere except the center of the donut pattern [70, 71]. This process effectively achieves the resolution beyond diffraction limit. All these diverse applications require high quality vortex laser beams with appropriate power and well-defined OAM at a suitable wavelength. Therefore, it is equally important to find out efficient methods that generate desired vortex laser beam. The most commonly used method is mode convertor which converts a Gaussian or Hermite-Gaussian modes into a vortex laser beam. The mode convertor mainly transforms a plane wavefront into a spiral wavefront using various tools such as phase plates [72, 73], cylindrical lens pairs [74], spatial light modulators (SLM) [75, 76]. Phase plates are fabricated in a way that its thickness increases gradually in a spiral fashion. It introduces adequate phase shift such that plane wavefront transforms into a spiral wavefront [72]. SLM is an electrically addressed light modulator based on liquid crystal which generates spiral wavefront by changing the phase of the incident light [76]. The direct method of vortex generation is also available in which vortex laser beam is generated directly from a laser cavity [77, 78].

Chapter 2

Four wave mixing based generation and control of light pulse

2.1 Introduction

The observation of atomic coherence in an atomic system leads us to uncover many spectacular optical effects. Among the most well known effect is EIT [2, 79] in which an opaque medium becomes eminently transparent for the probe field with the support of a control field. Diverse applications such as slowing and stopping of light [80–82], coherent storage and retrieval of light [83–86], Rydberg blockade induced interactions [87], diffraction control and guiding of light [29, 88], structured beam generation [30, 31], *etc.* have been documented using EIT. In multi-level atomic system, EIT enhances the nonlinear susceptibility which conducts us to use nonlinear optical regime in the investigation many nonlinear optical phenomena such as, Kerr nonlinearity [89, 90], self-phase modulation (SPM) [91], cross-phase modulation (XPM)[40, 92], four-wave mixing (FWM) [93–96], *etc.* In FWM process, three electro-magnetic fields interact in a nonlinear optical system and generate electro-magnetic field with a new frequency. Numerous experiments have been carried out to demonstrate the enhanced FWM process in multilevel atomic systems [97–102]. FWM process using EIT has been observed in both cold [103, 42, 99–102] and room temperature [98, 104] atomic system. Besides FWM process, enhanced higher order multi-wave mixing processes have been studied [105]. Hoonsoo *et al.* experimentally demonstrated EIT based six-wave mixing (SWM) signal in a N-type cold atomic system [106]. Recently an experimental observation of FWM signal in a N-type cold atomic system has been studied by Chang-Kai *et al.* at low light levels [107]. Aside from the atomic system, various hybrid systems composed of semiconductor quantum dots (SQD) and metallic

nanoparticles or photonic crystal nanocavity are used to study the FWM process [108, 109].

The four-level system not only generates new signal but also it permits the generated signal to propagate through the nonlinear medium along with the probe field under the condition of EIT [42, 107]. The effect of enhanced nonlinearity on these propagating signals through the atomic medium remains unexplored. Also the shape of the generated FWM signal and the progression during its propagation through the inhomogeneously broadened medium is not completely elucidated. In this chapter, we theoretically investigate all those questions in a simple four-level N-type atomic configuration as shown in Fig 2.1. Two weak probe field and a strong control field resonantly drive the system. In order to efficiently generate a FWM signal, it is essential that the phase-matching condition, $\vec{K}_{p1}+\vec{K}_{p2}=\vec{K}_c+\vec{K}_g$ is strictly fulfilled [98]. Here we conceive this by using a collinear geometry, which generates the FWM signal in the same direction as the probe field propagates. The steady state of the optical Bloch equations are numerically solved to study the atomic coherence created by the nonlinear atom-field interaction. The numerical result clearly shows gain in the FWM spectrum which indicates the possibility of signal generation. The frequency of the signal, ω_g related to the frequency of the probe fields, ω_{p1}, ω_{p2} and the frequency of the control field, ω_c by $\omega_g=\omega_{p1}-\omega_c+\omega_{p2}$. Note that the difference between two probe frequencies *i.e.*, $\Delta\omega_p=\omega_{p1}\sim\omega_{p2}<<\Delta\omega_{EIT}$ must be well contained within the EIT window otherwise the probe pulses will suffer distortion from different absorption and group velocity dispersion. Hence, the generated FWM signal will also suffer same kind of distortion due to different gain and group velocity dispersion.

Apart from the generation and control of the FWM signal, the storage and retrieval of this signal along with the probe has captivated enormous attention due to its potential application as an optical memory [110–114]. Recently many experiments demonstrate simultaneous storage and retrieval of both the signals in multi-level atomic system [112, 113, 115]. But the correlation between the input and the output pulse shape has not yet been explored in details. It is noticeable from the previous demonstrations that the retrieved FWM signal does not preserve its predefined shape and also its intensity is reduced considerably. We overcome these limitations by considering a non-degenerate atomic system in which two probe and one control field are interacting nonlinearly. In this chapter, we demonstrate the shape preserving storage and retrieval of the FWM signal without compromising its intensity. We also find that the storage and retrieval process is robust with both the adiabatic and non-adiabatic switching of the control field.

The arrangement of the chapter is as follows. In section 2.2.1, we configure the physical model and describe the system using a semiclassical theory. In section 2.2.2, we discuss

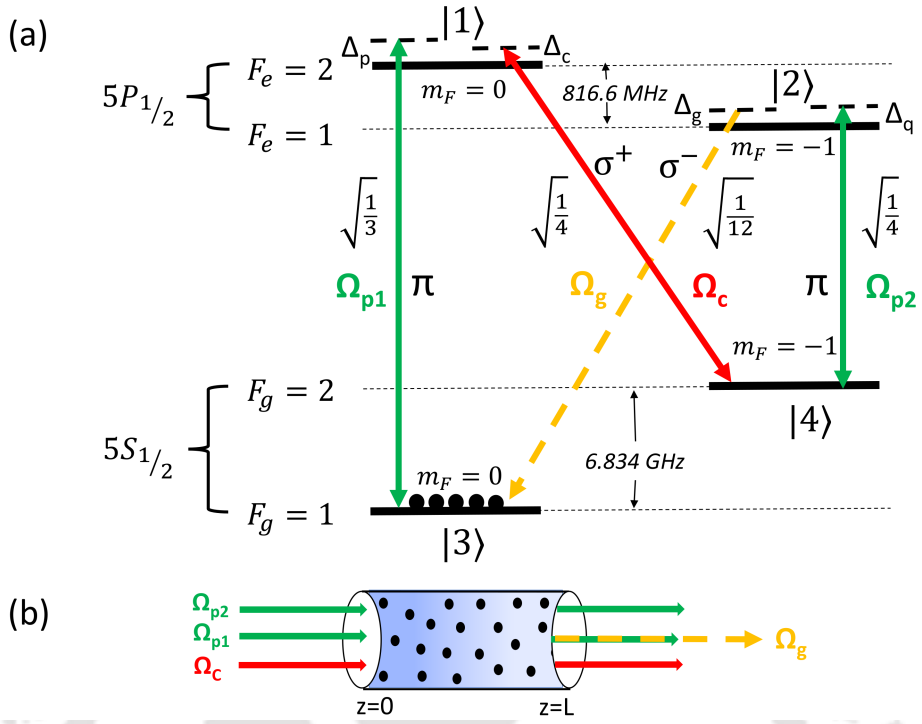

Fig. 2.1 (a) Schematic representation of the proposed N-type atomic energy levels of ^{87}Rb D_1-line transition. Two metastable ground states are defined as $|3\rangle = |F_g = 1, m_F = 0\rangle$ and $|4\rangle = |F_g = 2, m_F = -1\rangle$. Two excited states are defined as $|1\rangle = |F_e = 2, m_F = 0\rangle$ and $|2\rangle = |F_e = 1, m_F = -1\rangle$. Two probe fields ($\Omega_{p1}$ and Ω_{p2}) and one control field generate a FWM signal with frequency $\omega_g = \omega_{p1} - \omega_c + \omega_{p2}$. The square root terms are the coupling strengths (Clebsch-Gordan coefficient) of the corresponding transitions. (b) A simple illustration of the model system.

the dynamical equations of motion for the N-type system using Liouville's equation. In section 2.2.3, we derive the pulse propagation equations for the optical fields. In section 2.3, we investigate the generation and control of the FWM signal. In section 2.4, storage and retrieval of the FWM signal is demonstrated. In section 2.5, we derive the analytical expression of the nonlinear coherence under weak probe approximation in order to explain the FWM scheme. Finally in section 2.6, we briefly conclude our work.

2.2 Theoretical Model

2.2.1 Model Configuration

In this work, the four wave mixing mechanism has been exploited for the generation and control of an optical signal. The model system consists of an inhomogeneously broadened four level ^{87}Rb atomic system interacting with three co-propagating optical

fields as shown in Fig 2.1. The atomic transitions $|1\rangle \leftrightarrow |3\rangle$ and $|2\rangle \leftrightarrow |4\rangle$ are coupled by two probe field of frequency ω_{p1}, ω_{p2} whereas a strong control field with frequency ω_c couples $|1\rangle \leftrightarrow |4\rangle$ transition. These optical fields are defined as

$$\vec{E}_j(z,t) = \hat{e}_j \mathcal{E}_{0j}(z,t) e^{i(k_j z - \omega_j t)} + c.c., \tag{2.1}$$

where $\mathcal{E}_{0j}(z,t)$ is the space-time dependent amplitude, $k_j = \omega_j/c$ is the propagation constant along z-direction and $\hat{e}_j$ is the polarisation unit vector of the optical field. The subscript, $j \in \{p1, p2, c\}$ indicates the two probe field and control field respectively. The Hamiltonian describing the interaction between the four atomic level system with the two optical fields under electric-dipole approximation is as given below

$$\begin{aligned} H^{'} &= \hbar\omega_{13} |1\rangle\langle 1| + \hbar(\omega_{13} - \omega_{14}) |4\rangle\langle 4| + \hbar(\omega_{13} - \omega_{14} + \omega_{24}) |2\rangle\langle 2| \\ &- \hbar\Omega_{p1} e^{-i\omega_{p1}t} |1\rangle\langle 3| - \hbar\Omega_c e^{-i\omega_c t} |1\rangle\langle 4| - \hbar\Omega_{p2} e^{-i\omega_{p2}t} |2\rangle\langle 4| + h.c., \end{aligned} \tag{2.2}$$

where the Rabi frequencies of the probe and control are defined by

$$\Omega_{p1} = \frac{\hat{d}_{13}.\hat{e}_{p1}}{\hbar}\mathcal{E}_{0p1};\ \Omega_{p2} = \frac{\hat{d}_{24}.\hat{e}_{p2}}{\hbar}\mathcal{E}_{0p2};\ \Omega_c = \frac{\hat{d}_{14}.\hat{e}_c}{\hbar}\mathcal{E}_{0c}$$

The dipole moments for the atomic transitions between states $|1\rangle \leftrightarrow |3\rangle$, $|2\rangle \leftrightarrow |4\rangle$ and $|1\rangle \leftrightarrow |4\rangle$ are denoted by $\hat{d}_{13}$, $\hat{d}_{24}$, and $\hat{d}_{14}$, respectively. Note that the Clebsch-Gordan coefficients of the considered level scheme, $|\hat{d}_{13}|/|\hat{d}_{24}| = \sqrt{4/3}$ approximately implies that $|\hat{d}_{13}| \approx |\hat{d}_{24}|$ [116, 117, 107, 99, 115]. So, we can safely consider that $\Omega_{p1} \approx \Omega_{p2} = \Omega_p$. The probe pulses ($\Omega_{p1}$, Ω_{p2}) have different frequency (ω_{p1}, ω_{p2}) but they possess similar intensity, temporal profile and polarisation.

We perform the following unitary transformation in order to remove the explicit time dependence from the Hamiltonian

$$H = U^{\dagger} H^{'} U - i\hbar U^{\dagger} \frac{\partial U}{\partial t}, \tag{2.3}$$

where U is defined as

$$U = e^{-i(\omega_{p1}|1\rangle\langle 1| + (\omega_{p1} - \omega_c)|4\rangle\langle 4| + (\omega_{p1} - \omega_c + \omega_{p2})|2\rangle\langle 2|)t}. \tag{2.4}$$

Now the transformed Hamiltonian H takes the following form

$$\begin{aligned} H &= -\hbar\Delta_p |1\rangle\langle 1| - \hbar(\Delta_p - \Delta_c) |4\rangle\langle 4| - \hbar(\Delta_p - \Delta_c + \Delta_q) |2\rangle\langle 2| \\ &- \hbar\Omega_p |1\rangle\langle 3| - \hbar\Omega_c |1\rangle\langle 4| - \hbar\Omega_p |2\rangle\langle 4| + h.c., \end{aligned} \tag{2.5}$$

where $\Delta_p = \omega_{p1} - \omega_{13}$, and $\Delta_q = \omega_{p2} - \omega_{24}$ are the detunings of the probe field with $|1\rangle \leftrightarrow |3\rangle$ and $|2\rangle \leftrightarrow |4\rangle$ transitions, respectively. The detuning due to the control field corresponding to $|1\rangle \leftrightarrow |4\rangle$ transition is given by $\Delta_c = \omega_c - \omega_{14}$.

2.2.2 Dynamical Equations

We use Liouville's equation to account for the various radiative and non-radiative decay processes of the atomic system. The decay of the atomic system is caused by various mechanisms such as flight-through broadening, population exchange, and atom-atom and atom-wall collisions. To govern the response of the atomic populations and coherences of the four-level atomic system, the following density matrix equations are employed

$$\dot{\rho} = -\frac{i}{\hbar}[H, \rho] + \mathcal{L}_\rho \tag{2.6}$$

where the second term represents the decay processes that can be determined by

$$\mathcal{L}\rho = \mathcal{L}_r\rho + \mathcal{L}_c\rho \tag{2.7}$$

with

$$\mathcal{L}_r\rho = -\sum_{i=1}^{2}\sum_{j=3}^{4}\frac{\gamma_{ji}}{2}\left(|i\rangle\langle i|\,\rho - 2\,|j\rangle\langle j|\,\rho_{ii} + \rho\,|i\rangle\langle i|\right). \tag{2.8}$$

The spontaneous decay rates from the excited state $|i\rangle$, $(i \in 1, 2)$ to the ground state $|j\rangle$, $(j \in 3, 4)$ are denoted by γ_{ji} in Eq.(2.8). The dephasing in the ground state [$\mathcal{L}_c\rho$ in Eq.(2.7)] is due to collision at a rate γ_c. Now the dynamics of the model system can be obtained in the following form

$$\begin{aligned}
\dot{\rho}_{11} &= -(\gamma_{31} + \gamma_{41})\rho_{11} + i\Omega_p\rho_{31} + i\Omega_c\rho_{41} - i\Omega_p^*\rho_{13} - i\Omega_c^*\rho_{14},\\
\dot{\rho}_{12} &= -[i(\Delta_q - \Delta_c) + \frac{1}{2}(\gamma_{31} + \gamma_{41} + \gamma_{32} + \gamma_{42})]\rho_{12} + i\Omega_p\rho_{32} + i\Omega_c\rho_{42} - i\Omega_p^*\rho_{14},\\
\dot{\rho}_{13} &= [i\Delta_p - \frac{1}{2}(\gamma_{31} + \gamma_{41})]\rho_{13} + i\Omega_p(\rho_{33} - \rho_{11}) + i\Omega_c\rho_{43},\\
\dot{\rho}_{14} &= [i\Delta_c - \frac{1}{2}(\gamma_{31} + \gamma_{41})]\rho_{14} + i\Omega_p(\rho_{34} - \rho_{12}) + i\Omega_c(\rho_{44} - \rho_{11}),\\
\dot{\rho}_{22} &= -(\gamma_{32} + \gamma_{42})\rho_{22} + i\Omega_p\rho_{42} - i\Omega_p^*\rho_{24},\\
\dot{\rho}_{23} &= [i(\Delta_p - \Delta_c + \Delta_q) - \frac{1}{2}(\gamma_{32} + \gamma_{42})]\rho_{23} + i\Omega_p(\rho_{43} - \rho_{21}),\\
\dot{\rho}_{24} &= [i\Delta_q - \frac{1}{2}(\gamma_{32} + \gamma_{42})]\rho_{24} + i\Omega_p(\rho_{44} - \rho_{22}) - i\Omega_c\rho_{21},\\
\dot{\rho}_{33} &= \gamma_{31}\rho_{11} + \gamma_{32}\rho_{22} + i\Omega_p^*\rho_{13} - i\Omega_p\rho_{31}
\end{aligned}$$

$$\dot{\rho}_{34} = -[i(\Delta_p - \Delta_c) + \gamma_c]\rho_{34} + i\Omega_p^*\rho_{14} - i\Omega_p\rho_{32} - i\Omega_c\rho_{31},$$
$$\dot{\rho}_{44} = -(\dot{\rho}_{11} + \dot{\rho}_{22} + \dot{\rho}_{33})$$
$$\dot{\rho}_{ij} = \dot{\rho}_{ji}^* \tag{2.9}$$

where the overdot stands for the time derivative and star $(*)$ denotes the complex conjugate. The atoms in the room temperature vapor cell have random thermal motion and have a finite velocity associated with each. Due to finite velocity, each atom experiences different Doppler shift in laser field detuning *i.e.* $\Delta^{'} = \Delta \pm kv$ where the sign of frequency shift $\pm kv$ indicates the motion of atoms either counter propagating or co-propagating. The presence of different Doppler shifts make the atomic susceptibility inhomogeneously broadened. In presence of Doppler shift, the probe and control field detuning are modified to $\Delta_p^{'} = \Delta_p - k_{p1}v$, $\Delta_q^{'} = \Delta_q - k_{p2}v$, $\Delta_c^{'} = \Delta_c - k_c v$, respectively. Therefore, these effects can be incorporated into the equations of motion (5.11) by taken into account the averaging over a Maxwell velocity distribution. Hence the velocity averaging of the atomic coherences $\langle\rho_{ij}(z,t)\rangle$ can be expressed as

$$\langle\rho_{ij}(z,t)\rangle = \int \rho_{ij}(z,v,t)\mathcal{P}(kv)d(kv), \tag{2.10}$$

where $\mathcal{P}(kv)d(kv)$ is probability that an atom has a velocity between v and $v + dv$ and obeyed by the Maxwell-Boltzmann velocity distribution

$$\mathcal{P}(kv)d(kv) = \frac{1}{\sqrt{2\pi D^2}} e^{-\frac{(kv)^2}{2D^2}} d(kv). \tag{2.11}$$

The Doppler line width D is given by $D = \sqrt{k_B T \nu_c^2/Mc^2}$, where M is the atomic mass, k_B is the Boltzmann constant and T is the thermal equilibrium temperature. At room temperature (T=300K), the Doppler width, D is 37γ for ^{87}Rb atoms.

2.2.3 Pulse Propagation Equations

In this section, we use Maxwell's equations to govern the spatio-temporal evaluation of an optical field through a nonlinear medium. The wave equation for the probe, control and generated fields can be expressed as

$$\left(\nabla^2 - \frac{1}{c^2}\frac{\partial^2}{\partial t^2}\right)\vec{E} = \frac{4\pi}{c^2}\frac{\partial^2\vec{\mathcal{P}}}{\partial t^2}, \tag{2.12}$$

where $\vec{E} = \vec{E}_{p1} + \vec{E}_{p2} + \vec{E}_c + \vec{E}_g$ is the total field and its induced polarization is $\vec{\mathcal{P}}$. The source term $\vec{\mathcal{P}}$ that appears in the right hand side of Eq.(3.14) is the origin of linear and non-linear response of the medium. The macroscopic polarization $\vec{\mathcal{P}}$ can be

defined in terms of the atomic coherences as

$$\vec{\mathcal{P}} = \mathcal{N}(\vec{d}_{13}\rho_{13}e^{-i\omega_{p1}t} + \vec{d}_{24}\rho_{24}e^{-i\omega_{p2}t} + \vec{d}_{14}\rho_{14}e^{-i\omega_c t} + \vec{d}_{23}\rho_{23}e^{-i\omega_g t} + c.c.,) \tag{2.13}$$

where $\mathcal{N}$ is the atomic density. Note that the atomic density under consideration is weak, otherwise local field correction need to be taken into account. Under slowly-varying envelope approximation (SVEA), Eqs.(3.14) can be reformulated as

$$\left(\frac{\partial}{\partial z} + \frac{1}{c}\frac{\partial}{\partial t}\right)\Omega_p = i\eta\left\langle \frac{1}{3}\rho_{13}(z,t) + \frac{1}{4}\rho_{24}(z,t)\right\rangle, \tag{2.14}$$

$$\left(\frac{\partial}{\partial z} + \frac{1}{c}\frac{\partial}{\partial t}\right)\Omega_g = i\eta\left\langle \frac{1}{12}\rho_{23}(z,t)\right\rangle. \tag{2.15}$$

We neglect the propagation of the control field because its intensity is much higher than the probe and FWM signal intensity. The coupling constants for the probe and generated field are defined in terms of reduced coupling constant, $\eta = 2\pi k\mathcal{N}|\vec{d}_{ij}^{R}|^2/\hbar$ as follows

$$\eta_{p1} = \frac{\eta}{3} \quad ; \quad \eta_{p2} = \frac{\eta}{4} \quad ; \quad \eta_g = \frac{\eta}{12} \tag{2.16}$$

where $|\vec{d}_{ij}^{R}|$ is the reduced matrix element. The spontaneous decay rates from the excited states into the ground states are also modified due to different coupling strength and can be written as

$$\gamma_{31} = \frac{\gamma}{3}; \quad \gamma_{41} = \frac{\gamma}{4}; \quad \gamma_{32} = \frac{\gamma}{12}; \quad \gamma_{42} = \frac{\gamma}{4} \tag{2.17}$$

where reduced spontaneous decay rate is defined as $\gamma = 4|\vec{d}_{ij}^{R}|^2k^3/3\hbar$. The angular bracket denotes a statistical average over the velocity distribution of the atom. We introduce the following co-moving coordinate system in order to perform numerical computation:

$$\tau = t - \frac{z}{c}, \quad \xi = z. \tag{2.18}$$

Therefore, the expressions within the round bracket of Eq.(2.15) can be easily substituted by $\partial/\partial\xi$ in the frame of moving coordinate system. Subsequently, simultaneous solutions of Bloch Eqs.(5.11) and Maxwell's Eqs.(2.15) in space-time coordinate explore the dynamical progression of the optical fields inside the medium.

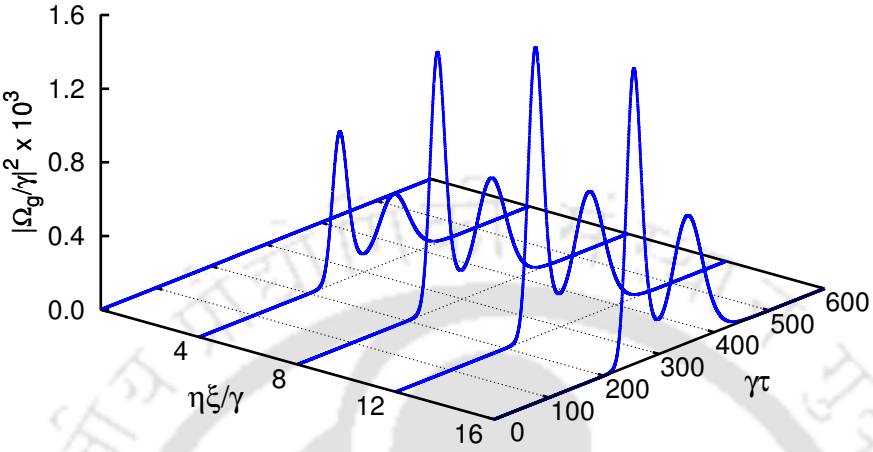

Fig. 2.2 Propagation dynamics of the generated FWM signal as function of position and time. The parameters are $\Omega_p^0 = 0.3\gamma$, $\Omega_c^0 = 3.0\gamma$, $\mathcal{N} = 4 \times 10^{10}$atoms/cm^3, $\lambda = 7.95 \times 10^{-5}$cm, $\Delta_p = \Delta_c = \Delta_q = \Delta_g = 0$, $\sigma_1 = 30/\gamma$, $\sigma_2 = 50/\gamma$, $\gamma\tau_1$=250, $\gamma\tau_2$=350, $D = 37\gamma$, T=300K, $\gamma_c \approx 1 \times 10^3$ Hz.

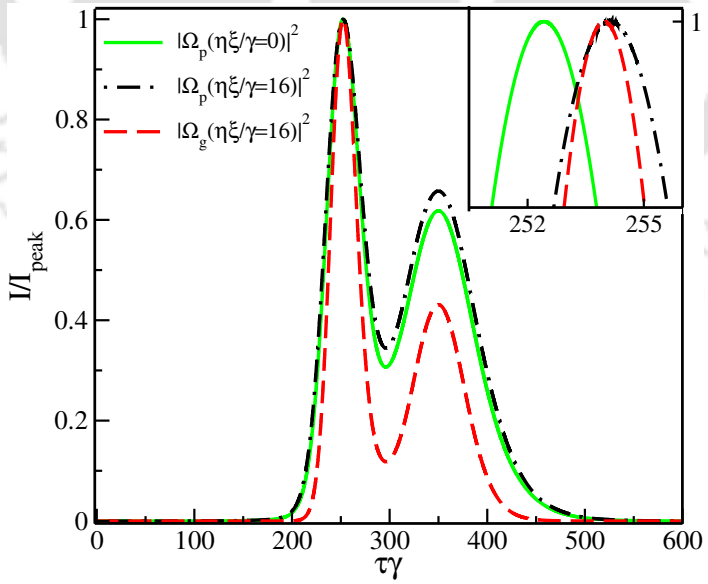

Fig. 2.3 Normalised intensity profile, I/I_{peak} of the complicated shaped probe pulse and FWM signal at input ($\eta\xi/\gamma = 0$) and output ($\eta\xi/\gamma = 16$) boundary of the medium. Temporal peak position of the output pulses are shifted at $\gamma\tau$=252.5. Inset figure shows the actual peak location. All other parameters are same as in Fig. (2.2).

2.3 Generation and control of FWM signal

In this section, we proceed with numerical simulation of Maxwell-Bloch equations to reveal the generation of optical field and its control by exploiting FWM mechanism. We have adopted Cash-Karp Runge-Kutta method in order to solve coupled partial differential equations. We begin with a complicated shaped input probe pulse which is a combination of Gaussian and secant hyperbolic pulse having different widths ($\sigma_1 = 30/\gamma$, $\sigma_2 = 50/\gamma$). The time dependent envelope of the probe field at the entry face of the medium can be written as

$$\Omega_p(\xi = 0, \tau) = \Omega_p^0 \left[e^{-(\frac{\tau-\tau_1}{\sigma_1})^2} + sech(\frac{\tau - \tau_2}{\sigma_2}) \right]. \tag{2.19}$$

where Ω_p^0, σ_i, $i \in \{1, 2\}$ and τ_i, $i \in \{1, 2\}$ are the amplitude, temporal width and peak location of the complicated shaped probe field, respectively. In our entire computation, we have assumed that the amplitude of control field ($\Omega_c^0 = 3.0\gamma$) is larger than the amplitude of the probe field ($\Omega_p^0 = 0.3\gamma$) and subsequently the dynamical evolution of control field can be neglected. Initially all atoms are occupied in the $|3\rangle$ state whereas all other states are unoccupied for $\xi \in (0, L)$.

Our first finding on the generation of optical pulse in the presence of a continuous wave (cw) control field is shown in Fig. 2.2. Figure 2.2 shows the temporal variation of generated field at different propagation distances. It is clear from Fig. 2.2 that the amplitude of the generated field increases gradually and takes the probe field shape while propagating along the medium. Note that temporal shape of the generated field remains unchanged after it attains saturation intensity. For the sake of generality, we compare the temporal shape of the generated field with the probe field as in Fig. 2.3. It can be seen that the time dependent envelope of the generated field is same as the input probe field, except its width is a scaled version of the probe pulse. We also notice that the temporal shapes of both generated and probe fields propagate through the medium without absorption and distortion. Therefore, only the cw control field efficiently acquires the temporal shape of probe field to generate signals and protect them during propagation.

Further, we have calculated the efficiency of the FWM process, η_{eff} as a ratio of energy of the output FWM generated field and energy of the input probe field [118]

$$\eta_{eff} = \frac{\int_{-\infty}^{\infty} |\vec{E}_g(z = L, \tau)|^2 \, d\tau}{\int_{-\infty}^{\infty} \sum_{i=1}^{2} |\vec{E}_{pi}(z = 0, \tau)|^2 \, d\tau}; \tag{2.20}$$
$$|\vec{E}_g|^2 = \frac{\hbar^2 |\Omega_g|^2}{|\vec{d}_{23}|^2}; \quad |\vec{E}_{pi}|^2 = \frac{\hbar^2 |\Omega_p|^2}{|\vec{d}_{13}|^2}$$

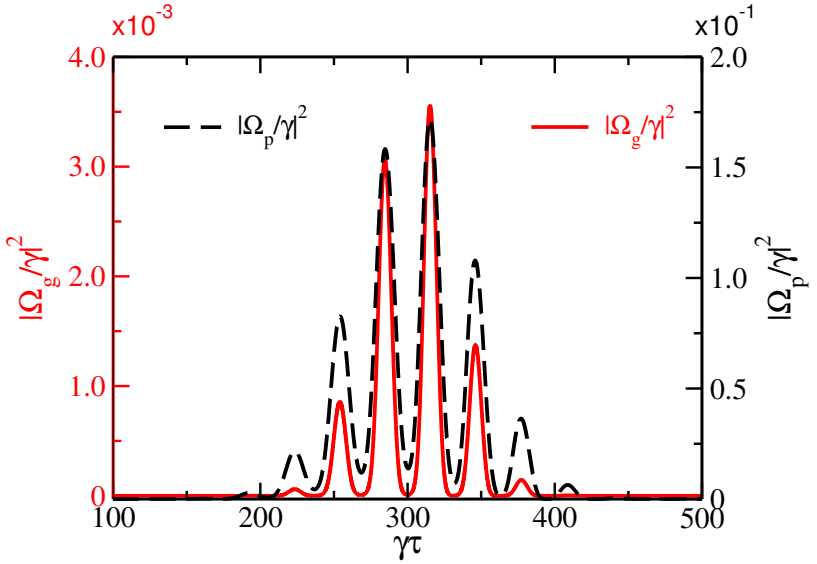

Fig. 2.4 Intensity profile of the amplitude modulated Gaussian shaped probe pulse and generated FWM signal at output ($\eta\xi/\gamma = 16$) boundary of the medium. The parameters for the probe pulse are $\Omega_p^0 = 0.3\gamma$, $m_a = 0.65$, $w_m = \gamma/5$, $\sigma_p = 75/\gamma$ and $\gamma\tau_0$=300. Other parameters are same as in Fig. (2.2).

The efficiency of the FWM process, η_{eff} is 2.8%. The efficiency also depends on the control field intensity and can be enhanced further by reducing the control field intensity as shown in Fig. 3.6 in the manuscript. However, the linewidth of the EIT window also depends on Ω_c and can be expressed as $(\Delta\omega)_{EIT} \propto |\Omega_c|^2/\gamma$ [119] which limits the FWM efficiency. This limitation can be avoided by considering a suitable spectral width of the probe pulse.

In order to prove the robustness of the model system, we next consider input probe field to be an amplitude modulated Gaussian pulse. For this purpose, the input envelope for the probe field is expressed as follows:

$$\Omega_p(\xi = 0, \tau) = \Omega_p^0 \left(1 + m_a \cos \omega_m t\right) e^{-(\frac{\tau-\tau_0}{\sigma_p})^2} \tag{2.21}$$

where m_a and ω_m are termed as the depth of modulation and frequency of the modulating signal, respectively. In practice, ω_m is small compared to the carrier frequency ω_p of the probe pulse. Figure 2.4 depicts the intensity profile of the probe and generated fields as a function of $\gamma\tau$ at propagation distance $\eta\xi/\gamma = 16$. This figure confirms precisely that the generated FWM signal gets its shape from the envelope of the probe field and propagates as a shape preserving pulse. However the time resolution of the generated amplitude modulated pulse is higher as compared to the probe pulse.

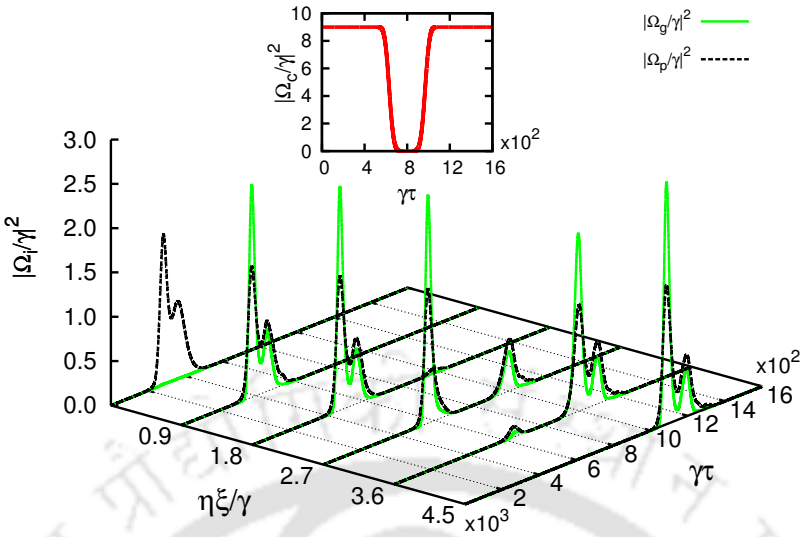

Fig. 2.5 Storage and retrieval of complicated shaped probe pulse (dashed black line, $i = p$) and generated FWM signal (solid green line, $i = g$) are demonstrated. We multiply 10^1 and 10^3 with the probe field intensity ($|\Omega_p/\gamma|^2$) and FWM signal intensity ($|\Omega_g/\gamma|^2$) respectively. Inset figure shows intensity profile of the control field (solid red). The parameters are $\sigma_1 = 30/\gamma$, $\sigma_2 = 50/\gamma$, $\gamma\tau_1$=280, $\gamma\tau_2$=360, $\sigma_c = 160/\gamma$, $\gamma\tau_c = 800$, $\alpha = 4$ and all other parameters are same as in Fig. 2.2.

2.4 Storage and Retrieval of EM radiations

In the previous section, we have demonstrated how the time independent control field efficiently generates and controls the propagaton of FWM signal. Here we explore the dynamics of the generated field in presence of time dependent profile of control field. We address this issue by considering the temporal profile of control field to be of inverted super-Gaussian shape which is defined as:

$$\Omega_c(\xi = 0, \tau) = \Omega_c^0\Big[1 - e^{-\left(\frac{\tau-\tau_c}{\sigma_c}\right)^{\alpha}}\Big], \tag{2.22}$$

where the parameter α regulates the rapidity of the switching action of the control field as shown in the inset of Fig. 2.5. Switching off and on of control field intensity in time domain holds the key of storage and retrieval process. Figure 2.5 displays the spatio-temporal characteristics of probe and FWM fields. The initial profile of the probe field is chosen as a combination of Gaussian and secant hyperbolic pulse having different widths. As seen from Fig. 2.5 the probe field intensity gradually diminishes due to dynamical reduction of control intensity. Simultaneously FWM signal is formed and its spatio-temopral evolution follows the same dynamical behaviour as the probe field. The control field not only generates the FWM signal but also enables the storage

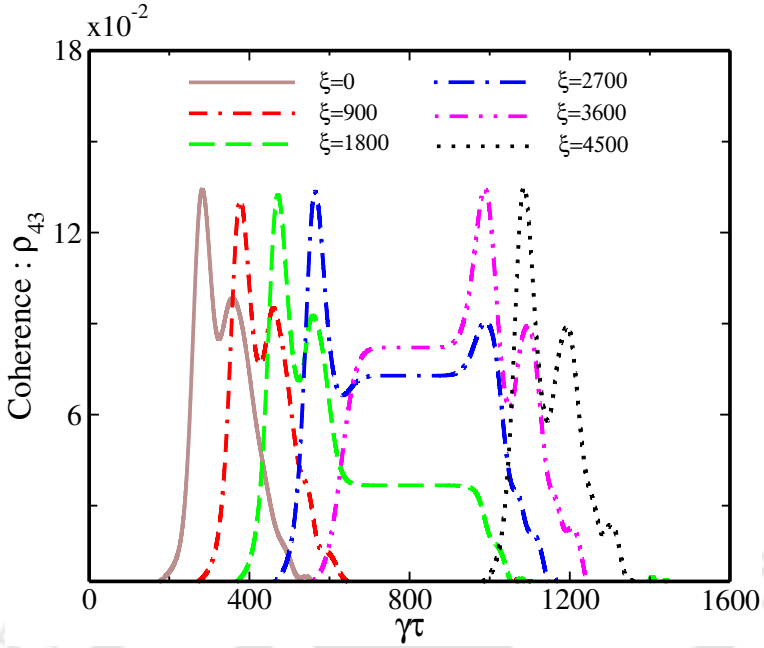

Fig. 2.6 The temporal profile of ground state atomic coherence, ρ_{43} is plotted as a function of time for different propagation distances. All parameters are same as in Fig. 2.5.

and retrieval of the signal along with the probe pulse by temporal variation of its own intensity. The intensity lowering (rising) to zero (maximum) with time produces switching off (on) of the control field as shown in inset of Fig. 2.5. The spatio-temporal evolution of probe and generated signals in the presence of super Gaussian shaped control field is shown in Fig 2.5. The signal and probe fields are depicted by solid green and dashed black lines, respectively. Figure 2.5 shows that the generation of signal field is accomplished within a short length of medium in the presence of both control and probe fields. It is also evident from Fig. 2.5 that storage of signal and probe fields start as soon as both peaks experience the falling intensity of the control field. Hence the intensities of both signal and probe fields are gradually stored by adiabatic switching off the control field during the propagation through the atomic medium. The storing of the fields can be completed by making intensity of control field zero. The stored pulses can be retrieved on demand by switching on the control field. The retrieval process of stored fields can be initiated by switching on of the control field at a later time. The maximum intensity of the control field leads to retrieval of both probe and signal from the medium without loss of generality.

Next we investigate the ground state atomic coherence which is solely responsible for the storage and retrieval of electromagnetic radiation in an atomic medium [120]. Subsequently we have plotted the atomic coherence ρ_{43} as a function of time at different propagation distances as shown in Fig. 2.6. As depicted from Fig. 2.6, at entry face

of the medium $\eta\xi/\gamma = 0$, ρ_{43} takes the temporal shape of probe field in presence of constant control. The atomic coherence attains its maximum value when control field is switched off. The probe and signal pulses are stored inside the medium in the form of ground atomic coherence by switching off the control field. This coherence (ρ_{43}) is well preserved inside the medium and efficiently can be retrieved before it decays at a rate of γ_c. The atomic coherence starts generating the replica of the stored pulses after the control field is switched on. The Raman scattering between stored atomic coherence and control field intensity produces back the stored signal. Therefore, the atomic coherence plays the main role behind the storage and retrieval of the probe as well as the FWM signal.

2.5 Analysis and Discussion

2.5.1 Perturbative Analysis

In this section, we derive an analytical expression for the atomic coherence which can successfully explain the generation of signal due to four wave mixing in four level atomic system. The perturbative expression for the coherence and population is determined under weak probe approximation ($\Omega_p < \Omega_c$) that are correct in all orders for the control field of Rabi frequencies Ω_c and 2^{nd} order in probe Rabi frequencies Ω_p. The solutions of the density matrix equations can be approximated as

$$\rho_{ij} = \rho_{ij}^{(0)} + \Omega_p\rho_{ij}^{(1)} + \Omega_p^*\rho_{ij}^{(2)} + \Omega_p^2\rho_{ij}^{(3)} + |\Omega_p|^2\rho_{ij}^{(4)} + \Omega_p^{*2}\rho_{ij}^{(5)} \tag{2.23}$$

where $\rho_{ij}^{(0)}$ describes the solution in the absence of Ω_p and $\rho_{ij}^{(k)}$, $k \in \{1, 2, 3, 4, 5\}$ is the higher order solution in the presence of weak Ω_p. The steady-state value of the atomic coherence, ρ_{23} can be expressed by the following expression

$$\rho_{23} = \frac{i\Omega_p^2\Omega_c^*}{\Gamma_1\Gamma_3[\Gamma_2 + \frac{\Omega_c^2}{\Gamma_1}]}, \tag{2.24}$$

where

$$\begin{aligned}
\Gamma_1 &= i\Delta_p - \frac{\gamma_{31} + \gamma_{41}}{2}, \\
\Gamma_2 &= i(\Delta_p - \Delta_c) - \gamma_c, \\
\Gamma_3 &= i(\Delta_p - \Delta_c + \Delta_q) - \frac{\gamma_{32} + \gamma_{42}}{2}.
\end{aligned} \tag{2.25}$$

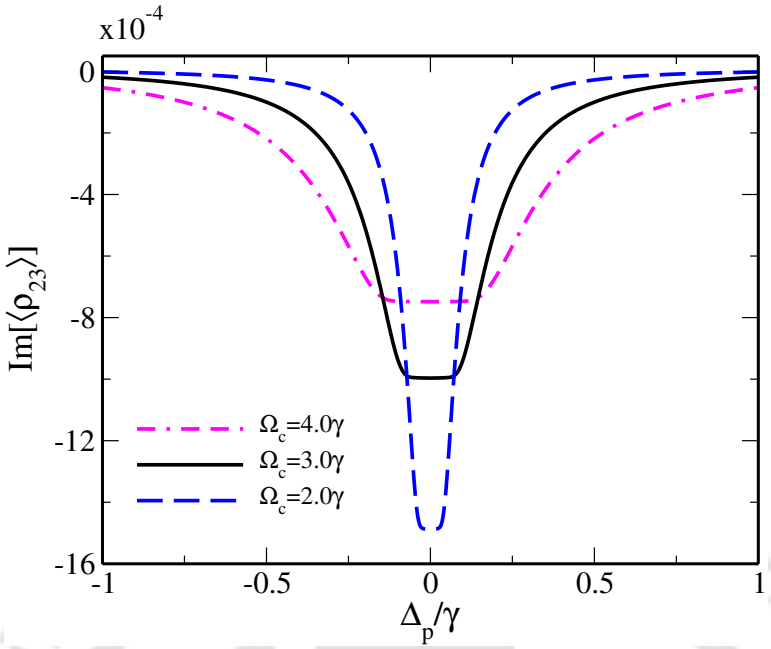

Fig. 2.7 Imaginary part of nonlinear Doppler averaged coherence, $\langle\rho_{23}\rangle$ as a function of Δ_p in units of γ for various values of Ω_c. The parameters are $\Omega_p^0 = 0.3\gamma$, $\Omega_c^0 = 3.0\gamma$, $\Delta_c = \Delta_q = 0$, $D = 37\gamma$, T=300K, $\gamma_c \approx 1 \times 10^3$ Hz, $\gamma = 5.746 \times 10^6$ Hz.

The above expression corresponds to the four wave mixing in a system of four level atoms and produces a frequency ω_g=$\omega_{p1} - \omega_c + \omega_{p2}$. The induced nonlinear atomic polarization $\vec{P}^{NL}$ is expressed as $\vec{P}^{NL} = \chi^{(3)}(\omega_g)\vec{E}_{p1}\vec{E}_c^*\vec{E}_{p2}$ where $\chi^{(3)}(\omega_g)$ is a 3$^{\text{rd}}$ order nonlinearity. Under the Doppler-broaden, the nonlinear susceptibility $\chi^{(3)}(\omega_g)$ can be written as

$$\langle\chi^{(3)}(\omega_g)\rangle = \frac{\mathcal{N}|\vec{d}_{23}||\vec{d}_{13}|^2|\vec{d}_{14}|}{\hbar^3|\Omega_p|^2\Omega_c^*}\langle\rho_{23}\rangle, \tag{2.26}$$

where $\mathcal{N}$ is the atomic density.

2.5.2 Nonlinear Susceptibility

We next study the nonlinear susceptibility of the medium and its variation with control field intensity. We use weak-approximated analytical solution (2.24) to obtain response of the generated signal coherence as shown in Fig.3.6. The plots in Fig.3.6 show gain which ensures that a new optical field generation is possible even in the weak probe regime. The gain of the generated signal can be enhanced by reducing the control field intensity as clearly shown in Fig.3.6 with double dash dot magenta curve ($\Omega_c = 4.0\gamma$), solid black curve ($\Omega_c = 3.0\gamma$) and dash blue curve ($\Omega_c = 2.0\gamma$). The condition of stable dark state *i.e.* $\Omega_p < \Omega_c$ becoming feeble as the control field intensity is reduced significantly as causes the population to leave the dark state,

$|3\rangle$ and populate the excited states $|1\rangle$ and $|2\rangle$ which enhances the gain of FWM signal. Simultaneously, the probe pulse suffers absorption and distortion due to narrowness of the medium transmission window at low control field intensity because $(\Delta\omega)_{EIT} \propto |\Omega_c|^2/\gamma$. However, the transmission and distortion of the probe pulse can be avoided by considering a suitable spectral width of the probe pulse so that the spectrum of the probe pulse will be well contained within the transparency window of the medium. Hence the efficiency of nonlinear signal generation can be enhanced with a suitable value of control field intensity.

2.6 Conclusion

In conclusion, we have demonstrated an efficient generation and control of a non-degenerate FWM signal in a N-type inhomogeneously broadened atomic medium. A strong control field and two weak probe fields tailored the medium susceptibility with a gain profile which enable us to generate the FWM signal. This scheme generates a scaled copy of the input probe pulse which travels through the atomic medium along with the probe field without changing its shape and intensity. We further study the propagation dynamics, storage and retrieval of the generated FWM signal in the nonlinear medium by considering a complicated combination of Gaussian and secant hyperbolic shape as well as amplitude modulated signal. This unique features have important applications in signal processing in optical communication as well as in quantum information science [43, 44].

Chapter 3

Four-wave mixing based orbital angular momentum translation

3.1 Introduction

Optical vortex beams carrying singularities in phase has emerged as a topic of intensive study in the quantum domain [58, 59]. The azimuthal varying phase structure $e^{il\phi}$ of the beam corresponds to the origin of the orbital angular momentum [121]. Various methods such as cylindrical lens pairs [122], computer generated hologram [75], spatial light modulator [123] *etc*., have been utilized to produce phase singularity. Light beam possessing vortex singularity has broad applications in optical communication [57, 124], super-resolution imaging [125, 126], optical tweezers [62, 67, 127], nonlinear phenomena [128–130], *etc*. Several systems including multi-core supermode optical fiber [131, 132], photonic crystal [133, 134] and atomic vapor media [135–137] are used for singularity based applications. Specially, nonlinear optical medium has been recognized as an excellent system for studying the generation, conversion and manipulation of vortex singularity because of its highly adaptable absorptive, dispersive and diffractive properties [138–141].

Recently, amplified spontaneous emission assisted parametric FWM processes in atomic medium has gain a lot of attention due to its ability to translate vortex singularities from input beam to the generated beam. Numerous experimental studies have been performed in rubidium [142–145] and cesium [146] atomic vapors for its demonstration. Atoms in diamond configuration have been established to efficiently map the wavefront dislocations of the near-infrared pump light to the generated collimated blue light (CBL) [142–144]. In these processes, two pump optical vortices with wavelengths 780 nm and 776 nm have been involved in transferring their OAM to forward-directed CBL with wavelength 420 nm [142, 147, 148]. Further, this experiment has been extended to a six

level system for demonstration of OAM transfer not only to CBL but also to the infra red radiation [143, 149]. Recently, Chopinaud *et. al.,* revisited the experiment with only one single vortex pump light operating at 776 nm [144] and mapped high helicity vortex [-30, +30] structures into the FWM signal, which is in contrast with the previous experiments. The theoretical counterpart of these experimental observations remains unexplored. A simple theory based on phase-matching condition has been adopted to explain the experimental results [142]. A detailed study of the nonlinear atomic coherence which governs such OAM conversion processes is required. Further the phase wavefront dynamics of the generated beam is very essential due to the accumulation of its constituent wave vectors in different phase in presence of diffraction and dispersion of the nonlinear atomic medium. The competition between diffraction-induced phase and dispersion-induced phase along the transverse directions of the medium define the handedness of the singularity. Hence a complete theoretical description of the Bloch equation for the atomic medium together with paraxial beam propagation equations for the generated beam needs to be formulated to demonstrate translation of OAM based on FWM processes.

In this work, we investigate how FWM process in an homogeneously broadened ^{85}Rb atomic system can facilitate the translation of OAM associated with two optical fields to the generated field. Two strong optical fields Ω_1 (780 nm) and Ω_2 (776 nm) first nonlinearly interact with the atoms as illustrated in Fig. 5.1(c). Consequently, a large fraction of population transfer from ground state to upper excited state via $|1\rangle \rightarrow |2\rangle \rightarrow |3\rangle$. The population accumulated in state $|3\rangle$ spontaneously decay into state $|4\rangle$ by emitting an infrared radiation of wavelength 5.23 μm. Simultaneously, this triggers the generation of a non-degenerate FWM signal at 420 nm along the direction of the optical fields [150, 151, 144, 152]. The frequency of the generated FWM signal (ω_g) depends on the frequency of three fields and is given by $\omega_g = \omega_1 + \omega_2 - \omega_3$. The phase mismatch parameter, $\Delta\vec{k} = (\vec{k}_1+\vec{k}_2)-(\vec{k}_g+\vec{k}_3)$ is essential to define the efficiency of the nonlinear FWM process. The appropriate selection of propagation direction of the interacting light fields can fulfils the phase matching condition ($\Delta\vec{k} = 0$). First, we introduce density matrix formalism that enables us to derive an analytical expression for the generated atomic coherence ρ_{34} and ρ_{41} in the steady state limit. Next we show how the singularity which is omnipresent in phase of the probe and control fields can be efficiently mapped to ρ_{41} in the transverse plane. This spatial inhomogeneity in absorption and phase of ρ_{41} holds the key behind translation of OAM from optical fields to FWM signal. We further solve the Maxwell's wave equation numerically at the paraxial limit in order to delineate the successful transfer of spatial inhomogeneity from atomic coherence to the generated signal.

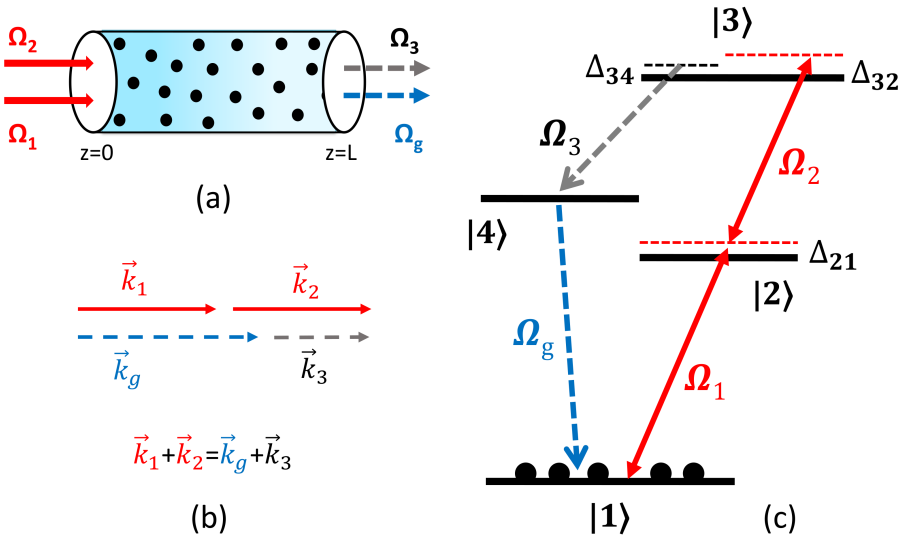

Fig. 3.1 (a) A simple illustration of the model system. Two strong input fields Ω_1 and Ω_2 interact with the Rb atoms in a vapor cell and generate two additional phase matched output signal Ω_3 and Ω_g. (b) The perfect phase matching configuration such that $\Delta\vec{k} = (\vec{k}_1 + \vec{k}_2) - (\vec{k}_3 + \vec{k}_g)$ becomes zero. (c) Schematic representation of the four-level atomic system. The energy states of ^{85}Rb are defined as $|1\rangle = 5S_{\frac{1}{2}}$, $|2\rangle = 5P_{\frac{3}{2}}$, $|3\rangle = 5D_{\frac{5}{2}}$, $|4\rangle = 6P_{\frac{3}{2}}$.

The structure of the work is as follows. In section 5.2, we introduce a four-level diamond-type atomic system and its interaction with the optical fields which is described by a semi-classical density matrix formalism. Section 5.23.2.1 presents the analytical expression of the nonlinear atomic coherence under the weak field approximation in order to describe the OAM translation process. We formulate the paraxial beam propagation equation for the generated infrared and CBL signal in section 5.23.2.2. Section 3.3 provides numerical simulations which confirm the vortex translation between different optical fields to FWM signal. Finally, we briefly conclude our work in section 5.7.

3.2 Theoretical Model

We consider the geometry as shown in Fig.5.1(a) where two co-propagating fields, namely, probe and control field interact with ^{85}Rb atoms in a four-level configuration. Fig.5.1(b) depicts that the phase matching condition ($\Delta\vec{k} = 0$) which is inevitable for efficient generation of FWM signal [153, 144]. The four-level system in Fig. 5.1(c) consists of three excited states $|2\rangle$, $|3\rangle$, $|4\rangle$ and one metastable ground state $|1\rangle$. This model can be experimentally realised by considering Zeeman sublevels with $|2\rangle = |5P_{\frac{3}{2}}, F = 4\rangle$, $|3\rangle = |5D_{\frac{5}{2}}, F = 5\rangle$, $|4\rangle = |6P_{\frac{3}{2}}, F = 4\rangle$ and $|1\rangle = |5S_{\frac{1}{2}}, F = 3\rangle$ in

^{85}Rb atomic system [153]. The atomic transitions $|2\rangle \leftrightarrow |1\rangle$ and $|3\rangle \leftrightarrow |2\rangle$ are coupled by strong probe and control fields with wavelengths $\lambda_1 = 780$ nm, $\lambda_2 = 776$ nm. The transitions $|3\rangle \leftrightarrow |4\rangle$ has a very strong dipole moment [150]. In order to model the simultaneous generation of infrared and CBL, we incorporate a weak seed field on the $|3\rangle \leftrightarrow |4\rangle$ transition with λ_3=5.23 μm [150]. All fields are defined as

$$\vec{E}_j(\vec{r},t) = \hat{e}_j \mathcal{E}_{0j}(\vec{r}_\perp) e^{i(k_j z - \omega_j t)} + c.c., \tag{3.1}$$

where $\mathcal{E}_{0j}(\vec{r}_\perp)$ is the transverse variation of envelope, $k_j = \omega_j/c$ is the propagation constant, ω_j is the frequency and $\hat{e}_j$ is the polarisation vector of the quasi-monochromatic field. The subscript, $j \in \{1,2,3\}$ represents the probe field, control field and seed field. The interaction between the atomic transitions and electromagnetic fields can be described by the following Hamiltonian under electric-dipole and rotating wave approximation

$$\begin{aligned} H =& \hbar\omega_{21} |2\rangle\langle 2| + \hbar(\omega_{21}+\omega_{32}) |3\rangle\langle 3| + \hbar(\omega_{21}+\omega_{32}-\omega_{34}) |4\rangle\langle 4| \\ & -\hbar\Omega_1 e^{-i\omega_1 t} |2\rangle\langle 1| - \hbar\Omega_2 e^{-i\omega_2 t} |3\rangle\langle 2| - \hbar\Omega_3 e^{-i\omega_3 t} |3\rangle\langle 4| + h.c., \end{aligned} \tag{3.2}$$

where the Rabi frequencies of the probe, control and seed field are defined as

$$\Omega_1 = \frac{\vec{d}_{21}.\hat{e}_1}{\hbar}\mathcal{E}_{01}, \quad \Omega_2 = \frac{\vec{d}_{32}.\hat{e}_2}{\hbar}\mathcal{E}_{02}, \quad \Omega_3 = \frac{\vec{d}_{34}.\hat{e}_3}{\hbar}\mathcal{E}_{03}. \tag{3.3}$$

The electric dipole moments $\hat{d}_{21}$, $\hat{d}_{32}$, and $\hat{d}_{34}$ allow the atomic transitions between states $|2\rangle \leftrightarrow |1\rangle$, $|3\rangle \leftrightarrow |2\rangle$ and $|3\rangle \leftrightarrow |4\rangle$ respectively. We now perform the following unitary transformation in order to remove explicit time dependency of the interaction Hamiltonian,

$$H_I = U^\dagger H U - i\hbar U^\dagger \frac{\partial U}{\partial t}, \tag{3.4}$$

where U is defined as

$$U = e^{-i(\omega_1|2\rangle\langle 2| + (\omega_1+\omega_2)|3\rangle\langle 3| + (\omega_1+\omega_2-\omega_3)|4\rangle\langle 4|)t}. \tag{3.5}$$

The Hamiltonian now turns into the following form

$$\begin{aligned} H_I =& -\hbar\Delta_{21} |2\rangle\langle 2| - \hbar(\Delta_{21}+\Delta_{32}) |3\rangle\langle 3| - \hbar(\Delta_{21}+\Delta_{32}-\Delta_{34}) |4\rangle\langle 4| \\ & -\hbar\Omega_1 |2\rangle\langle 1| - \hbar\Omega_2 |3\rangle\langle 2| - \hbar\Omega_3 |3\rangle\langle 4| + h.c., \end{aligned} \tag{3.6}$$

where the detunings are defined as

$$\Delta_{21} = \omega_1 - \omega_{21}, \Delta_{32} = \omega_2 - \omega_{32}, \Delta_{34} = \omega_3 - \omega_{34}. \tag{3.7}$$

We utilise Liouville equation to find the dynamical behaviour of the atomic populations and coherences of the diamond-type atomic system

$$\dot{\rho} = -\frac{i}{\hbar}[H_I, \rho] + \mathcal{L}_\rho, \tag{3.8}$$

where the second term incorporates spontaneous decay processes of the atomic system. The spontaneous decay rates of the excited state $|2\rangle$, $|3\rangle$ and $|4\rangle$ are denoted by γ_2, γ_3 and γ_4 respectively. In this system, the lifetime of the upper excited state $|3\rangle$ is $\tau_3 = 1/\gamma_3 = 240\ ns$ whereas the lifetime of two intermediate states $|2\rangle$ and $|4\rangle$ are given by $\tau_2 = 1/\gamma_2 = 32\ ns$ and $\tau_4 = 1/\gamma_4 = 112\ ns$ respectively [150]. Therefore, the upper state $|3\rangle$ has much slower dephasing rate than the two intermediate states $|2\rangle$ and $|4\rangle$. The collision rate (γ_c) and spontaneous decay rate (γ_1) of the metastable ground state, $|1\rangle$ are very small and can be neglected safely. We substitute Eqs. (3.6) into the Liouville's Eq. (3.8) and derive the following equations of motion for the four-level atomic system :

$$\begin{aligned}
\dot{\rho}_{11} &= \gamma_2\rho_{22} + \frac{\gamma_3}{3}\rho_{33} + \gamma_4\rho_{44} - i\Omega_1\rho_{12} + i\Omega_1^*\rho_{21},\\
\dot{\rho}_{12} &= [-i\Delta_{21} - \frac{\gamma_1+\gamma_2}{2}]\rho_{12} - i\Omega_2\rho_{13} + i\Omega_1^*(\rho_{22}-\rho_{11}),\\
\dot{\rho}_{13} &= [-i(\Delta_{21}+\Delta_{32}) - \frac{\gamma_1+\gamma_3}{2}]\rho_{13} + i\Omega_1^*\rho_{23} - i\Omega_2^*\rho_{12} - i\Omega_3^*\rho_{14},\\
\dot{\rho}_{14} &= [-i(\Delta_{21}+\Delta_{32}-\Delta_{34}) - \frac{\gamma_1+\gamma_4}{2}]\rho_{14} - i\Omega_3\rho_{13} + i\Omega_1^*\rho_{24},\\
\dot{\rho}_{22} &= -\gamma_2\rho_{22} + \frac{\gamma_3}{3}\rho_{33} + i\Omega_1\rho_{12} - i\Omega_1^*\rho_{21} + i\Omega_2^*\rho_{32} - i\Omega_2\rho_{23},\\
\dot{\rho}_{23} &= [-i\Delta_{32} - \frac{\gamma_3+\gamma_2}{2}]\rho_{23} + i\Omega_2^*(\rho_{33}-\rho_{22}) + i\Omega_1\rho_{13} - i\Omega_3^*\rho_{24},\\
\dot{\rho}_{24} &= [-i(\Delta_{32}-\Delta_{34}) - \frac{\gamma_4+\gamma_2}{2}]\rho_{24} + i\Omega_1\rho_{14} + i\Omega_2^*\rho_{34} - i\Omega_3\rho_{23},\\
\dot{\rho}_{33} &= -\gamma_3\rho_{33} + i\Omega_2\rho_{23} + i\Omega_3\rho_{43} - i\Omega_2^*\rho_{32} - i\Omega_3^*\rho_{34},\\
\dot{\rho}_{34} &= [i\Delta_{34} - \frac{\gamma_4+\gamma_3}{2}]\rho_{34} + i\Omega_3(\rho_{44}-\rho_{33}) + i\Omega_2\rho_{24},\\
\dot{\rho}_{44} &= -\gamma_4\rho_{44} + \frac{\gamma_3}{3}\rho_{33} - i\Omega_3\rho_{43} + i\Omega_3^*\rho_{34},
\end{aligned} \tag{3.9}$$

where the overdot stands for the time derivative and star ($*$) denotes the complex conjugate. The diagonal density matrix elements, ρ_{ii}, ($i \in 1, 2, 3, 4$) satisfy the conservation of population *i.e.*, ρ_{11}+ρ_{22}+ρ_{33}+ρ_{44}=1.

3.2.1 Perturbative analysis

In this section, we derive an analytical expression for the atomic coherence under $\Omega_3 \ll \Omega_1, \Omega_2$ that asserts the seed field (Ω_3) to be treated as a perturbation to the

system [150]. This analysis is valid for all orders for the probe and control fields. Now the time independent solutions of the density-matrix equations can be expressed as

$$\rho_{ij} = \rho_{ij}^{(0)} + \Omega_3 \rho_{ij}^{(1)} + \Omega_3^* \rho_{ij}^{(2)} \tag{3.10}$$

where $\rho_{ij}^{(0)}$ is the solution in the absence of the seed field and $\rho_{ij}^{(k)}$, $k \in \{1, 2\}$ describes the solution at positive and negative frequencies of the seed field, respectively. We now substitute Eq. (3.10) in Eqs. (3.9) by considering time derivative to be zero. We obtain two sets of ten coupled linear equations by equating the coefficients of Ω_3 and Ω_3^*. Next, we solve these algebraic equations to derive the atomic coherences ρ_{34} and ρ_{41}. The steady-state value of these atomic coherence ρ_{34} and ρ_{41} can be expressed by the following expression

$$\rho_{34} = \frac{i|\Omega_1|^2|\Omega_2|^2\Omega_3(\Gamma_{14}+\Gamma_{23})}{\Gamma_{12}\Gamma_{23}\digamma_1\Gamma_{14}\Gamma_{34}\digamma_2}; \tag{3.11}$$

$$\begin{aligned}
\digamma_1 &= \Gamma_{13} + \frac{|\Omega_2|^2}{\Gamma_{12}} + \frac{|\Omega_1|^2}{\Gamma_{23}}, \\
\digamma_2 &= \Gamma_{24} + \frac{|\Omega_2|^2}{\Gamma_{34}} + \frac{|\Omega_1|^2}{\Gamma_{14}},
\end{aligned}$$

$$\rho_{41} = \frac{i\Omega_1\Omega_2\Omega_3^*\digamma_3}{\Gamma_{41}\Gamma_{21}\digamma_4\digamma_5}; \tag{3.12}$$

$$\begin{aligned}
\digamma_3 &= \left[\Gamma_{42} + \frac{|\Omega_2|^2}{\Gamma_{43}} - \frac{|\Omega_1|^2}{\Gamma_{32}}\right], \\
\digamma_4 &= \left[\Gamma_{42} + \frac{|\Omega_2|^2}{\Gamma_{43}} + \frac{|\Omega_1|^2}{\Gamma_{41}}\right], \\
\digamma_5 &= \left[\Gamma_{31} + \frac{|\Omega_2|^2}{\Gamma_{21}} + \frac{|\Omega_1|^2}{\Gamma_{32}}\right],
\end{aligned}$$

where

$$\begin{aligned}
\Gamma_{21} &= i\Delta_{21} - \frac{\gamma_2+\gamma_1}{2}, \quad \Gamma_{31} = i(\Delta_{21}+\Delta_{32}) - \frac{\gamma_3+\gamma_1}{2}, \\
\Gamma_{32} &= i\Delta_{32} - \frac{\gamma_3+\gamma_2}{2}, \quad \Gamma_{41} = i(\Delta_{21}+\Delta_{32}-\Delta_{34}) - \frac{\gamma_4+\gamma_1}{2}, \\
\Gamma_{42} &= i(\Delta_{32}-\Delta_{34}) - \frac{\gamma_4+\gamma_2}{2}, \quad \Gamma_{43} = -i\Delta_{34} - \frac{\gamma_4+\gamma_3}{2}.
\end{aligned} \tag{3.13}$$

The expression of remaining Γ_{ij} terms can be obtained from the complex conjugate relation *i.e.* $\Gamma_{ij} = \Gamma_{ji}^*$. The numerator of Eq. (3.11) and Eq. (3.12) clearly shows that

the structure of the generated atomic coherence can be modulated along the azimuthal plane by selecting appropriate phase and intensity profiles of probe and control fields.

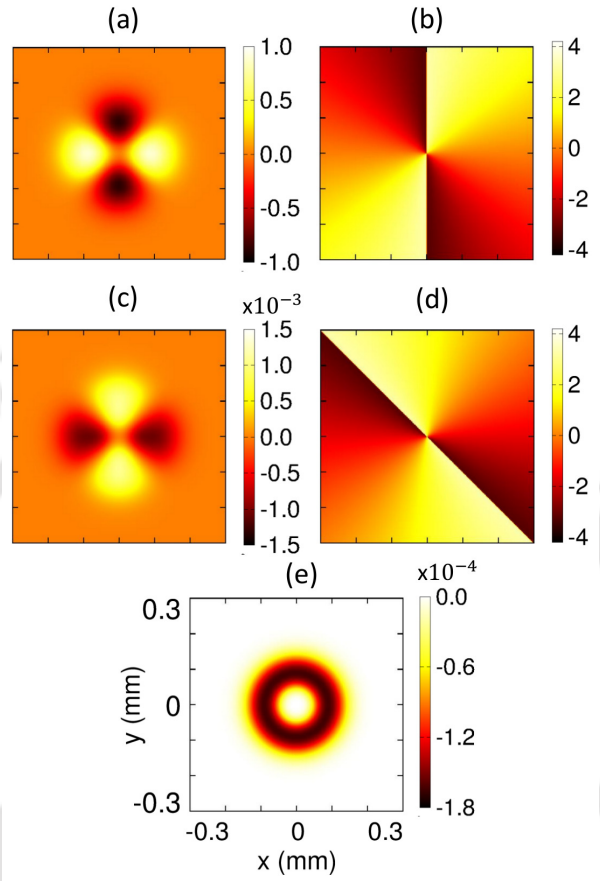

Fig. 3.2 (a) Amplitude (Re[Ω_1]) and (b) phase structure of Laguerre-Gaussian probe beam. (c) Absorption (Im[ρ_{41}]) and (d) phase profile of the atomic coherence, ρ_{41} in the transverse plane when Ω_1 possesses the optical vortex. (e) Simultaneous absorption profile (Im[ρ_{34}]) corresponding to atomic coherence ρ_{34}. The parameters are $m_1 = 0$, $l_1 = 2$, $w_1 = 90\ \mu m$, $\Omega_1^0 = 1.2\gamma$, $\Omega_2^0 = 1.2\gamma$, $\Omega_3^0 = 0.005\gamma$, $\Delta_{21} = 0$, $\Delta_{32} = 0$, $\Delta_{34} = 0$.

3.2.2 Beam propagation equation

The study of Maxwell's wave equations is essential to demonstrate how the generated atomic coherence ρ_{34} and ρ_{41} can produce an infrared light beam and CBL with desired OAM. The wave equation for the generated infrared and CBL light beam can be written as

$$\left(\nabla^2 - \frac{1}{c^2}\frac{\partial^2}{\partial t^2}\right)\vec{E} = \frac{4\pi}{c^2}\frac{\partial^2 \vec{\mathcal{P}}}{\partial t^2}, \tag{3.14}$$

where $\vec{E} = \vec{E}_3 + \vec{E}_g$ is the electric field of the generated signals and $\vec{\mathcal{P}}$ is the induced polarisation due to the probe and control fields. The induced macroscopic polarizations

can be expressed in terms of the atomic coherence as

$$\vec{\mathcal{P}} = \mathcal{N}\left(\vec{d}_{43}\rho_{34}e^{-i\omega_3 t} + \vec{d}_{14}\rho_{41}e^{-i\omega_g t} + c.c.\right) \tag{3.15}$$

Under slowly varying envelope and paraxial wave approximation, the wave Eq. (3.14) can be cast into the following form

$$\frac{\partial\Omega_3}{\partial z} = \frac{i}{2k_3}\nabla_\perp^2\Omega_3 + i\eta_3\rho_{34}, \tag{3.16}$$

$$\frac{\partial\Omega_g}{\partial z} = \frac{i}{2k_g}\nabla_\perp^2\Omega_g + i\eta_g\rho_{41}. \tag{3.17}$$

The first order derivative with respect to z on the left hand side indicates the amplitude variation of the generated signal envelope Ω_3 and Ω_g along the length of the medium. The first term on the right hand side represents the beam's phase induced diffraction and the rotation of the wave front during its propagation. The last term on the right-hand side accounts for the generation and dispersion of the medium. The coupling constant, η_j is defined as $\eta_j = 3\mathcal{N}\gamma_j\lambda_j^2/8\pi$ where $j \in \{3, g\}$. The atomic density $\mathcal{N}$ is 1.5×10^9 atoms/cm^3 and wavelength of the infrared and CBL is 5.23 μm and 420 nm respectively. We use appropriate spatially dependent transverse profile of the optical fields to generate the FWM signal. For this purpose, the transverse spatial profile of the optical beams are taken to be of Laguerre-Gaussian mode (m) with topological charge l that can be expressed as

$$\begin{aligned}\Omega_j(r,\phi,z) = \Omega_j^0\frac{w_j}{w_j(z)}\left(\frac{r\sqrt{2}}{w_j(z)}\right)^{|l|} e^{-\frac{r^2}{w_j^2(z)}} L_m^l\left[\frac{2r^2}{w_j^2(z)}\right] \\ \times e^{il\phi}e^{\frac{ik_j r^2}{2R(z)}}e^{-i(2m+|l|+1)\tan^{-1}\left(\frac{z}{z_0}\right)}, \\ r = \sqrt{x^2+y^2}, \quad \phi = \tan^{-1}\left(\frac{y}{x}\right), \\ \psi(m,l,z) = (2m+|l|+1)\tan^{-1}(z/z_0).\end{aligned} \tag{3.18}$$

where Ω_j^0 is the input amplitude, $R(z) = z + z_0^2/z$ is the radius of curvature and $z_0 = \pi w_j^2/\lambda_j$ is the Rayleigh length of the beam. The spot size of the beam is defined as $w_j(z) = w_j\sqrt{1+(z/z_0)^2}$, where w_j is the minimum beam waist at z=0. The subscript, $j \in \{1, 2\}$ refers to the probe and control fields.

3.3 Vortex beam generation

The aim of this section is to provide a detail theoretical explanation behind vortex beam generation. First we show how input singular beams generate spatial inhomogeneity in

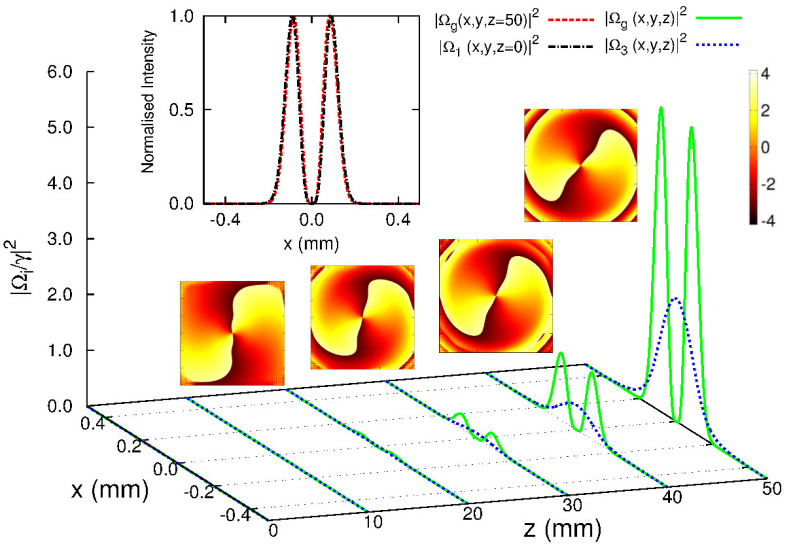

Fig. 3.3 The solid green curve ($i = g$) depicts the evolution of the FWM based CBL signal (Ω_g) at different propagation lengths along with its phase structure. The dotted blue curve ($i = 3$) represents the evolution of infrared signal (Ω_3). We multiply 10^1 and 10^4 with the infrared field intensity ($|\Omega_3/\gamma|^2$) and FWM signal intensity ($|\Omega_g/\gamma|^2$) respectively. Inset figure compares the normalised intensity profile of the output Ω_g and input Ω_1. The parameters are $m_1 = 0$, $l_1 = 2$, $w_1 = 90\ \mu m$, $\Omega_1^0 = 1.2\gamma$, $\Omega_2^0 = 1.2\gamma$, $\Omega_3^0 = 0.005\gamma$, $\Delta_{21} = 0$, $\Delta_{32} = 0$, $\Delta_{34} = 0$.

absorption and singularity in phase of ρ_{41} that hold the key behind translation of OAM from input optical fields to FWM signal. In order to satisfy the perturbation condition, we chose the probe field ($\Omega_1 = 1.2\gamma$) and control field ($\Omega_2 = 1.2\gamma$) intensities to be much larger than seed field ($\Omega_3 = 0.005\gamma$) intensity. We have chosen the probe field to be a singular beam while keeping the rest of the two fields as spatially homogeneous. The spatially inhomogeneous transverse profile of LG beam as shown in Fig. 3.2(a) give rise to inhomogeneous character of absorption ($\mathrm{Im}[\rho_{41}]$). However the bright and dark regions of the coherence get interchanged as compared to the spatial inhomogeneity of LG beam. This formation can be explained from Eq. (3.12), where $\mathrm{Im}[\rho_{41}] \propto -i\Omega_1$ at resonance condition *i.e.* $\Delta_{21} = 0$, $\Delta_{32} = 0$, $\Delta_{34} = 0$. Fig. 3.2(b) shows the phase singularities of the LG beam which are located at $\phi = 0$ and $\phi = 2\pi$, and are mapped to the phase structure of induced coherence ρ_{41} as depicted in Fig. 3.2(d). We observed an anti-clockwise rotation of $\pi/2$ developed in the induced phase singularity that comes from the $e^{-i\pi/2}$ factor that appear in the numerator of the Eq. (3.12). Hence the characteristic features of absorption and phase of the induced coherence are the essence of singular beam generation. In Fig. 3.2(e), we illustrate the absorption profile ($\mathrm{Im}[\rho_{34}]$) corresponding to the atomic coherence ρ_{34}. Note that the inhomogeneous transverse profile of Ω_1 as shown in Fig. 3.2(a) does not appear in the absorption

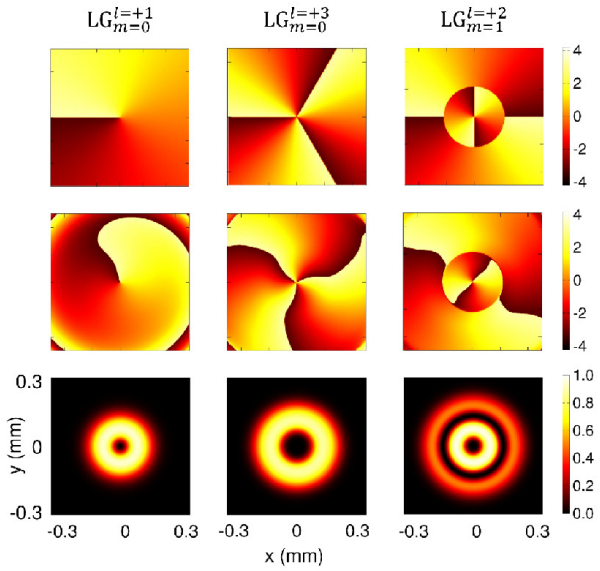

Fig. 3.4 Transfer of different OAM from probe beam (Ω_1) to FWM signal (Ω_g). First row shows phase profile of Ω_1 due to different OAM at z=0. Second and third row depict the phase and intensity profile of Ω_g at $z = 50\ mm$. Other parameters are same as shown in Fig. 3.3.

profile of ρ_{34}. This implies that the vortex informations of Ω_1 can not be translated into the generated infrared field in the considered model system.

Next, we derive the conditions for successfully mapping spatial structure of phase as well as intensity profile of the light beams to the generated FWM signal. The faithful generation of signal is possible by satisfying the phase matching conditions and fulfilment of OAM conservation laws as well as the Gouy phase matching criterion. A collinear beam geometry, where the proper choice of propagation direction of the interacting fields can secure the phase-matching condition, *i.e.*, $\vec{k}_g+\vec{k}_3 = \vec{k}_1+\vec{k}_2$, is used in our study. The coherent FWM process [144] inherently executes OAM conservation law *i.e.*, $l_g + l_3 = l_1 + l_2$. The Gouy phase matching criterion is another important requirement which immensely controls the nonlinear frequency conversion process [144]. The Gouy phase appears in the OAM carrying light beams as $\psi(m, l, z) = (2m + |l| + 1)\tan^{-1}(z/z_0)$. The efficient conversion confirms that the Gouy phase of the applied vortex beams should be equal to the generated FWM signal at any propagation distance z. We first choose all the fields in resonance with their respective atomic transitions. With all these stringent conditions, the individual OAM of probe beam (l_1) as well as control beam (l_2) or a combination of l_1, l_2 can be cloned from optical beams into the generated CBL signal.

We numerically solve Eq. (3.16) and Eq. (3.17) using the split-step Fourier method (SSFM) for the progression of the infrared and FWM signal to confirm successful

mapping of the induced coherence ρ_{34} and ρ_{41} into the respective signal envelope. The nonlinear atomic coherence ρ_{41} in Eq. (3.17) governs that various OAM conversion processes. Both the intensity and phase profile of the FWM signal can be pondered for confirmation of its actual vortex mode. The spatial dynamics of the probe and control beams can be neglected as it does not affect the progression of the FWM signal.

3.3.1 Transfer OAM of Ω_1

We now exhibit our results by considering different transverse shape of the probe beam (Ω_1) by selecting various values of l_1 and m_1 of the Laguerre-Gaussian mode. The control field Ω_2 is chosen to be continuous wave (cw) as it gives a plane wave front. In the first step, we focus on the generation of FWM based CBL which gets cloned from the vortex probe beam with mode $m_1 = 0$ and $l_1 = +2$. In Fig. 3.3, the solid green curve depicts the transverse variation of the generated CBL intensity $|\Omega_g/\gamma|^2$ at different propagation lengths of the medium together with azimuthal phase. Simultaneously, the dotted blue curve in Fig. 3.3 shows the transverse variation of the generated infrared intensity $|\Omega_3/\gamma|^2$ along the propagation lengths. These results are obtained from the beam propagation equations [Eq. (3.16) and Eq. (3.17)] along with the analytical perturbative expression of atomic coherences ρ_{34} and ρ_{41} derived from the full set of the density-matrix equations [Eq. (3.9)] at steady state limit. Note that in Fig. 3.3, the generation of infrared field (dotted blue curve) triggers the generation of CBL signal (solid green curve) [150]. Also, the intensity of the generated infrared field further enhances the intensity of the CBL signal inside the atomic medium as shown in Eq. (3.12) as well as in Fig. 3.3. However, the overall output intensity of the infrared and CBL signal can be controlled by the atomic density and the intensity of input probe and control field. The inset plot of Fig. 3.3 confirms that the generated CBL signal at $z = 50\ mm$ acquires identical intensity profile of the input probe beam as indicated by Eq. (3.12) [143]. We also notice that the spreading of generated beam due to diffraction is not very significant since its Rayleigh length, $z_g = \pi w_g^2/\lambda$ is larger than the propagation distance z. As seen from Fig. 3.3, the generated CBL phase experiences a rotation in the transverse plane as it propagates along z-direction which is an inherent feature of a vortex beam [121]. The phase structure of the FWM signal carries two distinct singularities at 0 and 2π location. A phase change of 4π establishes the fact that the FWM assisted optical vortex has same features as the input probe vortex. Next, a representative set of input probe vortex mode *e.g.*, $m_1 = 0, l_1 = 1$; $m_1 = 0, l_1 = 3$ and $m_1 = 1, l_1 = 2$; is taken into consideration for our analysis in order to justify the robustness of the proposed system. In Fig. 5.4, the first row represents the phase structure of the input probe beam carrying different OAM. Whereas the

second and third row of Fig. 5.4 depict the corresponding phase and intensity profile of the generated CBL at a propagation distance of $z = 50\ mm$. It is evident from Fig. 5.4 that the OAM of the probe beam precisely transfer into the generated CBL signal. We observe slight distortion in the phase structure of CBL signal. The origin of this distortion is the non-linearity induced in the medium by the strong probe and control field. This phase distortion can be removed completely by selecting suitably lower values of probe and control field intensity.

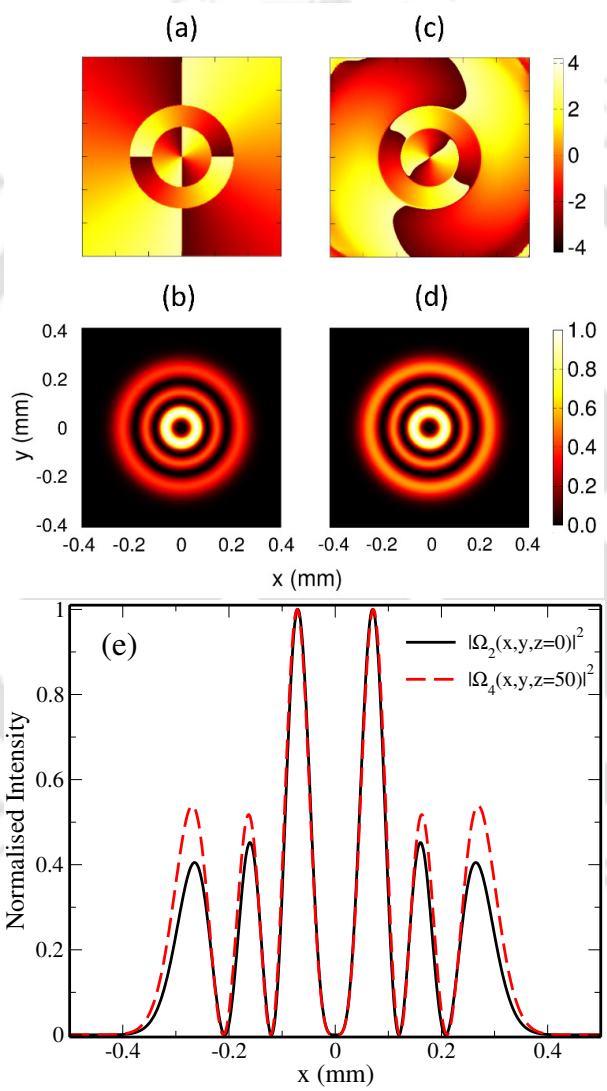

Fig. 3.5 Transfer of control beam's OAM (l_2) is demonstrated. Input phase and intensity profile of the control beam [(a) and (b)]. Output phase and intensity profile of the FWM signal [(c) and (d)]. (e) Comparison of normalised intensity profile of input control beam and output FWM signal. The parameters are $m_2 = 2$, $l_2 = 2$, $w_2 = 90\ \mu m$. Other parameters are same as shown in Fig. 3.3.

3.3.2 Transfer OAM of Ω_2

We now investigate transfer of OAM from control beam (Ω_2) to FWM signal. For this purpose, transverse profile of the control field is taken to be a higher-order Laguerre-Gaussian mode with m_2=2, l_2=2, whereas the probe field Ω_1 is chosen as cw for plane wave-front. Fig. 3.5(a) and 3.5(b) delineate the phase structure and intensity profile of the input control beam. The output phase and intensity profile of the CBL signal at $z = 50\ mm$ mm are shown in Fig. 3.5(c) and 3.5(d). In order to check the fidelity of the conversion, we compare the normalised intensity profile of Ω_2 at z=0 and Ω_g at $z = 50\ mm$ mm in Fig. 3.5(e). This study confirms that the FWM signal and control beam have similar intensity profile and phase structure. Note that the transfer of OAM induced information from the control beam into the FWM signal is achieved only because $\rho_{41} \propto \Omega_2$ as suggested by Eq. (3.12). We have also examined the intensity profile and phase structure of the generated infrared field. We found that the phase informations imprinted on the control beam can not be profoundly mapped into the generated infrared signal simply because $\rho_{34} \propto |\Omega_2|^2$ as shown in Eq. (3.11).

3.3.3 Transfer OAM of Ω_1 and Ω_2

In this section, we explore simultaneous transfer of probe and control beam's OAM into the generated FWM signal. We consider both the optical beams (Ω_1 and Ω_2) possess the Laguerre-Gaussian mode, $m_j = 0, l_j = 2;\ j \in \{1, 2\}$. From vortex beam generation criterion, we have found that OAM induced phase structure of the output FWM signal is the sum of individual probe and control beam's OAM *i.e.*, $l_g = l_1 + l_2$. Fig. 3.6(a) and 3.6(b) represent the phase structure and intensity profile of the input probe and control beam respectively. The phase and intensity profile of the generated CBL signal at $z = 50\ mm$ are depicted in Fig. 3.6(c) and 3.6(d). These results support that the FWM signal gets its shape from its generator beams and it obeys $\rho_{41} \propto \Omega_1\Omega_2$. Subsequently higher OAM can be generated by using the sum rule of probe and control OAM, $l_1 + l_2$, which is efficiently transferred into the FWM signal as it is clearly depicted in Fig. 3.6(d). It should be borne in mind that nonlinear atomic coherence ρ_{34} in Eq. (3.11) is proportional to $|\Omega_1|^2|\Omega_2|^2$. Under this condition, the infrared field is generated as a non-singular light beam. Therefore, the atomic coherence plays the key roles in the transfer of the OAM of probe and control beam simultaneously on the generated light beam.

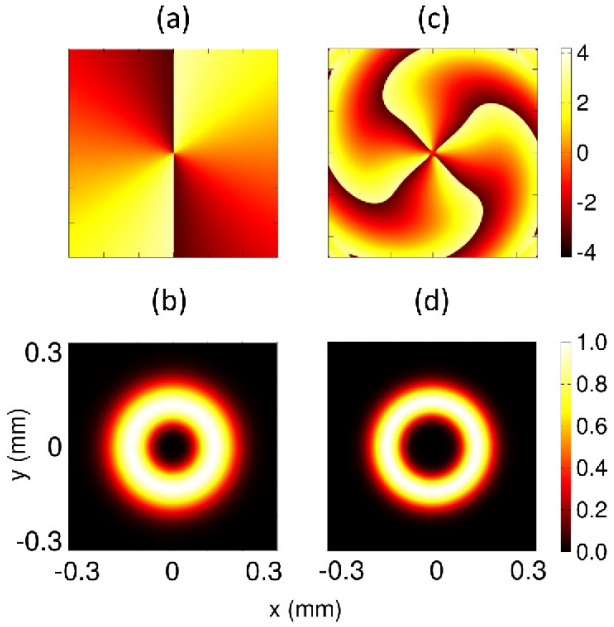

Fig. 3.6 Simultaneous transfer of probe OAM ($l_1 = 2$) and control OAM ($l_2 = 2$) into the FWM signal such that $l_g = l_1 + l_2$. The phase structure and normalised intensity profile of the input probe and control beam [(a) and (b)]. Output phase structure and intensity profile of the FWM signal [(c) and (d)]. The parameters are $m_1 = 0$, $m_2 = 0$, $l_1 = 2$, $l_2 = 2$, $w_1 = 90\ \mu m$, $w_2 = 90\ \mu m$. Other parameters are same as shown in Fig. 3.3.

3.4 Conclusion

In conclusion, we have demonstrated an efficient FWM based OAM translation process in a diamond-type homogeneously broadened ^{85}Rb atomic system. Two optical fields nonlinearly interact with the atoms and initiate phase-matched infrared and non-degenerate FWM signal [152]. In this nonlinear process, the vortex modes imprinted on the probe or control beam are transferred into the generated FWM signal with high fidelity. The generation and manipulation of such optical vortices through nonlinear FWM processes in atomic system can have promising applications in optical communication and quantum information processing systems.

Chapter 4

Microwave assisted transparency in a M-system

4.1 Introduction

Recently there are efforts towards atom based microwave (MW) electro- and magnetometry due to their high reproducibility, accuracy, spatial resolution and stability [154–158]. This is based upon the phenomenon of electromagnetically induced transparency (EIT) [2, 3] in which the absorption property of a probe laser is altered in the presence of control lasers in a multilevel system. The basis of EIT is the induced or transfer of coherence (TOC) between the levels which are not directly driven by optical control fields. The EIT has been explored extensively in the three level Λ [159–161, 19, 162, 21, 22], V [163–165] and Ξ [23, 166, 34, 25, 167, 24, 168] systems. It has also been investigated beyond three level systems such as in doubly driven V [169], N [20, 170–173], Y [174], inverted Y [175], $\Xi\Lambda$ [176, 177], tripod [178, 179] and doubled tripod [180] systems. The role of various TOCs for a general N-level atomic system has been well studied [181]. This phenomenon has been paid a great deal of attention due to its potential applications in a wide variety of fields like controlling the group velocity of light [19, 20], coherent storage and retrieval of light [21, 22], high-resolution spectroscopy [23, 24], studying photon-photon interaction via Rydberg blockade [166, 34], photon transistor for quantum optical information processing [25, 182, 168], etc.

The induced coherence of a Λ system can be drastically modified by applying a low frequency field which couples two ground levels. Two optical fields along with a lower level coupling field (LL) form a closed loop three level Λ system. The relative amplitude, detuning and phase differences between the LL field and two optical fields can play an

important role in significantly manipulating the optical property of the system such as dispersion, absorption and nonlinearity [45, 183, 184, 47, 46, 185, 30, 186].

In the above mentioned closed loop Λ system, population transfer is unavoidable in the presence of high power MW field as it acts on one of the populated states. The MW induced population transfer between metastable states leads to imperfect transparency which limits many of the EIT based applications [187]. Here we study an M-system wherein two unoccupied ground states are coupled with a MW field and hence there is no population transfer with this MW Rabi frequency. This MW field also enhances the generated atomic coherence at the probe transition manifold which can not be found in generic three level systems. This enhancement of atomic coherence is a result of the interference between excitation pathways from the different atomic states.

The chapter is organized as follows : in the next section, we introduce the physical model and basic equations of motion for a M-system by using a semiclassical theory. In section 4.2.2, an approximate analytical expression for linear susceptibility of a weak probe field is derived using the perturbative approach under three photon resonance condition. After deriving the analytical form of the atomic coherences, we compare it with the full numerical solution. In section 4.3, we first explain the lineshape of the probe laser absorption as a function of probe detuning for various MW strengths and phases. Finally M-systems are compared to closed loop Λ-systems both having ground states coupled by MW field.

4.2 Theoretical formulation

4.2.1 Model Configuration

We consider a five level atomic M-system as shown in Fig. 4.1a. The electric field associated with the lasers driving the transition $|i\rangle \rightarrow |i+1\rangle$ is $\mathrm{E}_{i,i+1}e^{i(\omega^L_{i,i+1}t+\phi^L_{i,i+1})}$. The $\mathrm{E}_{i,i+1}$ is amplitude, $\omega_{i,i+1}$ is the frequency and $\phi^L_{i,i+1}$ is the phase. We define Rabi frequency $\Omega_{i,j} = d_{i,j}E_{i,j}e^{i\phi^L_{i,j}}/\hbar$ for the transition $|i\rangle \rightarrow |j\rangle$ having the dipole moment matrix element $d_{i,j}$ driven by a laser with electric field amplitude $\mathrm{E}_{i,j}$ and the phase $\phi^L_{i,j}$. The Ω_{12} is the Rabi frequency of the probe laser driving $|1\rangle \rightarrow |2\rangle$ and shown with solid blue arrow in Fig. 4.1. The Rabi frequencies of the control lasers driving the transitions $|2\rangle \rightarrow |3\rangle$, $|3\rangle \rightarrow |4\rangle$ and $|4\rangle \rightarrow |5\rangle$ are denoted by Ω_{23}, Ω_{34} and Ω_{45} respectively and shown with solid red arrows. The lower level states $|3\rangle$ and $|5\rangle$ is coupled by a MW field with Rabi frequency Ω^{MW}_{35} as shown with solid green arrow. The M-system can be realized in ^{87}Rb at the D_1 line using the two hyperfine levels $F_g = 1$ and $F_g = 2$ of the ground state $5\mathrm{S}_{1/2}$ and the hyperfine level $F_e = 1$ of excited state $5\mathrm{P}_{1/2}$ as shown in Fig. 4.1b. The decay rate of the excited state $5\mathrm{P}_{1/2}$ is

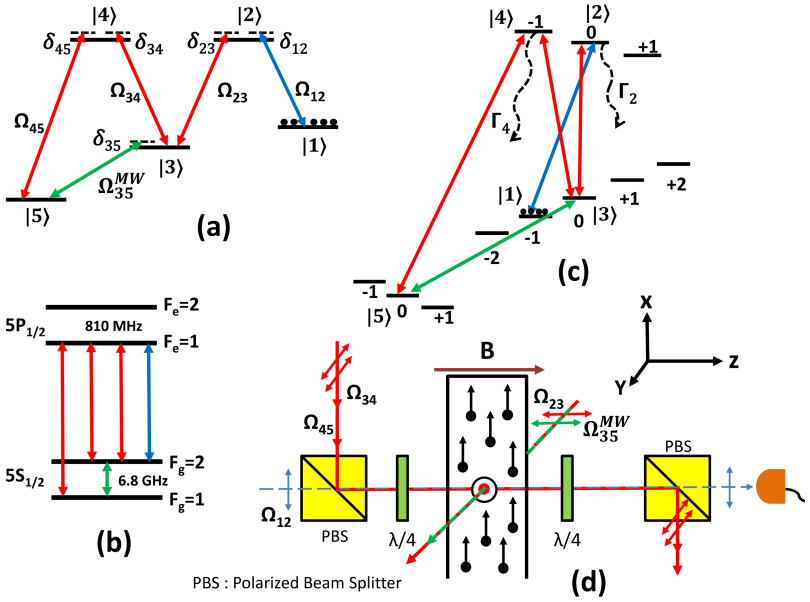

Fig. 4.1 (Color online). (a) The general energy level diagram for M-system. (b) The relevent energy level of ^{87}Rb for D_1 line to realize the M-system. (c) The magnetic sublevels in the presence of the magnetic field of the hyperfine states to realize the M-system. (d) Schematic of the experimental set-up for Doppler free configuration for all the optical and the MW fields .

$2\pi\times6$ MHz. We apply a large magnetic field to split the magnetic sublevels to keep away the unwanted sublevels from resonance and to define the quantization axis. The sign and value of the Lande g factor for the chosen hyperfine is suitable to split and keep away the unwanted transitions. At 200 G applied magnetic field the splitting of the magnetic sublevels for $F_e = 1$ is $2\pi\times46$ MHz and splitting for $F_g = 2$ and $F_g = 1$ is $2\pi\times140$ MHz as shown in Fig. 4.1c. We consider the probe to be σ^+ polarized and driving the transition $|F_g = 2; m_F = -1\rangle \rightarrow |F_e = 1; m_F = 0\rangle$. The π polarized control laser is driving the $|F_g = 2; m_F = 0\rangle \rightarrow |F_e = 1; m_F = 0\rangle$ transition. The two σ^- polarized control lasers are driving the $|F_g = 2; m_F = 0\rangle \rightarrow |F_e = 1; m_F = -1\rangle$ and $|F_g = 1; m_F = 0\rangle \rightarrow |F_e = 1; m_F = -1\rangle$ transitions as shown in Fig. 4.1c.

In the absence of the control lasers all the magnetic sublevels of the hyperfine states $F_g = 1$ and $F_g = 2$ will be equally populated. However when the control lasers are applied, the population in the ground states connected with the control lasers will deplete. In the steady state there will be no population left in the $|F_g = 1, m_F = 0\rangle$ and $|F_g = 2, m_F = 0\rangle$ states as shown in Fig. 4.1c.

The experimental set-up is shown in Fig. 4.1d. In this all the optical and MW fields are propagating perpendicular to the atomic beam and hence does not involve any Doppler shift and broadening. The probe laser (Ω_{12}) and the two control lasers, (Ω_{34} and Ω_{45}) are mixed by a polarizing beam splitter, PBS and are propagating along the

z-direction. The polarization of the probe laser is σ^+ and it is σ^- for the two control lasers, Ω_{34} and Ω_{45} w.r.t the applied magnetic field of 200 G along the z-direction as shown in the Fig. 4.1d. The opposite circular polarization for control and the probe lasers are set by a $\lambda/4$ waveplate just before entering the glass cell. After coming out of the glass cell the probe laser is separated from the two control lasers using a $\lambda/4$ waveplate and a PBS. The π-polarized control laser (Ω_{23}) and the MW field (Ω_{35}^{MW}) are propagating along y-direction having the polarization along the z-direction. Instead of Rb atomic beam we can also use the cold atoms or nano-cell to avoid Doppler broadening[188, 189].

The unperturbed atomic Hamiltonian can be written as

$$H_0 = \sum_{j=1}^{5} \hbar\omega_j \left|j\right\rangle \left\langle j\right|, \tag{4.1}$$

where $\hbar\omega_j$ is the energy of the $|j\rangle$ state. Under the action of five coherent fields, the interaction Hamiltonian of the system in the dipole approximation is given by

$$\begin{aligned} H_I = &\frac{\hbar\Omega_{12}}{2}[e^{i\omega_{12}^L t} + e^{-i\omega_{12}^L t}] \left|1\right\rangle \left\langle 2\right| + \frac{\hbar\Omega_{23}}{2}[e^{i\omega_{23}^L t} + e^{-i\omega_{23}^L t}] \left|2\right\rangle \left\langle 3\right| \\ &+ \frac{\hbar\Omega_{34}}{2}[e^{i\omega_{34}^L t} + e^{-i\omega_{34}^L t}] \left|3\right\rangle \left\langle 4\right| + \frac{\hbar\Omega_{45}}{2}[e^{i\omega_{45}^L t} + e^{-i\omega_{45}^L t}] \left|4\right\rangle \left\langle 5\right| \\ &+ \frac{\hbar\Omega_{35}^{MW}}{2}[e^{i\omega_{35}^{MW} t} + e^{-i\omega_{35}^{MW} t}] \left|3\right\rangle \left\langle 5\right| \end{aligned} \tag{4.2}$$

Hence the total Hamiltonian will be $H = H_0 + H_I$. We use suitable unitary transformation to eliminate the explicit time dependent part in the Hamiltonian. In rotating wave approximation, the effective interaction Hamiltonian can be expressed as

$$\begin{aligned} \mathcal{H}_I = \hbar[&0 \left|1\right\rangle \left\langle 1\right| - \delta_{12} \left|2\right\rangle \left\langle 2\right| - (\delta_{12} - \delta_{23}) \left|3\right\rangle \left\langle 3\right| - (\delta_{12} - \delta_{23} + \delta_{34}) \left|4\right\rangle \left\langle 4\right| \\ &- (\delta_{12} - \delta_{23} + \delta_{34} - \delta_{45}) \left|5\right\rangle \left\langle 5\right| + \frac{\Omega_{12}}{2} \left|1\right\rangle \left\langle 2\right| + \frac{\Omega_{23}}{2} \left|2\right\rangle \left\langle 3\right| + \frac{\Omega_{34}}{2} \left|3\right\rangle \left\langle 4\right| \\ &+ \frac{\Omega_{45}}{2} \left|4\right\rangle \left\langle 5\right| + \frac{\Omega_{35}^{MW}}{2} e^{i(-\delta_{34}+\delta_{45}+\delta_{35}^{MW})t} \left|3\right\rangle \left\langle 5\right|] + c.c., \end{aligned} \tag{4.3}$$

where $\delta_{12} = \omega_{12}^L - (\omega_2 - \omega_1)$, $\delta_{23} = \omega_{23}^L - (\omega_2 - \omega_3)$, $\delta_{34} = \omega_{34}^L - (\omega_4 - \omega_3)$, $\delta_{45} = \omega_{45}^L - (\omega_4 - \omega_5)$ and $\delta_{35}^{MW} = \omega_{35}^{MW} - (\omega_5 - \omega_3)$ known as detunings of the lasers for respective transitions. Now we impose the condition $\delta_{45} + \delta_{35}^{MW} - \delta_{34} = 0$, so that the time dependence is completely eliminated from the effective interaction Hamiltonian. To explore the dynamics of the atomic system, we use the density matrix equations where radiative relaxation of the atomic states are included. The atomic density

operator ρ obey the following equations

$$\dot{\rho} = -\frac{i}{\hbar}[\mathcal{H}_I, \rho] - \frac{1}{2}\{\Gamma, \rho\} \tag{4.4}$$

where Γ is the relaxation matrix [53].

4.2.2 Perturbative Analysis

To study the response of the medium, we numerically solve the density matrix equations at steady-state condition. We derive an analytical expression for the probe field response that is correct to first order in probe field approximation and exact for the all order in control fields. In this weak approximation, there will be no population transfer and hence the evolution of the population i.e. diagonal terms of the density matrix such as ρ_{11}, ρ_{22}, ρ_{33}, ρ_{44} and ρ_{55} can be ignored with $\rho_{11} \approx 1$, $\rho_{22} \approx 0$, $\rho_{33} \approx 0$, $\rho_{44} \approx 0$ and $\rho_{55} \approx 0$. Time evolution for the coherences i.e. off-diagonal terms of the density matrix will be given by following set of equations

$$\begin{aligned}
\dot{\rho}_{12} &\approx -\gamma_{12}\rho_{12} + \frac{i}{2}\Omega_{12} + \frac{i}{2}\Omega_{23}^{*}\rho_{13}, \\
\dot{\rho}_{13} &\approx -\gamma_{13}\rho_{13} - \frac{i}{2}\Omega_{12}\rho_{23} + \frac{i}{2}\Omega_{23}\rho_{12} + \frac{i}{2}\Omega_{34}^{*}\rho_{14} + \frac{i}{2}\Omega_{35}^{MW*}\rho_{15}, \\
\dot{\rho}_{14} &\approx -\gamma_{14}\rho_{14} - \frac{i}{2}\Omega_{12}\rho_{24} + \frac{i}{2}\Omega_{34}\rho_{13} + \frac{i}{2}\Omega_{45}^{*}\rho_{15}, \\
\dot{\rho}_{15} &\approx -\gamma_{15}\rho_{15} - \frac{i}{2}\Omega_{12}\rho_{25} + \frac{i}{2}\Omega_{35}^{MW}\rho_{13} + \frac{i}{2}\Omega_{45}\rho_{14},
\end{aligned} \tag{4.5}$$

where

$$\begin{aligned}
\gamma_{12} &= \left[\frac{\Gamma_1 + \Gamma_2}{2} + i\delta_{12}\right], \\
\gamma_{13} &= \left[\frac{\Gamma_1 + \Gamma_3}{2} + i\left(\delta_{12} - \delta_{23}\right)\right], \\
\gamma_{14} &= \left[\frac{\Gamma_1 + \Gamma_4}{2} + i\left(\delta_{12} - \delta_{23} + \delta_{34}\right)\right], \\
\gamma_{15} &= \left[\frac{\Gamma_1 + \Gamma_5}{2} + i\left(\delta_{12} - \delta_{23} + \delta_{34} - \delta_{45}\right)\right].
\end{aligned}$$

The decay rate of the states $|1\rangle$, $|2\rangle$, $|3\rangle$, $|4\rangle$ and $|5\rangle$ are given by Γ_1, Γ_2, Γ_3, Γ_4 and Γ_5, respectively. Again within the same weak probe limit, the coherences $\rho_{23} \approx \rho_{24} \approx \rho_{25} \approx 0$. Under the steady state condition i.e. $\dot{\rho}_{ij} = 0$, the equations (4.5) become

$$\rho_{12} = \frac{i}{2}\frac{\Omega_{12}}{\gamma_{12}} + \frac{i}{2}\frac{\Omega_{23}^{*}}{\gamma_{12}}\rho_{13}$$

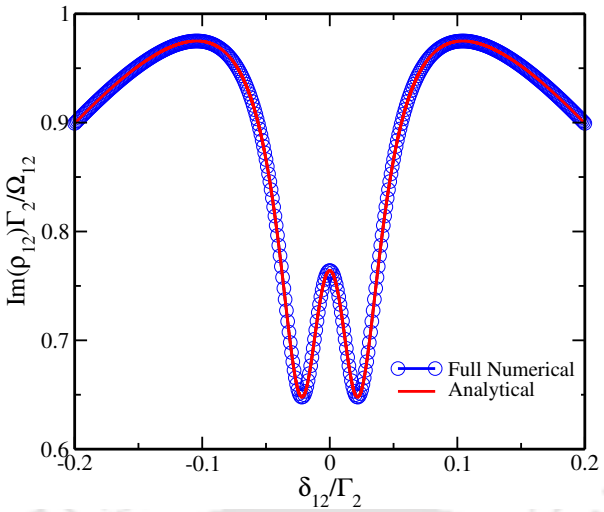

Fig. 4.2 (Color online). Comparison between analytical and numerical solution for normalized absorption, $\mathrm{Im}(\rho_{12})\Gamma_2/\Omega_{12}$ vs δ_{12}/Γ_2. The red solid curve corresponds to the analytical solution while blue open circle points correspond to the full numerical solution for Ω_{12}=$2\pi\times$ 0.01 MHz, $|\Omega_{23}|$=$|\Omega_{34}|$=$|\Omega_{45}|$=$2\pi\times$1 MHz, $|\Omega_{35}^{MW}|$=$2\pi\times$0.3 MHz, ϕ=$\pi/2$, δ_{23}=δ_{34}=δ_{45}=δ_{35}^{MW}=0, $\Gamma_1=\Gamma_3=\Gamma_5=0$ and $\Gamma_2=\Gamma_4=2\pi\times$ 6 MHz.

$$\begin{aligned}
\rho_{13} &= \frac{i}{2}\frac{\Omega_{23}}{\gamma_{13}}\rho_{12} + \frac{i}{2}\frac{\Omega_{34}^{*}}{\gamma_{13}}\rho_{14} + \frac{i}{2}\frac{\Omega_{35}^{MW*}}{\gamma_{13}}\rho_{15} \\
\rho_{14} &= \frac{i}{2}\frac{\Omega_{34}}{\gamma_{14}}\rho_{13} + \frac{i}{2}\frac{\Omega_{45}^{*}}{\gamma_{14}}\rho_{15} \\
\rho_{15} &= \frac{i}{2}\frac{\Omega_{35}^{MW}}{\gamma_{15}}\rho_{13} + \frac{i}{2}\frac{\Omega_{45}}{\gamma_{15}}\rho_{14}
\end{aligned} \tag{4.6}$$

We obtain following analytical expression for ρ_{12} by solving above linear algebraic equations

$$\rho_{12} = \frac{\frac{i}{2}\frac{\Omega_{12}}{\gamma_{12}}}{1+\frac{\frac{1}{4}\frac{|\Omega_{23}|^2}{\gamma_{12}\gamma_{13}}}{1+\frac{\frac{1}{4}\frac{|\Omega_{34}|^2}{\gamma_{13}\gamma_{14}}+\frac{i}{4}\frac{|\Omega_{34}||\Omega_{45}||\Omega_{35}^{MW}|cos\phi}{\gamma_{13}\gamma_{14}\gamma_{15}}+\frac{1}{4}\frac{|\Omega_{35}^{MW}|^2}{\gamma_{13}\gamma_{15}}}{1+\frac{1}{4}\frac{|\Omega_{45}|^2}{\gamma_{14}\gamma_{15}}}}} \tag{4.7}$$

where $\phi=\phi_{35}^{MW}-\phi_{34}^{L}-\phi_{45}^{L}$. In order to ensure the correctness of the above approximation, in Fig.(4.2) we plot the normalized absorption of the probe field ($\mathrm{Im}(\rho_{12})\Gamma_2/\Omega_{12}$) as a function of normalized probe detuning (δ_{12}/Γ_2) obtain from analytical expression of ρ_{12} as given in Eq.(4.7) as well as the complete numerical solution of density matrix equation as stated in Eq.(4.4). The numerical solution of density matrix equation is calculated for the parameters mentioned in caption of Fig. 4.2. We solve 25 coupled differential equations for ρ_{ij} where i=1 to 5, j=1 to 5, for the time $100/\Gamma_2$, which is much higher than steady state time ($1/\Gamma_2$). It is clear from Fig. 4.2 that the complete

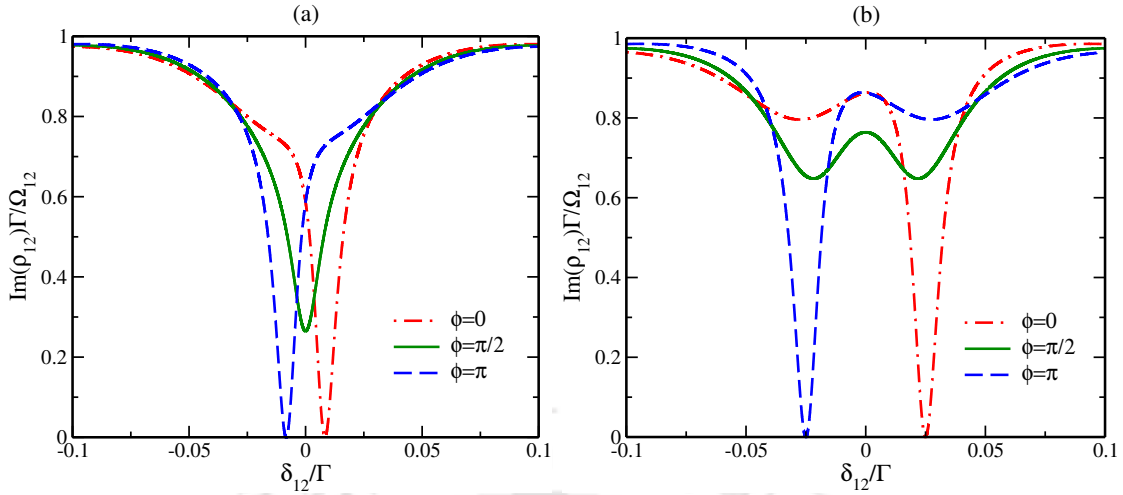

Fig. 4.3 (Color online). Normalized probe absorption $\mathrm{Im}(\rho_{12})\Gamma_2/\Omega_{12}$ vs probe detuning in unit of Γ_2 (δ_{12}/Γ_2) for (a) $|\Omega_{35}^{MW}|$=$2\pi\times$0.1 MHz (b) $|\Omega_{35}^{MW}|$=$2\pi\times$0.3 MHz. Other parameters are Ω_{12}=$2\pi\times$0.01 MHz, $|\Omega_{23}|$=$|\Omega_{34}|$=$|\Omega_{45}|$=$2\pi\times$1 MHz δ_{23}=δ_{34}=δ_{45}=δ_{35}^{MW}=0. The dashed dotted red, solid green and dashed blue curves represent $\phi = 0$, $\phi = \pi/2$ and $\phi = \pi$ respectively

numerical results are in an excellent agreement with the approximated analytical solutions.

4.3 Results and Discussions

4.3.1 Lineshape of the probe absorption

In this section, we study the effect of the MW field on the lineshape of the probe absorption. We consider all the control and MW fields are on the resonance. First we discuss the role of individual control fields one by one and finally the MW field. There is a broad Lorentzian profile having a full width at half maximum of Γ_2 which is $2\pi\times$ 6 MHz in this case [160, 161]. At the line centre of the Lorentzian profile, the probe response develops a sharp EIT dip in the presence of the control field Ω_{23} [160, 181]. The linewidth of EIT dip depends decoherence rates and the control field intensity $|\Omega_{23}|$ and can be expressed as $\Delta\omega \propto |\Omega_{23}|^2/4\Gamma_2$ [119]. Here we have taken Γ_1=Γ_3=0, as states $|1\rangle$ and $|3\rangle$ are the ground states. The control laser Ω_{34} recovers the absorption against EIT i.e. electromagnetically induced transparency and absorption and known as EITA has been discussed in details in our previous work [181]. When $|\Omega_{34}| < |\Omega_{23}|$ the linewidth of EITA peak is comparable with the linewidth of EIT dip and it is broadening with the increase of the Ω_{34}. Finally when $|\Omega_{34}| > |\Omega_{23}|$ the linewidth of the EITA peak will be Γ_2. In the presence of the control laser Ω_{45} there will be transparency against EITA, known as EITAT i.e. electromagnetically induced

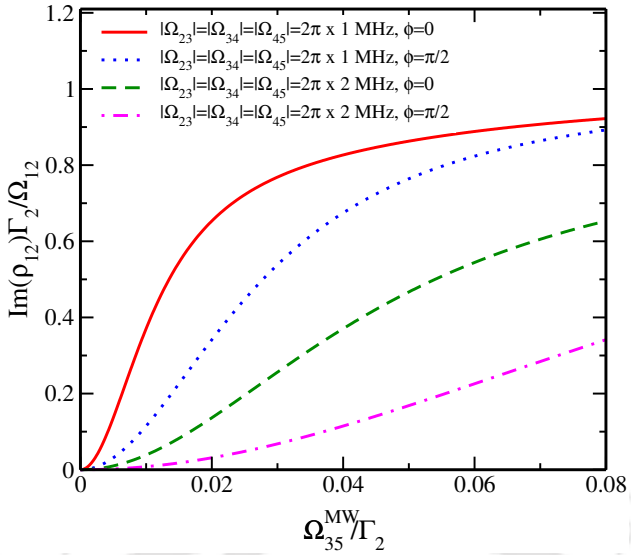

Fig. 4.4 (Color online). $\mathrm{Im}(\rho_{12})\Gamma_2/\Omega_{12}$ vs $\Omega_{35}^{MW}/\Gamma_2$ for Ω_{12}=$2\pi\times0.01$ MHz. The solid red curve is with $|\Omega_{23}| = |\Omega_{34}| = |\Omega_{45}|$=$2\pi\times1$ MHz and $\phi = 0$. The dashed green curve is with $|\Omega_{23}| = |\Omega_{34}|= |\Omega_{45}|$=$2\pi\times2$ MHz and $\phi = 0$. The dotted blue curve is with $|\Omega_{23}| = |\Omega_{34}|=|\Omega_{45}|$=$2\pi\times1$ MHz and $\phi = \pi/2$. The magenta dashed dotted curve is with $|\Omega_{23}| = |\Omega_{34}|=|\Omega_{45}|$=$2\pi\times2$ MHz and $\phi = \pi/2$. All fields are on resonance i.e. δ_{12}=δ_{23}=δ_{34}=δ_{45}=δ_{35}^{MW}=0

transparency, absorption and transparency and has also been discussed in our previous work [181]. The linewidth of the EITAT is given by the expression,

$$\Delta\omega \propto \frac{1}{4\Gamma_2} \times \frac{|\Omega_{23}||\Omega_{45}|}{\left[(|\Omega_{34}|^2 + |\Omega_{45}|^2)\left(\frac{1}{|\Omega_{23}|^2} + \frac{1}{|\Omega_{45}|^2} + \frac{|\Omega_{34}|^2}{|\Omega_{23}|^2|\Omega_{45}|^2}\right) - 1\right]}$$

The linewidth of the EITAT is modulated by the three control field intensities Ω_{23}, Ω_{34}, Ω_{45} and the decay rate of the excited states $|2\rangle$, $|4\rangle$. Here we have taken Γ_5=0, as state $|5\rangle$ is the metastable ground state. The MW field, Ω_{35}^{MW} splits or shifts the EITAT dip, depending upon the phase ϕ as below as shown in Fig. 4.3.

Fig. 4.3 shows the plot for normalized absorption ($\mathrm{Im}(\rho_{12})\Gamma_2/\Omega_{12}$) vs probe detuning in the unit of (Γ_2) for various combination of the phase and the MW field strength. In Fig. 4.3a for ϕ=0 there is shift of EITAT dip by approximately $\frac{|\Omega_{35}^{MW}|}{2}$ to the right while it shifts to the left by same amount for ϕ=π. For the $\phi = \pi/2$ there is broadening and reduction of the EITAT dip. However with the relatively high value of the MW field, $|\Omega_{35}^{MW}|$=$2\pi\times0.3$ MHz there is further reduction of EITAT dip and splitting increases and visible as shown in Fig. 4.3b.

4.3.2 Effect of the MW power

The variation of the normalized probe absorption as a function of the MW Rabi frequency, $|\Omega_{35}^{MW}|$ in unit of Γ_2 is shown in Fig. 4.4. As in the presence of the MW field the EITAT dip shift, thus with increase of the MW Rabi frequency the absorption increases and saturates to 1. The slope of the absorption profile depends upon the EITAT linewidth, and the narrower will be the linewidth sharper will be the slope. As we see in Fig. 4.4 the red solid curve shows the sharper rise in the absorption with the MW Rabi frequency as compared to the dashed green curve. This is because the EITAT dip linewidth is power broadened by the control laser with higher Rabi frequency. The red solid curve saturates faster as compare to the dotted blue curve this is because with $\phi = \pi/2$ the EITAT dip splits instead of shifting and hence will have lower slope as compare to the $\phi = 0$ with same Rabi frequency of the control lasers.

4.4 Closed loop Λ vs M-system

In this section, we discuss how the constraints of a closed loop Λ-system [183] can be overcome by considering a M-system in which the MW field couples the unpopulated ground states. In Fig. 4.5, we study the probe absorption lineshape as a function of detuning under three-photon resonance condition i.e. $\delta_{12} - \delta_{23} - \delta_{13} = 0$ for a closed loop Λ-system and a M-system. The lineshape under the approximation of no population transfer [183] is denoted by open circles in Fig. 4.5(a). A Lorentzian fit of the same (dashed blue curve) gives a linewidth of 0.028 Γ_2. A full numerical solution for this system displays a broader linewidth (0.1 Γ_2) as shown by the open sqaures. The broadening of the lineshape is due to the population transfer to the excited states which leads to fluorescence. The solid green curve in Fig. 4.5(b) shows the full numerical solution of the density matrix equation (4) at steady state condition for M-system. It is found that the Lorentzian linewidth of the absorption spectrum is 0.014 Γ_2 as shown by dashed blue curve. Therefore the Lorentzian linewidth of M-system is much smaller than the Lorentzian linewidth of closed loop Λ-system. Hence the population transfer can be suppressed in the former system by MW field which is not possible in the latter. Nevertheless, the transparency window can be shifted by changing the total phase of the system at a fixed linewidth. Thus M-systems driven by a MW field can efficiently select the carrier frequency of the probe field.

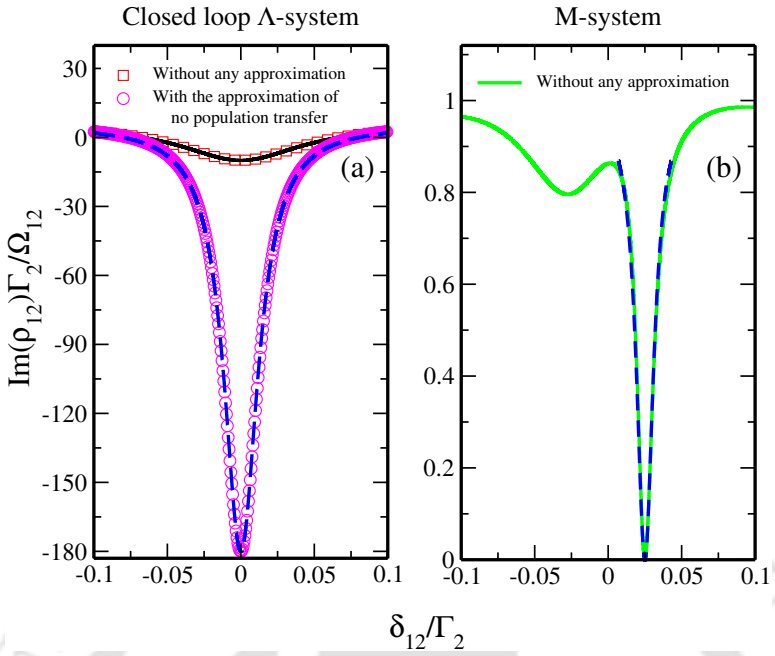

Fig. 4.5 (Color online). Normalized absorption, $\mathrm{Im}(\rho_{12})\Gamma_2/\Omega_{12}$ as a function of probe detuning, δ_{12} in unit of Γ_2 for (a) the closed loop Λ-system with $|\Omega_{12}|{=}2\pi{\times}0.01$ MHz, $|\Omega_{23}|{=}2\pi{\times}1$ MHz, $|\Omega_{35}^{MW}|{=}2\pi{\times}0.3$ MHz and $\phi = \pi/2$ (b) the M-system in which the parameters are $|\Omega_{12}|{=}2\pi{\times}0.01$ MHz, $|\Omega_{23}|{=}|\Omega_{34}|{=}|\Omega_{45}|{=}2\pi{\times}1$ MHz, $|\Omega_{35}^{MW}|{=}2\pi{\times}0.3$ MHz, $\delta_{23}{=}\delta_{34}{=}\delta_{45}{=}\delta_{35}^{MW}{=}0$ and $\phi = 0$.

4.5 Conclusion

In conclusion, we have studied how the strength and phase of the MW field can be efficiently used to manipulate the absorption property of the probe field in a five-level M-system. The transparency window of the probe field shifts or splits depending upon the phase of the MW field for the resonant control optical fields. The transparency window splits by an amount equal to the Rabi frequency of the MW field for $\pi/2$ phase while it shifts to higher or lower value by an amount half of the Rabi frequency of the MW field for the phase 0 or π of the same. We have also shown that M-system offers an order of magnitude narrower linewidth of the probe absorption spectrum as compare to the routinely studied Λ-system even at moderate strength of MW field. This is due to absence of MW field induced population transfer in the M-system in contrast to the Λ-system. The changes in the position of the transparency window in frequency space can enable us to select the desired carrier probe field frequency. Hence narrow probe absorption spectrum opens up a new avenue for atom based phase dependent MW magnetometry which has important applications in MW engineering and communications.

Chapter 5

Microwave assisted optical waveguide in Rydberg atoms

5.1 Introduction

The ability to guide a narrow width optical beam holds promise for applications in high-density optical communication [190] and high-resolution imaging [191, 192]. The main obstacle for realisation of narrow beam based optical technology comes from diffraction and absorption of the medium [193]. The divergence angle of a narrow beam is significantly larger as compared to broad beam due to its geometrical shape [194]. Consequently, the narrow beam encounters severe spatial distortions along the transverse direction as its propagates a few Rayleigh wavelengths distance through the medium. Ultimately diffraction induced image blurring prevents the important light based applications [190, 191]. Hence, the complete elimination of diffraction for the narrow width beam becomes a long-standing goal.

To achieve this goal, different methods based on Raman self-focusing technique [195–197], and manipulation of refractive index [28, 198, 199, 29] have been proposed in bulk medium [197, 198] as well as in atomic vapor medium [28, 29]. Suitable tailoring of refractive index along transverse direction leads to the form of waveguide like structure inside cold atomic medium [200, 199, 201] and also in hot vapor cell [27, 28, 88]. Truscott *et al*. published their seminal paper establishing that atomic vapor can produce a waveguide which controls beam propagation without diffraction [27]. This experiment opened a floodgate for numerous experiments [27, 202–205] in addition to theoretical investigations [28, 200, 29, 206, 207, 88, 202, 201]. A suitably chosen spatial profile of the control field that creates spatial modulation of refractive index which enables weak optical beams to propagate through the medium without loss of generality. Taking advantage of different spatial profiles of control field such as Gaussian

[200, 202, 208], super-Gaussian [88, 200] and different mode of Laguerre-Gaussian (LG_n^l) [29, 206, 209] results an undistorted probe beam dynamics. Off-resonance [29, 88] or nearly resonance atomic transitions [206, 210] can also support guiding and steering of optical beams. However, the optically written waveguide is based on normal atom with low principal quantum number and is often associated with considerable amount of absorption which limits lossless beam propagation for several Rayleigh lengths. Another drawback of normal atomic waveguide appear due to lack of high contrast in refractive index that fails to support narrow width beam propagation. These limitations can be overcome by exploiting the exaggerated optical properties of Rydberg atoms with high principal quantum number [32]. An atomic waveguide with narrow core and high contrast refractive index between the core and cladding is a very fundamental criteria for guiding a narrow beam with size of $5\mu m$.

In this chapter, we use highly excited Rydberg energy states of rubidium atom to create high contrast and narrow core optical waveguide. The inspiration of our work comes from recent experimental demonstrating by Shaffer *et al.* [155] wherein MW field becomes highly responsive to the Rydberg energy states [155, 211, 212, 90]. Even a very weak MW field ($8\ \mu V\, cm^{-1}$) can be able to modify the probe response drastically [155]. We exploit this sensitive behavior of the Rydberg energy states to create a highly efficient and extremely tunable atomic waveguide. A high contrast refractive index modulation of probe can be produced by application of LG shaped MW beam which couples two highly excited Rydberg states $|30D_{\frac{5}{2}}\rangle$, $|31P_{\frac{3}{2}}\rangle$ [211]. The desired spatial shape of the beam either in MW or optical domain can be found experimentally [213–217, 122, 123]. Note that dipole-dipole interaction mediated through the residual occupation in Rydberg states are very small in the considered model system [155, 211] and can be neglected safely.

Further, we assimilate inactive buffer gas atoms in addition to active Rydberg atoms inside the vapor cell to enhance the efficiency of the waveguide [203, 205, 218]. The active atoms frequently collide with the buffer gas atoms in which the velocity of the active atoms alter from one velocity group into another velocity group. This velocity changing collision (VCC) leads to the phenomena of Dicke narrowing [219, 220] in presence of buffer gas. In this chapter, we exploit buffer gas induced VCC process in order to create a high contrast and efficient atomic waveguide. The perspective of the current scheme is substantially unique from the preceding articles by two ways [203, 205, 206]. First, the key difference is the employing of spatially modulated MW beam between the Rydberg states. The spatial dependent MW LG_n^l beam generates a sharply varying fiber-like refractive index profile which is tightly confined in the central region of the transverse position ($r_\perp$). Second, the presence of buffer gas further manipulates the features of the waveguide by widening the transparency window and

enhancing the contrast of the refractive index profile. Therefore, the transmission of the weak diffraction controlled probe beam at medium output enhances from 10% to 40% in the presence of buffer gas unlike the results based on the absorptive systems reported earlier *et al.*[203, 205, 206]. Also the enhanced contrast in refractive index focused the probe beam tightly towards the center of the waveguide. Along with that the waveguide possesses an exclusive and handy feature in which the absorption and refractive index profile of the waveguide are squeezed from both side with the increase of MW intensity which makes this waveguide very efficient in guiding the probe beam of arbitrary width. Narrow beam broadens much faster than the wide beam because the divergence angle is inversely proportional to the beam width. Therefore, this high contrast and tunable atomic waveguide is essential for diffraction elimination from the narrow beam of any arbitrary mode.

The chapter is structured as follows. In section 5.2, we introduce the model configuration and describe the interaction of Rydberg atoms with the optical and MW fields by a semi-classical density matrix formalism. In section 5.3, we point out the advantage of using Rydberg atomic system over its normal counterpart by studying the probe susceptibility. Section 5.4 provides how the spatial structure of the MW beam permits us to build an optical waveguide. In section 5.5, we discuss the tunability of the atomic waveguide. Section 5.6 demonstrates the propagation of weak probe field having different beam profiles through the atomic waveguide. Finally, we briefly conclude our work in section 5.7.

5.2 Theoretical model

5.2.1 Model Configuration

In this work, we study the collective behavior of active Rydberg atoms in the presence of inactive buffer gas atoms at room-temperature. The geometry of the model system under consideration is shown in Fig. 5.1(a) where two counter propagating optical fields and MW field interact with the active ^{87}Rb atoms. Figure 5.1(b) shows four energy levels of active atoms which include one metastable ground state $|1\rangle$ and three excited states $|2\rangle$, $|3\rangle$, $|4\rangle$ [155, 211]. The ground state $|1\rangle$=$|5S_{\frac{1}{2}}, F = 2, m_F = 2\rangle$ is coupled to an excited state $|2\rangle$=$|5P_{\frac{3}{2}}, F = 3, m_F = 3\rangle$ by a weak probe field. Two highly excited Rydberg states $|3\rangle = |30D_{\frac{5}{2}}, m_J = \frac{5}{2}\rangle$ and $|4\rangle$=$|31P_{\frac{3}{2}}, m_J = \frac{3}{2}\rangle$ are coupled by a moderately intense MW field of frequency 84.2 GHz [211]. A strong control field connects two states $|2\rangle$ and $|3\rangle$. The electric fields associated with the electro-magnetic

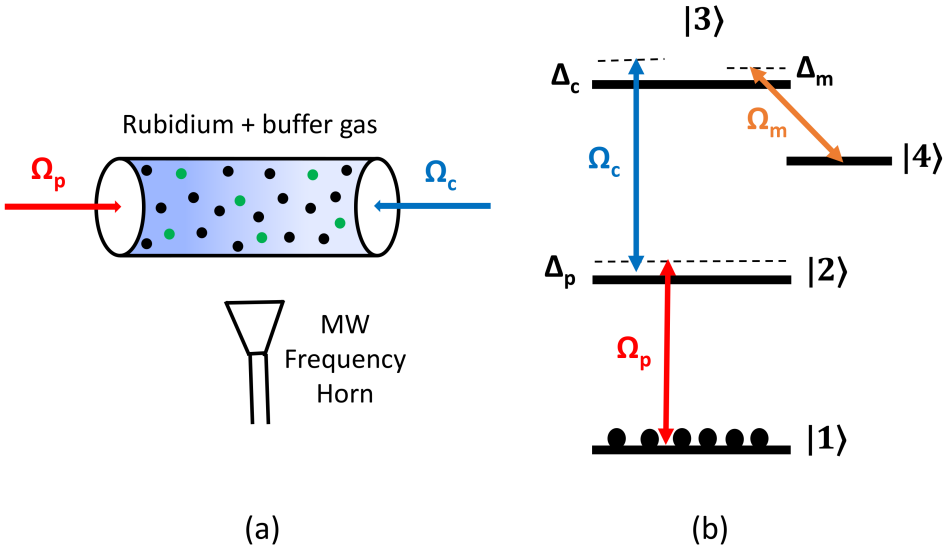

Fig. 5.1 (a) A simple illustration of the model system. The vapor cell contains active Rubidium atoms (black dots) and inactive buffer gas atoms (green dots). Two counter-propagating optical fields Ω_p, Ω_c and one MW field interact with the active atoms. (b) Schematic representation of the four level system. The energy levels have been realized in ^{87}Rb atomic vapor where $|1\rangle$=$|5S_{\frac{1}{2}}, F = 2, m_F = 2\rangle$, $|2\rangle$=$|5P_{\frac{3}{2}}, F = 3, m_F = 3\rangle$, $|3\rangle$=$|30D_{\frac{5}{2}}, m_J = \frac{5}{2}\rangle$, $|4\rangle$=$|31P_{\frac{3}{2}}, m_J = \frac{3}{2}\rangle$.

(EM) radiations are described as

$$\vec{E}_j(\vec{r},t) = \hat{e}_j \mathcal{E}_j(\vec{r}) e^{i(k_j z - \omega_j t)} + c.c., \tag{5.1}$$

where $\mathcal{E}_j(\vec{r})$, k_j, ω_j and $\hat{e}_j$ are the slowly varying envelope, wave number, frequency and unit polarization vector of the EM fields respectively. The indices $j \in \{p, c, m\}$ refer to the probe, control and MW field. The EM fields only interact with the active atoms and the interaction can be expressed as a time-dependent Hamiltonian under the electric dipole approximation :

$$\begin{aligned} H' &= \hbar\omega_{21} |2\rangle\langle 2| + \hbar(\omega_{21} + \omega_{32}) |3\rangle\langle 3| + \hbar(\omega_{21} + \omega_{32} - \omega_{34}) |4\rangle\langle 4| \\ &- \hbar\Omega_p e^{-i\omega_p t} |2\rangle\langle 1| - \hbar\Omega_c e^{-i\omega_c t} |3\rangle\langle 2| - \hbar\Omega_m e^{-i\omega_m t} |3\rangle\langle 4| + h.c., \end{aligned} \tag{5.2}$$

where Ω_p, Ω_c, Ω_m are the Rabi frequencies of the probe, control and MW fields respectively. The expression of Rabi frequencies are

$$\Omega_p = \frac{\vec{d}_{21}.\hat{e}_p}{\hbar}\mathcal{E}_p, \quad \Omega_c = \frac{\vec{d}_{32}.\hat{e}_c}{\hbar}\mathcal{E}_c \quad \text{and} \quad \Omega_m = \frac{\vec{d}_{34}.\hat{e}_m}{\hbar}\mathcal{E}_m. \tag{5.3}$$

In order to acquire the time-independent Hamiltonian, we execute the following unitary transformation

$$H = U^{\dagger} H^{'} U - i\hbar U^{\dagger} \frac{\partial U}{\partial t}, \tag{5.4}$$

where U is defined as

$$U = e^{-i(\omega_p |2\rangle\langle 2| + (\omega_p+\omega_c)|3\rangle\langle 3| + (\omega_p+\omega_c-\omega_m)|4\rangle\langle 4|)t}. \tag{5.5}$$

Now the Hamiltonian transforms into the following time-independent form

$$\begin{aligned} H = &- \hbar\Delta_p |2\rangle\langle 2| - \hbar(\Delta_p + \Delta_c)|3\rangle\langle 3| - \hbar(\Delta_p + \Delta_c - \Delta_m)|4\rangle\langle 4| \\ &- \hbar\Omega_p |2\rangle\langle 1| - \hbar\Omega_c |3\rangle\langle 2| - \hbar\Omega_m |3\rangle\langle 4| + h.c. \end{aligned} \tag{5.6}$$

where $\Delta_p = \omega_p - \omega_{21}$, $\Delta_c = \omega_c - \omega_{32}$, and $\Delta_m = \omega_m - \omega_{34}$, are the detuning of the probe, control and MW field respectively.

5.2.2 Dynamical Equations

The dynamics of the active atoms inside the vapor cell are governed by the following Liouville's equation :

$$\dot{\rho} = -\frac{i}{\hbar}[H, \rho] + \mathcal{L}_{\rho} \tag{5.7}$$

where the second term incorporates various radiative and non-radiative decay processes in the presence of buffer gas atoms. The collisions between the active atoms and buffer gas atoms interrupt the velocity distribution of the active atoms and also the phase coherence between the atomic energy levels which modifies the life-time of the atomic coherence [221–225]. The effect of such collision can be included in the dynamical Eq. (5.7) by adding the following term [221, 222, 224]

$$\begin{aligned} \left[\frac{\partial \rho_{jk}(v,t)}{\partial t}\right]_{collision} &= -\gamma_{ph}(1-\delta_{jk})\rho_{jk}(v,t) - \Gamma_{jk}\rho_{jk}(v,t) \\ &+ \int K(v' \to v)\rho_{jk}(v',t)dv' \end{aligned} \tag{5.8}$$

In the above Eq. (5.8), Γ_{jk} is known as velocity changing collision rate and γ_{ph} is the rate of collisional dephasing of the atomic coherence. The collision kernel, $K(v' \to v)$ represents the probability density per unit time that active atoms have their velocity changed from v' to v as a result of collisions with buffer gas atoms [221]. For simplicity,

the collision kernel can be written in terms of Γ_{jk} as shown in the following expression

$$\begin{aligned} K(v' \to v) &= \Gamma_{jk} M(v), \\ M(v) &= \frac{1}{\sqrt{\pi} v_{th}} e^{-\frac{v^2}{v_{th}^2}}, \quad v_{th} = \sqrt{\frac{2k_B T}{m_A}}, \end{aligned} \tag{5.9}$$

where $M(v)$ and v_{th} are the Maxwell-Boltzmann velocity distribution along the z direction and most probable velocity of the active atoms of mass m_A at a temperature T. The spontaneous decay rates from the excited state $|j\rangle$, $(j \in 2, 3, 4)$ to the ground state $|1\rangle$, are denoted by γ_{j1}. Note that collision rate of different atomic states Γ_{j1}, $j \in 2, 3, 4$ are all similar in strength and are indicated by $\Gamma_{21} \simeq \Gamma_{31} \simeq \Gamma_{41}$=$\Gamma_c$ [224]. In the considered model system, k_p ($\simeq 2\pi \times 1.3\ \mu m^{-1}$) is nearly equal to k_c ($\simeq 2\pi \times 2.0\ \mu m^{-1}$) such that wave vector difference $|\delta\vec{k}| = |\vec{k}_p - \vec{k}_c|$ becomes minimal. Further, we restrict our analysis for the moderate collision case in which Γ_c is comparatively smaller than spontaneous decay rate (γ_{21}) and Doppler width (γ_d) *i.e.* $\Gamma_c \ll \gamma_{21}, \gamma_d$ [224, 155]. The degree of collisions can be realized experimentally by controlling the density of the buffer gas inside the vapor cell. The collision induced Γ_c significantly influences the absorptive and dispersive features of the atomic medium.

The following three coupled density matrix equations are sufficient for describing the dynamics of the active atoms in the buffer gas environment under weak probe approximation

$$\begin{aligned} \dot{\rho}_{21}(v,t) =& - A_{21}(v)\rho_{21}(v,t) + i\Omega_p(\rho_{11}(v,t) - \rho_{22}(v,t)) + i\Omega_c^*\rho_{31}(v,t), \\ \dot{\rho}_{31}(v,t) =& - A_{31}(v)\rho_{31}(v,t) + i\Omega_c\rho_{21}(v,t) - i\Omega_p\rho_{32}(v,t) \\ & + i\Omega_m\rho_{41}(v,t) + \Gamma_{31}M(v)\int \rho_{31}(v,t)dv, \\ \dot{\rho}_{41}(v,t) =& - A_{41}(v)\rho_{41}(v,t) + i\Omega_m^*\rho_{31}(v,t) - i\Omega_p\rho_{42}(v,t) \\ & + \Gamma_{41}M(v)\int \rho_{41}(v,t)dv, \end{aligned}$$

where

$$\begin{aligned} A_{21}(v) =& i(\vec{k}_p.\vec{v} - \Delta_p) + \gamma_{21} + \Gamma_{21} + \gamma_{ph}, \\ A_{31}(v) =& i\{(\vec{k}_p + \vec{k}_c).\vec{v} - (\Delta_p + \Delta_c)\} + \gamma_{31} + \Gamma_{31} + \gamma_{ph}, \\ A_{41}(v) =& i\{(\vec{k}_p + \vec{k}_c - \vec{k}_m).\vec{v} - (\Delta_p + \Delta_c - \Delta_m)\} + \gamma_{41} + \Gamma_{41} + \gamma_{ph}. \end{aligned}$$

The perturbative solution of the atomic coherence and population in the limits of weak probe approximation can be defined as

$$\rho_{jk} = \rho_{jk}^{(0)} + \Omega_p\rho_{jk}^{(1)} \tag{5.10}$$

The zeroth order solution in absence of probe field is $\rho_{11}^{(0)} = M(v)$ [224]. The first order solution in presence of weak probe field can be obtained in the following form

$$\begin{aligned}
\dot{\rho}_{21}^{(1)}(v,t) &= -A_{21}(v)\rho_{21}^{(1)}(v,t) + i\rho_{11}^{(0)} + i\Omega_c^*\rho_{31}^{(1)}(v,t),\\
\dot{\rho}_{31}^{(1)}(v,t) &= -A_{31}(v)\rho_{31}^{(1)}(v,t) + i\Omega_c\rho_{21}^{(1)}(v,t)\\
&\quad + i\Omega_m\rho_{41}^{(1)}(v,t) + \Gamma_{31}M(v)\int\rho_{31}^{(1)}(v,t)dv,\\
\dot{\rho}_{41}^{(1)}(v,t) &= -A_{41}(v)\rho_{41}^{(1)}(v,t) + i\Omega_m^*\rho_{31}^{(1)}(v,t)\\
&\quad + \Gamma_{41}M(v)\int\rho_{41}^{(1)}(v,t)dv.
\end{aligned}$$

The steady state response of the above coupled equations *i.e.*, $\dot{\rho}_{jk}^{(1)} = 0$ can be used for finding the analytical expression of first order atomic coherence $\langle\rho_{21}\rangle$, $\langle\rho_{31}\rangle$ and $\langle\rho_{41}\rangle$. We also incorporated the thermal agitation of the atom by performing the velocity averaging of the atomic coherence

$$\begin{aligned}
\langle\rho_{21}\rangle &= \int\rho_{21}^{(1)}(v)dv,\\
&= i\Omega_P f_{10}(r) + i\Omega_c^*\Gamma_{31}f_3(r)\langle\rho_{31}^{(1)}\rangle - \Omega_c^*\Omega_m\Gamma_{41}f_1(r)\langle\rho_{41}^{(1)}\rangle,\\
\langle\rho_{31}^{(1)}\rangle &= \int\rho_{31}^{(1)}(v)dv,\\
&= \Omega_p\Omega_c\left[\frac{|\Omega_m|^2 f_1(r)L_2 - f_3(r)L_3}{L_1L_3 + |\Omega_m|^2L_2L_4}\right],\\
\langle\rho_{41}^{(1)}\rangle &= \int\rho_{41}^{(1)}(v)dv,\\
&= -i\Omega_p\Omega_c\Omega_m^*\left[\frac{f_1(r)L_1 + f_3(r)L_4}{L_1L_3 + |\Omega_m|^2L_2L_4}\right],
\end{aligned}$$

where

$$\begin{aligned}
L_1 &= 1 + |\Omega_c|^2\Gamma_{31}f_8(r) - \Gamma_{31}f_5(r),\\
L_2 &= \Gamma_{41}f_4(r) - |\Omega_c|^2\Gamma_{41}f_6(r),\\
L_3 &= 1 - |\Omega_c|^2|\Omega_m|^2\Gamma_{41}f_9(r) - \Gamma_{41}f_2(r) + |\Omega_m|^2\Gamma_{41}f_7(r),\\
L_4 &= \Gamma_{31}f_4(r) - |\Omega_c|^2\Gamma_{31}f_6(r).
\end{aligned}$$

The expression of the spatial functions $f_j(r)$, ($j \in$ 1,2,3,... 10) are shown in the appendix section (5.15). Finally, the velocity averaged linear probe susceptibility, $\langle\chi_{21}\rangle$

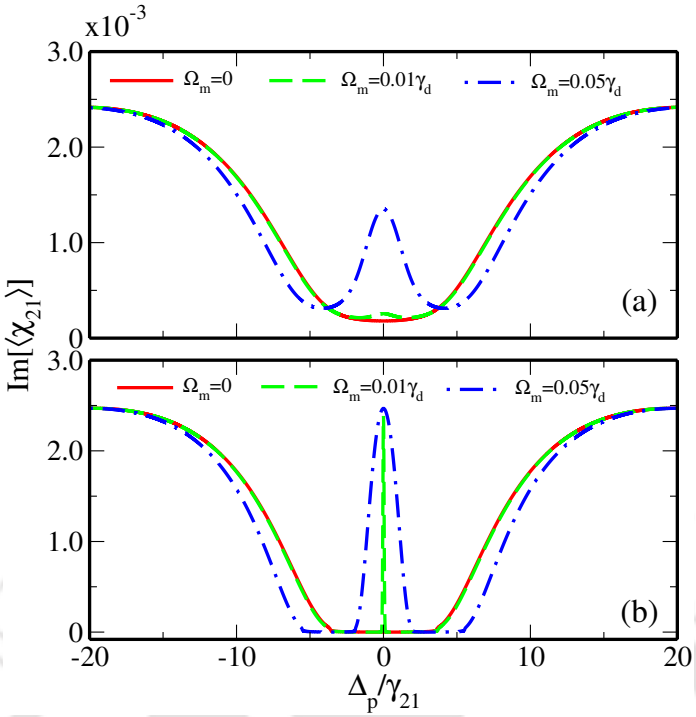

Fig. 5.2 Probe absorption profile, Im$[\langle\chi_{21}\rangle]$ as a function of probe laser detuning (Δ_p) for (a) normal (b) Rydberg atomic system. EIA lineshapes for three different values of MW field (Ω_m) demonstrate the MW field sensitivity. Decay rate for (a) $\gamma_{31} \simeq \gamma_{41} \simeq \gamma_{21}$ and for (b) $\gamma_{31} = 2\pi \times 1.0 \times 10^3$ Hz, $\gamma_{41} = 2\pi \times 0.5 \times 10^3$ Hz. The other parameters are $\Omega_c = 0.3\gamma_d$, $\Delta_c = 0$, $\Delta_m = 0$, $\Gamma_c = 0$, T=300K, $\mathcal{N} = 5 \times 10^{10}$ atoms/cm^3, $\gamma_d = 2.53 \times 10^9$ Hz, $\gamma_{21} = 2\pi \times 6.1 \times 10^6$ Hz, $\gamma_{ph} \approx 1 \times 10^3$ Hz.

at frequency ω_p can be written as

$$\langle\chi_{21}\rangle = \frac{\mathcal{N}|\vec{d}_{21}|^2}{\hbar\Omega_p}\langle\rho_{21}\rangle \tag{5.11}$$

where $\mathcal{N}$ is the atomic density.

5.3 Microwave field sensitivity

In this section, we distinguish the advantage of using Rydberg atomic system over its normal counterpart by studying the probe susceptibility in the absence and presence of the MW field. In Rydberg atomic system, MW field couples two Rydberg states with high principal quantum number as shown in Fig. 5.1(b). Whereas MW field connects two states with very low principal quantum number for normal atomic system. In Fig. 5.2(a) and 5.2(b), we compare the probe absorption lineshape in case of normal as well as Rydberg atomic system for three different values of MW field intensity Ω_m=0, 0.01γ_d, 0.05γ_d. In absence of MW field (Ω_m=0), both the normal and Rydberg

atomic system displays electromagnetically induced transparency (EIT) [226, 227] under two-photon resonance condition *i.e.*, $\Delta_p = \Delta_c$ as shown by solid red curve in Fig. 5.2. We have observed that Rydberg system offers complete flat transparency window (no absorption) due to the low decay rate ($\sim$ KHz) of the Rydberg states as compared to a shallow window exists in the normal atomic states (decay rate $\sim$ MHz) [79]. We next study how a weak MW field (Ω_m=$0.01\gamma_d$) drastically modify the probe response in Rydberg system which is distinct from normal system. It is clear from 5.2(b) that a complete sharp electromagnetically induced absorption (EIA) peak [228, 229] presence in Rydberg system. On the other hand, the EIA peak in normal atomic system just build up as shown with dash green curve in Fig. 5.2(a). With the increase of MW field power (Ω_m=$0.05\gamma_d$), Rydberg EIA peak experiences power broadening, while the normal EIA peak is still growing towards its maximum peak value. These observations clearly confirms that Rydberg energy states are strongly responsive to the MW field unlike the normal atomic states [155]. We exploit this responsive behavior of MW field in Rydberg atomic system to create a highly tuneable atomic waveguide. The effective modulation of spatial susceptibility due to spatial structure of the MW beam holds the main essence behind the formation of waveguide inside the Rydberg atomic system.

5.4 Formation of atomic waveguide

We now investigate how the spatial structure of the MW beam permits us to build an optical waveguide inside the atomic medium. A waveguide like refractive index can be formed by considering the transverse profile of the MW beam to be Laguerre-Gaussian (LG_n^l) together with a Gaussian (LG_0^0) shaped control beam. The spatial shape of the LG_n^l beam in cylindrical coordinate can be expressed as [194],

$$\begin{aligned}\Omega_j(r,\phi,z) = \Omega_j^0 \frac{w_j}{w_j(z)} \left(\frac{r\sqrt{2}}{w_j(z)}\right)^{|l|} e^{-\frac{r^2}{w_j^2(z)}} e^{il\phi} \\ \times L_n^l\left(\frac{2r^2}{w_j^2(z)}\right) e^{\frac{ik_j r^2}{2R_j(z)}} e^{-i(2n+l+1)\tan^{-1}\left(\frac{z}{z_j}\right)}, \\ r = \sqrt{x^2+y^2}, \quad \phi = \tan^{-1}\left(\frac{y}{x}\right).\end{aligned} \tag{5.12}$$

The input amplitude is denoted by Ω_j^0, $R_j(z) = z + (z_j^2/z)$ is the radius of curvature and $z_j = \pi w_j^2/\lambda_j$ is the Rayleigh length of the beam. The spot size of the beam is defined as $w_j(z) = w_j\sqrt{1+(z/z_j)^2}$, where w_j is the minimum beam waist at z=0. The indices $j \in \{m, c, p\}$ denotes the MW, control and probe beams, respectively.

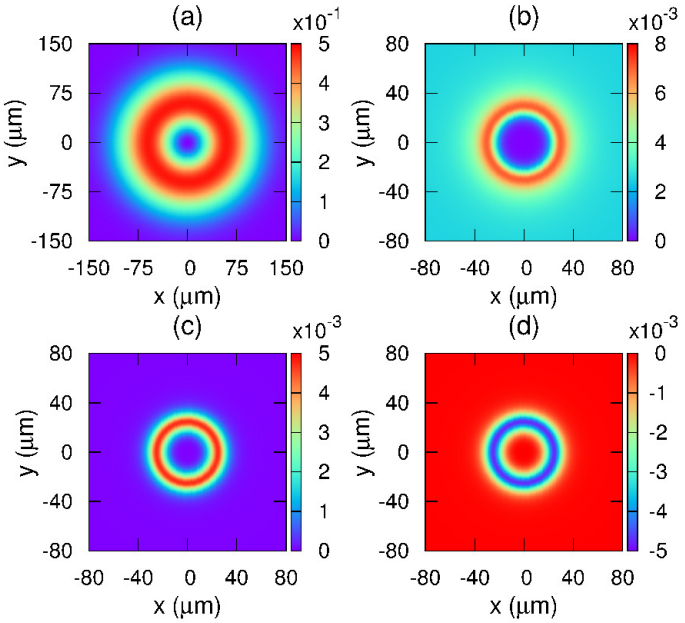

Fig. 5.3 (a) Input doughnut shaped Laguerre-Gaussian (LG_0^2) MW beam, (b) Fiber-like absorption profile tightly confined in the central region of transverse position (x,y) with $\Delta_p = \pm 0.001\gamma_{21}$, (c) Red shifted detuning ($\Delta_p = -0.001\gamma_{21}$) and (d) Blue shifted detuning ($\Delta_p = 0.001\gamma_{21}$) depict anti-waveguide like and waveguide like refractive index profile in the transverse position (x,y) respectively. The parameters are $\Omega_c = 0.3\gamma_d$, $\Omega_m = 0.01\gamma_d$, $\omega_c = 60\mu m$, $\omega_m = 60\mu m$, $l_m = 2$. All other parameters are same as in 5.2.

The spatial inhomogeneous intensity distribution of LG_0^2 beam as shown in Fig. 5.3(a). It is clear from Fig. 5.3(a) that the doughnut shaped LG_0^2 MW beam has zero intensity at the central region whereas maximum intensity occurs in the ring-shaped region. Therefore, LG_0^2 MW beam together with Gaussian control beam can be used to obtain the desired spatial refractive profile of the probe beam as follows. Fig. 5.3(b) shows the transverse variation of the probe absorption. A complete transparency window exists at the core because of dominant characteristics of control beam over the MW field. The diminishing intensity of the control beam toward the wing region yields absorption at the cladding. Simultaneously MW field gain maximum intensity in the bright ring which causes high probe absorption due to EIA as shown in Fig. 5.3(b). Hence, considering suitable spatial structure of the two fields allows us to achieve probe transparency at the core and opaqueness at cladding both at resonance condition and near resonance detuned situation. Fig. 5.3(d) display that the refractive index attains a maximum value at EIT dominant region and forms the core of the atomic waveguide. The cladding section of the waveguide can be cast by EIA, since EIT is ineffective in the ring-shaped region. The induced waveguide structure consists of refractive variation between core and cladding accompanied with a small width of core.

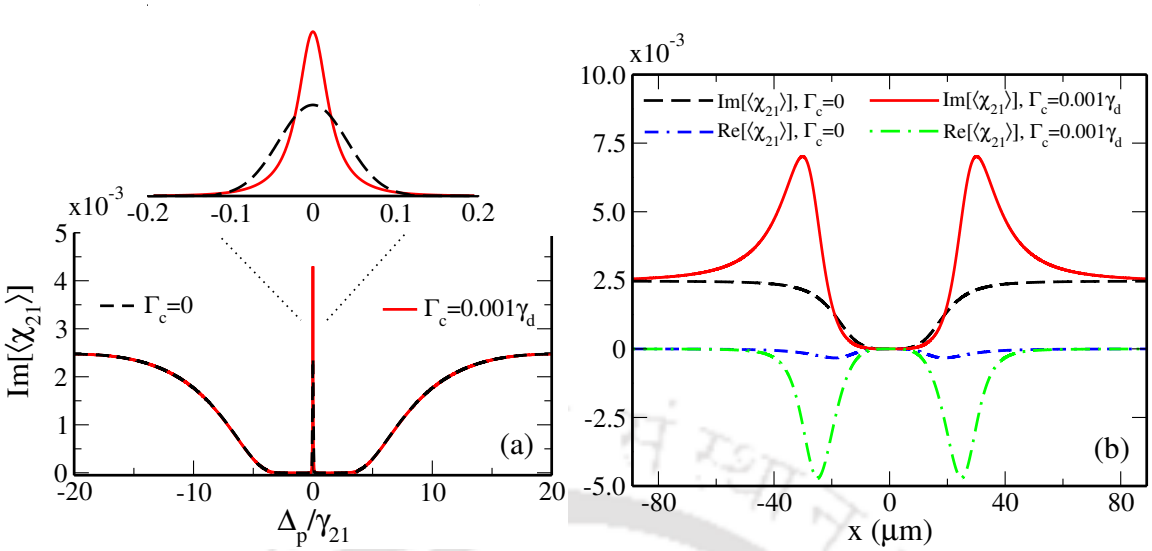

Fig. 5.4 (a) Probe absorption is plotted as a function of probe field detuning in the presence and absence of VCC. Inset zoom figure shows the Dicke narrowing and enhancing of the EIA peak due to Γ_c. (b) Real and imaginary part of the susceptibility is plotted as a function of transverse position x at y=0 plane for two different values of Γ_c. The parameters are $\Omega_c = 0.3\gamma_d$, $\Omega_m = 0.01\gamma_d$, $\Delta_p = 0.001\gamma_{21}$. All other parameters are same as in 5.2.

Hence the spatial response of the medium for the probe field exhibits waveguide like structure at blue detuned condition whereas at red detuned condition, it changes to the anti-waveguide like structure as shown in Fig. 5.3(c). In both the cases, the core region of the atomic wave guide display minimum absorption as shown in Fig. 5.3(b). Finally, we have chosen the blue detuned probe field condition, *i.e.*, $\Delta_p = 0.001\gamma_{21}$ for efficient guiding of various narrow Gaussian and Hermit Gaussian with arbitrary modes.

5.5 Tunability of the waveguide

Next, we discuss how the buffer gas induced collision significantly manoeuvres the features of the atomic waveguide along the transverse direction in the presence of MW field (Ω_m^0). In order to comprehend the reasons behind these manipulations of atomic waveguide, we plot the probe absorption lineshape as a function of Δ_p in the absence and presence of VCC as shown in Fig. 5.4(a). The MW induced EIA peak in Fig. 5.4(a) can be enhanced by a notable amount in the presence of VCC. Along with that the EIA lineshape manifests Dicke like narrowing due to the collision process as displayed in the inset of Fig. 5.4(a). Fig. 5.4(b) illustrates that the contrast of refractive index significantly enhances in the presence of VCC. The slope of VCC

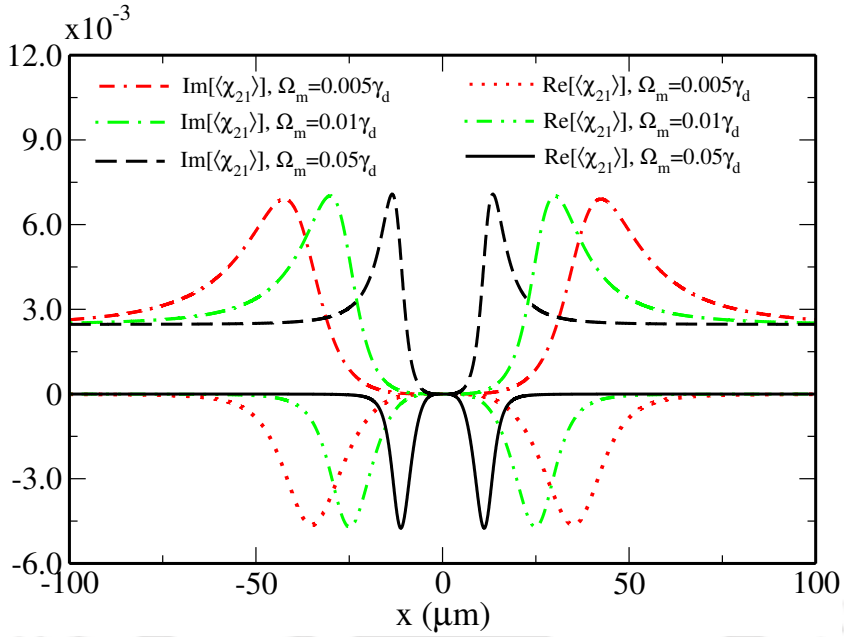

Fig. 5.5 Medium susceptibility is plotted for different values of MW field intensity along the transverse position x at y=0 plane. The parameters are $\Omega_c = 0.3\gamma_d$, $\Delta_p = 0.001\gamma_{21}$, $\Gamma_c = 0.001\gamma_d$. All other parameters are same as in 5.2.

induced refractive index profile is remarkably sharp which makes this waveguide more efficient in guiding the narrow probe beam in comparison to that of a Kerr field induced waveguide [206]. Further, the transparency window of the waveguide becomes much wider and steeper in the presence of buffer gas. As a result, a narrow probe beam propagates through the waveguide without significant loss of intensity. These VCC induced Dicke narrowing and enhancing of the EIA peak distinctly facilitate the waveguide characteristics.

Now, we delineate how the MW field intensity effects the induced atomic waveguide. In Fig. 5.5, we plot imaginary and real part of the probe susceptibility along the transverse position for three different values of MW field intensity. We observe that absorption profile and refractive index of the waveguide are squeezed from both sides with the increase of MW intensity. This unique feature creates sharply varying and confined refractive index profile which makes the waveguide very efficient in guiding the light beam. It is familiar that narrow beam broadens more rapidly than the wide beam due to optical diffraction because divergence angle ($\Theta = 2\lambda_p/\pi w_p$) is inversely proportional to the beam width w_p [194]. Hence, this high-contrast and squeeze waveguide is highly desired in order to remove diffraction from the narrow beam.

5.6 Beam propagation through the waveguide

Next, we study the propagation of weak probe field having different beam profiles through the atomic waveguide. The beam propagation dynamics is governed by the Maxwell's wave equations [29, 206]. Under slowly varying envelope and paraxial wave approximation, Maxwell's wave equations for the probe beam transform into the following form

$$\frac{\partial \Omega_p}{\partial z} = \frac{i}{2k_p}\nabla_\perp^2 \Omega_p + 2i\pi k_p \langle \chi_{21} \rangle \Omega_p. \tag{5.13}$$

In Eq. (5.13), second order partial derivative in the xy plane *i.e.* $\nabla_\perp^2 = (\partial^2/\partial x^2 + \partial^2/\partial y^2)$ incorporates inherent optical diffraction of the probe beam. The last term of Eq. (5.13) is the contribution of linear and nonlinear optical effects which includes MW and buffer gas induced absorption and refractive index profile of the medium in order to suppress the diffraction. Note that we have considered tightly focused MW beam. Therefore, the diffraction of the MW beam is negligible. We adopt split-step Fourier method (SSFM) to obtain the numerical solution of Eq. (5.13) and demonstrate the effect of spatially varying absorption and refractive index on probe beam dynamics. First, we study the propagation dynamics of a Gaussian (LG_0^0) probe beam. The width of the probe beam is 5 μm which remains within the limit of paraxial wave approximation, $\lambda_p/2\pi w_p < 0.1$ [230, 206]. The propagation dynamics of the narrow Gaussian shaped probe beam through the high contrast atomic waveguide is shown in Fig. 5.6. The input and output intensity profile of the probe beam in the presence and absence of the MW beam and buffer gas are illustrated clearly. In absence of MW LG_0^2 beam, the probe beam suffers diffraction induced broadening along with large absorption as shown with double-dashed-dot magenta curve in Fig. 5.6. The diffraction of the probe beam is drastically reduced in the presence of MW LG_0^2 beam. We notice that the output intensity of the probe beam decreases below 10% in absence of buffer gas after the propagation of $z = 5z_p$. The situation changes in the presence of buffer gas, and the transmissivity of the diffraction controlled probe beam enhances over 40% for the same propagation distance ($z = 5z_p$). This efficient beam propagation without any diffraction is possible due to the presence of high-contrast tunable optical waveguide in buffer gas medium.

In order to prove the robustness of the atomic waveguide, we also demonstrate diffraction-less propagation of arbitrary Hermite-Gaussian (HG_n^m) modes. A further reason to choose HG_n^m modes of narrow width is its direct application in super-resolution imaging [231, 192]. The spatial profile of different HG_n^m modes at medium entrance

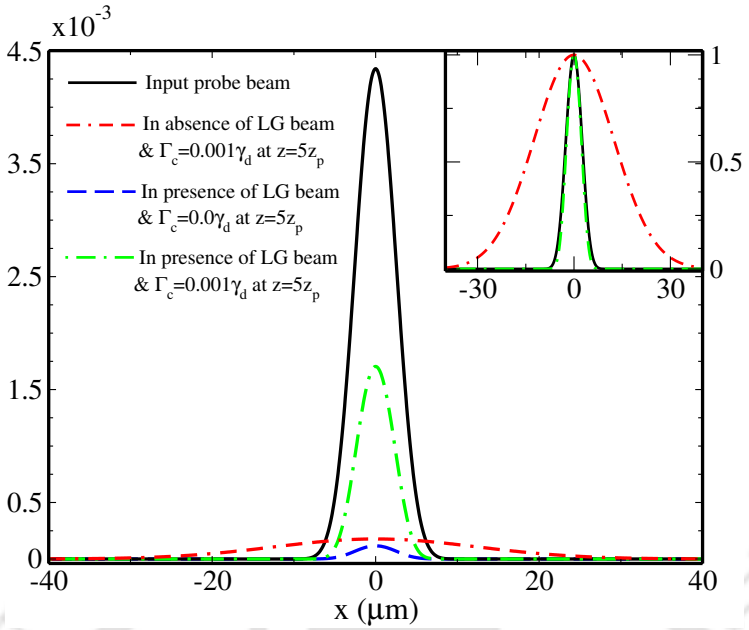

Fig. 5.6 Narrow Gaussian beam ($\omega_p = 5\mu m$) propagation through the atomic medium in presence and absence of MW LG_0^2 beam and buffer gas. Inset figure shows the normalised intensity profile of the probe beam in presence and absence of MW LG_0^2. All other parameters are same as in figure 5.5.

$(z = 0)$ is given by

$$\Omega_p(x, y, 0) = \Omega_p^0 H_n\left(\frac{\sqrt{2}x}{w_p}\right) H_m\left(\frac{\sqrt{2}y}{w_p}\right) e^{-\frac{x^2+y^2}{w_p^2}}, \tag{5.14}$$

where H_n and H_m are the Hermite polynomials of order n and m respectively. For demonstration, we propel the Hermite-Gaussian probe beam of mode $n = 1$, $m = 1$ through the waveguide. The intensity profile of the HG_1^1 mode at $z = 0$ is shown in Fig. 5.7(a). The diffraction of the beam in absence of MW LG_0^2 beam and buffer gas is displayed in Fig. 5.7(b). The presence of LG_0^2 beam eliminates the diffraction completely as shown in Fig. 5.7(c) and Fig. 5.7(d). However, Fig. 5.7(d) clearly shows that the diffraction-less HG_1^1 beam becomes tightly focused towards the centre of the waveguide due to the sharply varying refractive index in the presence of buffer gas medium. The transverse structure of the MW beam and buffer gas play the important role in guiding the weak probe beam of narrow width and arbitrary modes.

5.7 Conclusion

In conclusion, we have demonstrated an efficient scheme to generate MW assisted optical waveguide in an inhomogeneously broadened vapor medium that is made

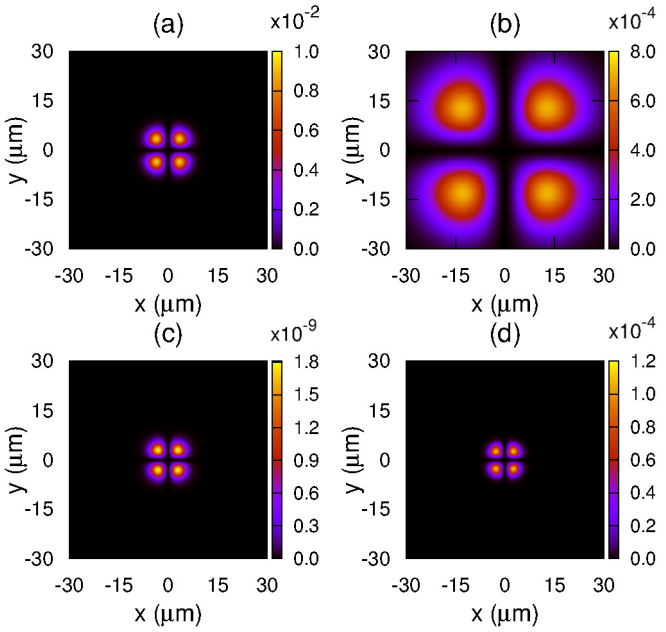

Fig. 5.7 (a) Intensity profile of the probe beam (HG_1^1) at z=0. (b) Intensity profile of the probe beam (HG_1^1) in absence of MW LG_0^2 beam at z=5z_p. Intensity profile of the probe beam (HG_1^1) in presence of MW LG_0^2 beam after propagation over 5 Rayleigh lengths (z=5z_p) through the atomic medium (c) without and (d) with the buffer gas environment. All other parameters are same as in figure 5.6.

of active ^{87}Rb atoms and inactive buffer gas atoms. The sensitive behaviour of MW field coupled between two highly excited Rydberg states of Rb atoms allow us to create a responsive atomic susceptibility. The structured MW LG_0^2 beam and Gaussian control beam together build an optical waveguide with amenable fiber like refractive index profile. The presence of buffer gas induced collision further manipulates the features of the waveguide by widening the spatial transparency window and enhancing the contrast of the refractive index. The increasing intensity of the MW field squeezes the high contrast waveguide from both sides which duly guides the probe beam of narrow width. We numerically solve Maxwell's equations to demonstrate diffractionless propagation of narrow paraxial light beam of arbitrary modes such as Gaussian, Hermite-Gaussian HG_1^1 to several Rayleigh lengths. The output intensity of diffractionless light significantly enhances in the presence of buffer gas. This efficient technique to eliminate diffraction from narrow light beams have important applications in high-density optical communication [190] and high-resolution imaging [191, 231, 192].

Appendix

$$f_1(r) = \int \frac{M(v)}{f_D(v)} dv, \quad f_2(r) = \int \frac{M(v)}{A_{41}(v)} dv,$$
$$f_3(r) = \int \frac{A_{41}(v)M(v)}{f_D(v)} dv, \quad f_4(r) = \int \frac{M(v)}{A_{31}(v)A_{41}(v) + |\Omega_m|^2} dv,$$
$$f_5(r) = \int \frac{A_{41}(v)M(v)}{A_{31}(v)A_{41}(v) + |\Omega_m|^2} dv,$$
$$f_6(r) = \int \frac{A_{41}(v)M(v)}{(A_{31}(v)A_{41}(v) + |\Omega_m|^2)\, f_D(v)} dv,$$
$$f_7(r) = \int \frac{M(v)}{(A_{31}(v)A_{41}(v) + |\Omega_m|^2)\, A_{41}(v)} dv,$$
$$f_8(r) = \int \frac{A_{41}^2(v)M(v)}{(A_{31}(v)A_{41}(v) + |\Omega_m|^2)\, f_D(v)} dv,$$
$$f_9(r) = \int \frac{M(v)}{(A_{31}(v)A_{41}(v) + |\Omega_m|^2)\, f_D(v)} dv,$$
$$f_{10}(r) = \int \frac{M(v)\,(A_{31}(v)A_{41}(v) + |\Omega_m|^2)}{f_D(v)} dv,$$

where

$$f_D(v) = A_{21}(v)\left(A_{31}(v)A_{41}(v) + |\Omega_m|^2\right) + A_{41}(v)|\Omega_c|^2.$$

Chapter 6

Conclusions and Future Outlook

In conclusion, this thesis reports coherent generation and control of electro-magnetic fields in different atomic systems. The properties of atomic systems are manipulated by using the atomic coherence induced by coherent atom-light interaction. The variation of optical properties such as absorption, dispersion and diffraction are the key for efficient generation and control of electro-magnetic fields in these systems. In the following, we concisely present important conclusions of each work and discuss the future outlook of the problem.

In chapter 2, we have shown an efficient generation and control of a non-degenerate FWM signal in an inhomogeneously broadened atomic medium. The generated FWM signal is a scaled copy of the input probe pulse which travels through the atomic medium along with the probe pulse without changing its intensity and shape. We have demonstrated the generation, control, storage and retrieval of various complicated shaped FWM signal such Gaussian, secant hyperbolic and amplitude modulated signal. The similar FWM generation scheme can be extended to other coherent atomic systems which may generate multiple FWM signals simultaneously. The coherent control of multiple FWM signals have important applications in signal processing in optical communication as well as in quantum information science.

In chapter 3, we have discussed how the nonlinear FWM process in an atomic system facilitates the translation of OAM associated with two optical fields to the generated FWM signal. In this scheme, two strong optical fields transfer a large fraction of populations from ground state to upper excited state. This populations spontaneously decay into an intermediate state by emitting an infrared radiation of wavelength 5.23 μm. Simultaneously, this triggers the generation of a FWM signal at 420 nm along the direction of the optical fields. We have demonstrated that the vortex modes imprinted on the probe or control beam are transferred into the 420 nm FWM signal with high

fidelity. This scheme can be investigated further to translate OAM from the optical fields to the generated 5.23 μm infrared signal. Apart from OAM translation, the storage and retrieval of OAM in such atomic systems can have promising applications in optical communication and quantum information processing systems.

In chapter 4, we have studied a five level M-system and three level Λ-system in presence of MW field which couples two unpopulated ground states in M-system whereas it acts on one of the populated states in Λ-system. Therefore, the population transfer is unavoidable in the presence of high power MW field in closed loop Λ-system. In this work, we have shown how the limitations of routinely studied Λ-system can be overcome in the M-system. We have also shown that M-system offers an order of magnitude narrower probe absorption linewidth as compare to the Λ-system. The M-system can be studied further for atom based phase dependent MW magnetometry which has important applications in MW engineering and communications.

In chapter 5, we have demonstrated an optical waveguide in an inhomogeneously broadened vapor medium that is made of active ^{87}Rb atoms and inactive buffer gas atoms. The structured MW LG_0^2 beam and Gaussian control beam together build the high contrast and narrow core waveguide inside the atomic medium. We have demonstrated diffractionless propagation of narrow paraxial light beam of arbitrary single mode such as Gaussian, Hermite-Gaussian HG_1^1 to several Rayleigh lengths. The presence of buffer gas significantly enhances output intensity of diffraction controlled light beam. Currently, this induced waveguide eliminates diffraction only from a single mode paraxial beam. We investigate further to build a multi-mode atomic waveguide in these medium which has important applications in high-capacity optical communication.

Appendix A

Numerical Methods for Maxwell's Equations

A.1 Numerical solution of light beam equation

The propagation equation of a paraxial light beam, $\Omega_p(x, y, z)$ is given by

$$\frac{\partial \Omega_p}{\partial z} = \frac{i}{2k_p}\nabla_\perp^2 \Omega_p + 2\pi i k_p \chi \Omega_p, \tag{A.1}$$

where $\nabla_\perp^2 = (\partial^2/\partial x^2 + \partial^2/\partial y^2)$ is known as transverse Laplacian operator. Now, we describe how to solve Eq. (A.1) numerically using the split step Fourier method (SSFM). First, we express the overhead propagation equation in the following operator form

$$\frac{\partial \Omega_p}{\partial z} = (\hat{\mathcal{D}} + \hat{\mathcal{S}})\Omega_p, \tag{A.2}$$

where $\hat{\mathcal{D}} = (i/2k_p)\nabla_\perp^2 = (i/2k_p)\,(\partial^2/\partial x^2 + \partial^2/\partial y^2)$ is a differential operator which incorporates inherent optical diffraction of the light beam and $\hat{\mathcal{S}} = 2\pi i k_p \chi$ is a nonlinear operator which includes dispersion and absorption profile of the medium. A general solution of Eq. (A.2) for a small propagation distance δz is

$$\Omega_p(x, y, z + \delta z) = \exp[(\hat{\mathcal{D}} + \hat{\mathcal{S}})\delta z]\Omega_p(x, y, z) \tag{A.3}$$

Now, we expand the exponential function $\exp[(\hat{\mathcal{D}}+\hat{\mathcal{S}})\delta z]$ in the following form [232, 233]

$$\exp[(\hat{\mathcal{D}} + \hat{\mathcal{S}})\delta z] = \exp\left[\hat{\mathcal{D}}\delta z + \hat{\mathcal{S}}\delta z + \frac{1}{2}[\hat{\mathcal{D}}, \hat{\mathcal{S}}]\delta z^2 + \cdots\right]. \tag{A.4}$$

We consider that the step size δz is very small. So, we safely neglect the higher-order terms in Eq. (A.4). Now, the above equation reduces to

$$\exp[(\hat{\mathcal{D}} + \hat{\mathcal{S}})\delta z] \simeq \exp[\hat{\mathcal{D}}\delta z]\exp[\hat{\mathcal{S}}\delta z] \tag{A.5}$$

We substitute Eq. (A.5) into Eq. (A.3) to obtain the numerical solution of Eq. (A.1)

$$\Omega_p(x, y, z + \delta z) = \exp[\hat{\mathcal{D}}\delta z]\exp[\hat{\mathcal{S}}\delta z]\Omega_p(x, y, z) \tag{A.6}$$

We compute the first operation *i.e.* $\exp[\hat{\mathcal{S}}\delta z]\Omega_p(x, y, z)$ in position domain where $\Omega_p(x, y, z)$ is the initial value of the light beam. In the next step, we perform a Fourier transform.

$$\text{First Step :} \qquad \exp[2\pi i k_p \chi \delta z]\Omega_p(x, y, z) \tag{A.7}$$

$$\text{Second Step :} \qquad \mathcal{F}\left[\exp[2\pi i k_p \chi \delta z]\Omega_p(x, y, z)\right] \tag{A.8}$$

where $\mathcal{F}$ denotes the Fourier transform. The partial derivatives $\partial/\partial x$ and $\partial/\partial y$ in position space becomes ik_x and ik_y in frequency space. Therefore, the operator $\exp[\hat{\mathcal{D}}\delta z]$ in the fourier space can be written as

$$\exp[\hat{\mathcal{D}}\delta z] = \exp\left[\frac{-i(k_x^2 + k_y^2)\delta z}{2k_p}\right] \tag{A.9}$$

Now, we employ the exponential operator $\exp[\hat{\mathcal{D}}\delta z]$ in frequency domain.

$$\text{Third Step :} \qquad \exp\left[\frac{-i(k_x^2 + k_y^2)\delta z}{2k_p}\right]\mathcal{F}\left[\exp[2\pi i k_p \chi \delta z]\Omega_p(x, y, z)\right] \tag{A.10}$$

Next, we use the inverse Fourier transform $\mathcal{F}^{-1}$ to write the final solution in the position space.

$$\text{Fourth Step :} \qquad \mathcal{F}^{-1}\left[\exp\left[\frac{-i(k_x^2 + k_y^2)\delta z}{2k_p}\right]\mathcal{F}\left[\exp[2\pi i k_p \chi \delta z]\Omega_p(x, y, z)\right]\right] \tag{A.11}$$

Therefore, the solution after a single step δz can be written as

$$\Omega_p(x, y, z + \delta z) = \mathcal{F}^{-1}\left[\exp\left[\frac{-i(k_x^2 + k_y^2)\delta z}{2k_p}\right]\mathcal{F}\left[\exp[2\pi i k_p \chi \delta z]\Omega_p(x, y, z)\right]\right] \tag{A.12}$$

A.2 Numerical solution of light pulse equation

The propagation equation of a light pulse $\Omega_p(z,t)$ is given by

$$\frac{\partial \Omega_p}{\partial z} + \frac{1}{c}\frac{\partial \Omega_p}{\partial t} = 2\pi i k_p \chi \Omega_p. \tag{A.13}$$

We numerically solve Eq. $(A.13)$ in a reference frame with local time $\tau = t - \frac{z}{c}$ and space $\xi = z$. Eq. $(A.13)$ in new reference frame reshape into the following form

$$\frac{\partial \Omega_p}{\partial \xi} = i\eta_p \rho(\xi,\tau) \tag{A.14}$$

We integrate the partial differential Eq. (A.14) to study the spatio-temporal evolution of the light pulse. The solution of $\Omega_p(\xi,\tau)$ is made possible because we know input value of the pulse $\xi = 0$ plane. The initial value of $\Omega_p(\xi = 0,\tau)$ is utilized to determine the value of atomic coherence $\rho(\xi = 0,\tau)$. Next, we substitute $\rho(\xi = 0,\tau)$ in Eq. (A.14) and determine the value of the pulse $\Omega_p(\xi + \delta\xi,\tau)$ for a small propagation distance $\delta\xi$. In the next iteration, we use $\Omega_p(\xi + \delta\xi,\tau)$ to determine the value of atomic coherence $\rho(\xi + \delta\xi,\tau)$. In this way, the numerical solution Eq. (A.14) is achieved for the whole space-time (ξ,τ).

List of publications

1. Nawaz Sarif Mallick, Tarak Nath Dey, Kanhaiya Pandey, *"Microwave assisted transparency in a M-system"*, Journal of Physics B: Atomic, Molecular and Optical Physics, **50**, 195502 (2017).

2. Nawaz Sarif Mallick, Tarak Nath Dey, *"Generation, control, storage and retrieval of complicated shaped four wave mixing signal"*, Journal of Physics B: Atomic, Molecular and Optical Physics, **53**, 045402 (2020).

3. Nawaz Sarif Mallick, Tarak Nath Dey, *Four-wave mixing based orbital angular momentum translation*, J. Opt. Soc. Am. B **37**, 1857-1864 (2020).

4. Nawaz Sarif Mallick, Tarak Nath Dey, *Microwave assisted optical waveguide in Rydberg atoms*, (communicated).

5. Nawaz Sarif Mallick and Tarak Nath Dey, *"Efficient generation of a degenerate four-wave mixing signal from a four level N-type atomic system"*, International Conference on Fibre Optics and Photonics, W3A. **49** (2016).

Schools and Conferences attended

1. **ICTS School on Frontiers in Light-Matter Interactions (ICTS-LMI2014)** held at Indian Association for the Cultivation of Science, Kolkata during December 8-18, 2014.

2. **13th International Conference on Fiber Optics and Photonics (PHOTONICS-2016)** held at Indian Institute of Technology Kanpur, Kanpur during December 5-8, 2016.

3. **Research Conclave 2017** held at Indian Institute of Technology Guwahati, Guwahati during March 16-19, 2017.

4. **SERB School on Frontiers in Quantum Optics** held at Indian Institute of Technology Guwahati, Guwahati during December 1-19, 2017.

5. **International Conference on Recent Trends in Cold and Ultracold Matter (ULTRACOLD 2018)** held at Indian Institute of Technology Guwahati, Guwahati during March 27-29, 2018.

References

[1] S. E. Harris, Phys. Today **50**, 36 (1997).

[2] M. Fleischhauer, A. Imamoglu, and J. P. Marangos, Rev. Mod. Phys. **77**, 633 (2005).

[3] B. Peng *et al.*, Nature **5**, (2014).

[4] A. Lazoudis *et al.*, Phys. Rev. A **83**, 063419 (2011).

[5] S. Sharma, B. Deb, and T. N. Dey, Journal of Physics B: Atomic, Molecular and Optical Physics **48**, 175502 (2015).

[6] K. Ichimura, K. Yamamoto, and N. Gemma, Phys. Rev. A **58**, 4116 (1998).

[7] J. J. Longdell, E. Fraval, M. J. Sellars, and N. B. Manson, Phys. Rev. Lett. **95**, 063601 (2005).

[8] A. A. Abdumalikov *et al.*, Phys. Rev. Lett. **104**, 193601 (2010).

[9] P. M. Anisimov, J. P. Dowling, and B. C. Sanders, Phys. Rev. Lett. **107**, 163604 (2011).

[10] S. Zhang *et al.*, Phys. Rev. Lett. **101**, 047401 (2008).

[11] M. Parvinnezhad Hokmabadi *et al.*, Scientific Reports **5**, (2015).

[12] N. Papasimakis, V. A. Fedotov, N. I. Zheludev, and S. L. Prosvirnin, Phys. Rev. Lett. **101**, 253903 (2008).

[13] S. Weis *et al.*, Science **330**, 1520 (2010).

[14] C. Dong, V. Fiore, M. C. Kuzyk, and H. Wang, Science **338**, 1609 (2012).

[15] P. S. Light *et al.*, Opt. Lett. **32**, 1323 (2007).

[16] X. Yang, M. Yu, D.-L. Kwong, and C. W. Wong, Phys. Rev. Lett. **102**, 173902 (2009).

[17] D. D. Smith *et al.*, Phys. Rev. A **69**, 063804 (2004).

[18] L. Vestergaard Hau, S. E. Harris, Z. Dutton, and C. H. Behroozi, Nature **397**, (1999).

[19] D. Budker, D. F. Kimball, S. M. Rochester, and V. V. Yashchuk, Phys. Rev. Lett. **83**, 1767 (1999).

[20] D. Han, H. Guo, Y. Bai, and H. Sun, Physics Letters A **334**, 243 (2005).

[21] D. F. Phillips *et al.*, Phys. Rev. Lett. **86**, 783 (2001).

[22] T. N. Dey and G. S. Agarwal, Phys. Rev. A **67**, 033813 (2003).

[23] A. Krishna, K. Pandey, A. Wasan, and V. Natarajan, EPL (Europhysics Letters) **72**, 221 (2005).

[24] S. Jin, Y. Li, and M. Xiao, Optics Communications **119**, 90 (1995).

[25] H. Schmidt and A. Imamoglu, Opt. Lett. **21**, 1936 (1996).

[26] Y. qing Li and M. Xiao, Opt. Lett. **21**, 1064 (1996).

[27] A. G. Truscott, M. E. J. Friese, N. R. Heckenberg, and H. Rubinsztein-Dunlop, Phys. Rev. Lett. **82**, 1438 (1999).

[28] R. Kapoor and G. S. Agarwal, Phys. Rev. A **61**, 053818 (2000).

[29] T. N. Dey and J. Evers, Phys. Rev. A **84**, 043842 (2011).

[30] N. Radwell *et al.*, Phys. Rev. Lett. **114**, 123603 (2015).

[31] S. Sharma and T. N. Dey, Phys. Rev. A **96**, 033811 (2017).

[32] T. F. Gallagher, *Rydberg Atoms* (Cambridge University Press, ADDRESS, 1994).

[33] J. D. Pritchard, *Cooperative Optical Non-Linearity in a Blockaded Rydberg Ensemble* (Springer Theses, ADDRESS, 2012).

[34] A. V. Gorshkov *et al.*, Phys. Rev. Lett. **107**, 133602 (2011).

[35] T. Peyronel *et al.*, Nature **488**, (2012).

[36] M. Muller *et al.*, Phys. Rev. Lett. **102**, 170502 (2009).

[37] H. Gorniaczyk *et al.*, Phys. Rev. Lett. **113**, 053601 (2014).

[38] R. K. V., T. N. Dey, J. Evers, and M. Kiffner, Phys. Rev. A **92**, 023840 (2015).

[39] V. Wong *et al.*, Phys. Rev. A **65**, 013810 (2001).

[40] H. Sun, Y. Niu, S. Jin, and S. Gong, Journal of Physics B: Atomic, Molecular and Optical Physics **40**, 3037 (2007).

[41] A. Lezama, G. C. Cardoso, and J. W. R. Tabosa, Phys. Rev. A **63**, 013805 (2000).

[42] H. Kang, G. Hernandez, and Y. Zhu, Phys. Rev. A **70**, 061804 (2004).

[43] Y. Cai *et al.*, Phys. Rev. A **91**, 013843 (2015).

[44] H. Wang, C. Fabre, and J. Jing, Phys. Rev. A **95**, 051802 (2017).

[45] G. S. Agarwal, T. N. Dey, and S. Menon, Phys. Rev. A **64**, 053809 (2001).

[46] A. Eilam, A. D. Wilson-Gordon, and H. Friedmann, Opt. Lett. **34**, 1834 (2009).

[47] R. K. V., T. N. Dey, S. Das, and P. K. Jha, Opt. Lett. **40**, 2229 (2015).

[48] H. M. Gibbs, Phys. Rev. Lett. **29**, 459 (1972).

[49] U. Fano, Phys. Rev. **124**, 1866 (1961).

[50] S. P. Tewari and G. S. Agarwal, Phys. Rev. Lett. **56**, 1811 (1986).

[51] K.-J. Boller, A. Imamoğlu, and S. E. Harris, Phys. Rev. Lett. **66**, 2593 (1991).

[52] J. D. Jackson, *Classical Electrodynamics*, 3rd ed. (Wiley, New York, 1999).

[53] M. O. Scully and M. S. Zubairy, *Quantum Optics* (Cambridge University Press, Cambridge, 1997).

[54] V. L. Allen and J. H. Eberly, *Optical Resonance and Two Level Atoms* (Wiley, New York, 1975).

[55] L. Allen and M. Padgett, Optics Communications **184**, 67 (2000).

[56] L. Allen, M. W. Beijersbergen, R. J. C. Spreeuw, and J. P. Woerdman, Phys. Rev. A **45**, 8185 (1992).

[57] G. Molina-Terriza, J. P. Torres, and L. Torner, Nature Physics **3**, 305 (2007).

[58] S. M. Barnett, M. Babiker, and M. J. Padgett, Philosophical Transactions of the Royal Society A: Mathematical, Physical and Engineering Sciences **375**, 20150444 (2017).

[59] S. Franke-Arnold, Philosophical Transactions of the Royal Society A: Mathematical, Physical and Engineering Sciences **375**, 20150435 (2017).

[60] G. Gibson *et al.*, Opt. Express **12**, 5448 (2004).

[61] A. E. Willner *et al.*, Philosophical Transactions of the Royal Society A: Mathematical, Physical and Engineering Sciences **375**, 20150439 (2017).

[62] H. He, M. E. J. Friese, N. R. Heckenberg, and H. Rubinsztein-Dunlop, Phys. Rev. Lett. **75**, 826 (1995).

[63] J. Ng, Z. Lin, and C. T. Chan, Phys. Rev. Lett. **104**, 103601 (2010).

[64] N. B. Simpson, K. Dholakia, L. Allen, and M. J. Padgett, Opt. Lett. **22**, 52 (1997).

[65] M. E. J. Friese, J. Enger, H. Rubinsztein-Dunlop, and N. R. Heckenberg, Phys. Rev. A **54**, 1593 (1996).

[66] V. Garcés-Chávez *et al.*, Phys. Rev. Lett. **91**, 093602 (2003).

[67] A. T. O'Neil, I. MacVicar, L. Allen, and M. J. Padgett, Phys. Rev. Lett. **88**, 053601 (2002).

[68] T. Omatsu *et al.*, Opt. Express **18**, 17967 (2010).

[69] K. Toyoda *et al.*, Nano Letters **12**, 3645 (2012).

[70] G. Vicidomini, P. Bianchini, and A. Diaspro, Nature Methods **15**, 173 (2018).

[71] H. Yang *et al.*, Optik **127**, 3735 (2016).

[72] V. V. Kotlyar *et al.*, J. Opt. Soc. Am. A **22**, 849 (2005).

[73] V. Kotlyar *et al.*, J. Opt. Technol. **74**, 686 (2007).

[74] M. Beijersbergen, L. Allen, H. van der Veen, and J. Woerdman, Optics Communications **96**, 123 (1993).

[75] N. R. Heckenberg, R. McDuff, C. P. Smith, and A. G. White, Opt. Lett. **17**, 221 (1992).

[76] N. Matsumoto *et al.*, J. Opt. Soc. Am. A **25**, 1642 (2008).

[77] A. J. Lee, T. Omatsu, and H. M. Pask, Opt. Express **21**, 12401 (2013).

[78] M. Okida, T. Omatsu, M. Itoh, and T. Yatagai, Opt. Express **15**, 7616 (2007).

[79] G. S. Agarwal, in *Quantum Optics* (Cambridge University Press, ADDRESS, 2012), pp. 385–412.

[80] H. R. Hamedi, J. Ruseckas, and G. Juzeliūnas, Journal of Physics B: Atomic, Molecular and Optical Physics **50**, 185401 (2017).

[81] R. Liu *et al.*, Phys. Rev. A **96**, 053823 (2017).

[82] D. Arsenović *et al.*, Phys. Rev. A **98**, 023829 (2018).

[83] A. K. Patnaik, F. L. Kien, and K. Hakuta, Phys. Rev. A **69**, 035803 (2004).

[84] H. Nakao and N. Yamamoto, Journal of Physics B: Atomic, Molecular and Optical Physics **50**, 065501 (2017).

[85] R. Zhang and X.-B. Wang, Phys. Rev. A **94**, 063856 (2016).

[86] O. Katz and O. Firstenberg, Nature Communications **9**, (2018).

[87] O. Firstenberg, C. S. Adams, and S. Hofferberth, Journal of Physics B: Atomic, Molecular and Optical Physics **49**, 152003 (2016).

[88] N. Cui, Z. Gan, and L. Zhang, Scientific Reports **7**, 14198 (2017).

[89] H. R. Hamedi and G. Juzeliunas, Phys. Rev. A **91**, 053823 (2015).

[90] N. S. Mallick, T. N. Dey, and K. Pandey, Journal of Physics B: Atomic, Molecular and Optical Physics **50**, 195502 (2017).

[91] P. Béjot and J. Kasparian, Phys. Rev. A **97**, 063835 (2018).

[92] G. Dmochowski *et al.*, Phys. Rev. Lett. **116**, 173002 (2016).

[93] F. A. M. de Oliveira, C. B. de Araújo, and J. R. Rios Leite, Phys. Rev. A **38**, 5688 (1988).

[94] J. P. Lopez, M. P. Moreno, M. H. G. de Miranda, and S. S. Vianna, Journal of Physics B: Atomic, Molecular and Optical Physics **50**, 085001 (2017).

[95] A. M. Akulshin, A. A. Orel, and R. J. McLean, Journal of Physics B: Atomic, Molecular and Optical Physics **45**, 015401 (2011).

[96] T. Jeong and H. S. Moon, Opt. Express **24**, 28774 (2016).

[97] B. S. Ham and P. R. Hemmer, Phys. Rev. Lett. **84**, 4080 (2000).

[98] A. Kölle *et al.*, Phys. Rev. A **85**, 063821 (2012).

[99] C.-Y. Lee *et al.*, Opt. Express **24**, 1008 (2016).

[100] Z.-Y. Liu *et al.*, Scientific Reports **7**, 15796 (2017).

[101] J.-Y. Juo *et al.*, Phys. Rev. A **97**, 053815 (2018).

[102] H.-C. Li, G.-Q. Ge, and M. S. Zubairy, Phys. Rev. A **97**, 053826 (2018).

[103] D. A. Braje *et al.*, Phys. Rev. Lett. **93**, 183601 (2004).

[104] S. S. Sahoo, A. Bhowmick, and A. K. Mohapatra, Journal of Physics B: Atomic, Molecular and Optical Physics **50**, 055501 (2017).

[105] Y. Zhang, A. W. Brown, C. Gan, and M. Xiao, Journal of Physics B: Atomic, Molecular and Optical Physics **40**, 3319 (2007).

[106] H. Kang, G. Hernandez, and Y. Zhu, Phys. Rev. Lett. **93**, 073601 (2004).

[107] C.-K. Chiu *et al.*, Phys. Rev. A **89**, 023839 (2014).

[108] J.-B. Li, M.-D. He, and L.-Q. Chen, Opt. Express **22**, 24734 (2014).

[109] J.-B. Li *et al.*, Opt. Express **25**, 25663 (2017).

[110] R. M. Camacho, P. K. Vudyasetu, and J. C. Howell, Nat Photon **3**, 103 (2009).

[111] A. Raczynski and J. Zaremba, Optics Communications **209**, 149 (2002).

[112] N. B. Phillips, A. V. Gorshkov, and I. Novikova, Phys. Rev. A **83**, 063823 (2011).

[113] J. Wu *et al.*, Phys. Rev. A **87**, 013845 (2013).

[114] M. Hosseini *et al.*, Journal of Physics B: Atomic, Molecular and Optical Physics **45**, 124004 (2012).

[115] D. Xu, C. Hang, and G. Huang, Phys. Rev. A **98**, 043848 (2018).

[116] N. Lauk, C. O'Brien, and M. Fleischhauer, Phys. Rev. A **88**, 013823 (2013).

[117] N. B. Phillips *et al.*, Journal of Modern Optics **60**, 64 (2013).

[118] Y. Wu and X. Yang, Phys. Rev. A **70**, 053818 (2004).

[119] M. Fleischhauer and M. D. Lukin, Phys. Rev. A **65**, 022314 (2002).

[120] M. Fleischhauer and M. D. Lukin, Phys. Rev. Lett. **84**, 5094 (2000).

[121] L. Allen, M. Padgett, and M. Babiker, Progress in Optics **39**, 291 (1999).

[122] M. J. Padgett and L. Allen, Journal of Optics B **4**, S17 (2002).

[123] L. Zhu and J. Wang, Scientific Reports **4**, (2014).

[124] J. Wang *et al.*, Nature Photonics **6**, 488 (2012).

[125] F. Tamburini *et al.*, Phys. Rev. Lett. **97**, 163903 (2006).

[126] G. Gariepy *et al.*, Phys. Rev. Lett. **113**, 153901 (2014).

[127] J. E. Curtis and D. G. Grier, Phys. Rev. Lett. **90**, 133901 (2003).

[128] L. J. Pereira *et al.*, Phys. Rev. A **96**, 053856 (2017).

[129] X. Pan *et al.*, Phys. Rev. Lett. **123**, 070506 (2019).

[130] Y. S. Ihn *et al.*, J. Opt. Soc. Am. B **34**, 2352 (2017).

[131] S. Li and J. Wang, Opt. Express **23**, 18736 (2015).

[132] G.-h. Shao *et al.*, Scientific Reports **7**, (2017).

[133] Z. Wang, J. Yang, Y. Sun, and Y. Zhang, Opt. Lett. **43**, 4354 (2018).

[134] Y. Li, Z.-Y. Zhou, D.-S. Ding, and B.-S. Shi, J. Opt. Soc. Am. B **32**, 407 (2015).

[135] J. D. Swaim, E. M. Knutson, O. Danaci, and R. T. Glasser, Opt. Lett. **43**, 2716 (2018).

[136] Y. Hong, Z. Wang, D. Ding, and B. Yu, Opt. Express **27**, 29863 (2019).

[137] H. R. Hamedi, J. Ruseckas, E. Paspalakis, and G. Juzeliūnas, Phys. Rev. A **99**, 033812 (2019).

[138] Z. Amini Sabegh, M. A. Maleki, and M. Mahmoudi, Scientific Reports **9**, 3519 (2019).

[139] R. N. Lanning *et al.*, Phys. Rev. A **96**, 013830 (2017).

[140] H.-H. Wang *et al.*, Phys. Rev. A **100**, 013822 (2019).

[141] H. R. Hamedi, J. Ruseckas, and G. Juzeliūnas, Phys. Rev. A **98**, 013840 (2018).

[142] G. Walker, A. S. Arnold, and S. Franke-Arnold, Phys. Rev. Lett. **108**, 243601 (2012).

[143] A. M. Akulshin, R. J. McLean, E. E. Mikhailov, and I. Novikova, Opt. Lett. **40**, 1109 (2015).

[144] A. Chopinaud, M. Jacquey, B. Viaris de Lesegno, and L. Pruvost, Phys. Rev. A **97**, 063806 (2018).

[145] A. M. Akulshin, D. Budker, and R. J. McLean, J. Opt. Soc. Am. B **34**, 1016 (2017).

[146] J. W. R. Tabosa and D. V. Petrov, Phys. Rev. Lett. **83**, 4967 (1999).

[147] N. Prajapati, A. M. Akulshin, and I. Novikova, J. Opt. Soc. Am. B **35**, 1133 (2018).

[148] A. M. Akulshin, N. Rahaman, S. A. Suslov, and R. J. McLean, J. Opt. Soc. Am. B **34**, 2478 (2017).

[149] A. M. Akulshin, F. P. Bustos, N. Rahaman, and D. Budker, Polychromatic forward-directed sub-Doppler emission from sodium vapour, 2019.

[150] A. S. Zibrov, M. D. Lukin, L. Hollberg, and M. O. Scully, Phys. Rev. A **65**, 051801 (2002).

[151] R. F. Offer *et al.*, Communications Physics **1**, (2018).

[152] Y. Sebbag, Y. Barash, and U. Levy, Opt. Lett. **44**, 971 (2019).

[153] A. M. Akulshin, R. J. McLean, A. I. Sidorov, and P. Hannaford, Opt. Express **17**, 22861 (2009).

[154] J. A. Sedlacek, A. Schwettmann, H. Kübler, and J. P. Shaffer, Phys. Rev. Lett. **111**, 063001 (2013).

[155] J. A. Sedlacek *et al.*, Nature physics **8**, 819 (2012).

[156] A. Horsley *et al.*, Phys. Rev. A **88**, 063407 (2013).

[157] A. Horsley, G.-X. Du, and P. Treutlein, New Journal of Physics **17**, 112002 (2015).

[158] Y. Jiao *et al.*, ArXiv e-prints (2016).

[159] O. S. Mishina *et al.*, Phys. Rev. A **83**, 053809 (2011).

[160] S. M. Iftiquar, G. R. Karve, and V. Natarajan, Phys. Rev. A **77**, 063807 (2008).

[161] S. M. Iftiquar and V. Natarajan, Phys. Rev. A **79**, 013808 (2009).

[162] H. Wang, D. Goorskey, and M. Xiao, Phys. Rev. Lett. **87**, 073601 (2001).

[163] S. Menon and G. S. Agarwal, Phys. Rev. A **61**, 013807 (1999).

[164] A. Lazoudis *et al.*, Phys. Rev. A **83**, 063419 (2011).

[165] C. Zhu, C. Tan, and G. Huang, Phys. Rev. A **87**, 043813 (2013).

[166] J. D. Pritchard *et al.*, Phys. Rev. Lett. **105**, 193603 (2010).

[167] H.-R. Noh and H. S. Moon, Phys. Rev. A **92**, 013807 (2015).

[168] S. Das *et al.*, Phys. Rev. A **93**, 040303 (2016).

[169] S. R. de Echaniz *et al.*, Phys. Rev. A **64**, 013812 (2001).

[170] M. G. Bason, A. K. Mohapatra, K. J. Weatherill, and C. S. Adams, Journal of Physics B: Atomic, Molecular and Optical Physics **42**, 075503 (5pp) (2009).

[171] C. Goren, A. D. Wilson-Gordon, M. Rosenbluh, and H. Friedmann, Phys. Rev. A **69**, 053818 (2004).

[172] Y. Chen, X. G. Wei, and B. S. Ham, Journal of Physics B: Atomic, Molecular and Optical Physics **42**, 065506 (2009).

[173] S. R. Chanu *et al.*, Optics Communications **284**, 4957 (2011).

[174] X.-D. Tian *et al.*, Optics Communications **345**, 6 (2015).

[175] D. Yan *et al.*, Phys. Rev. A **86**, 023828 (2012).

[176] T. Hong, C. Cramer, W. Nagourney, and E. N. Fortson, Phys. Rev. Lett. **94**, 050801 (2005).

[177] K. Pandey, D. Kaundilya, and V. Natarajan, Optics Communications **284**, 252 (2011).

[178] S. Kumar *et al.*, Phys. Rev. A **84**, 023811 (2011).

[179] S. Kumar *et al.*, Phys. Rev. A **88**, 023852 (2013).

[180] Y.-X. Hu, C. Miniatura, D. Wilkowski, and B. Grémaud, Phys. Rev. A **90**, 023601 (2014).

[181] K. Pandey, Phys. Rev. A **87**, 043838 (2013).

[182] M. Khazali, K. Heshami, and C. Simon, Phys. Rev. A **91**, 030301 (2015).

[183] H. Li *et al.*, Phys. Rev. A **80**, 023820 (2009).

[184] M. Manjappa *et al.*, Phys. Rev. A **90**, 043859 (2014).

[185] D. V. Kosachiov, B. G. Matisov, and Y. V. Rozhdestvensky, Journal of Physics B: Atomic, Molecular and Optical Physics **25**, 2473 (1992).

[186] R. K. V. and T. N. Dey, Phys. Rev. A **94**, 053851 (2016).

[187] M. D. Lukin, Rev. Mod. Phys. **75**, (2003).

[188] Hakhumyan, G. *et al.*, Eur. Phys. J. D **66**, 119 (2012).

[189] Sargsyan, A. *et al.*, EPL **110**, 23001 (2015).

[190] E. N. Glezer *et al.*, Opt. Lett. **21**, 2023 (1996).

[191] S. Feng and J. M. Elson, Opt. Express **14**, 216 (2006).

[192] M. Tsang, R. Nair, and X.-M. Lu, Phys. Rev. X **6**, 031033 (2016).

[193] R. Malallah *et al.*, J. Opt. Soc. Am. B **35**, 2046 (2018).

[194] P. W. Milonni and J. H. Eberly, *Laser Physics* (John Wiley and Sons Inc, ADDRESS, 2010).

[195] F. Ladouceur, D. J. Mitchell, and A. W. Snyder, J. Opt. Soc. Am. B **14**, 1768 (1997).

[196] L. Stoyanov, G. Maleshkov, I. Stefanov, and A. Dreischuh, J. Opt. Soc. Am. B **31**, 1159 (2014).

[197] R. D. L. Fuente, A. Barthelemy, and C. Froehly, Opt. Lett. **16**, 793 (1991).

[198] S.-L. Xu *et al.*, J. Opt. Soc. Am. B **35**, 410 (2018).

[199] T. G. Akin, S. P. Krzyzewski, M. W. Holtfrerich, and E. R. I. Abraham, J. Opt. Soc. Am. B **34**, 1286 (2017).

[200] T. N. Dey and G. S. Agarwal, Opt. Lett. **34**, 3199 (2009).

[201] L. Zhang, T. N. Dey, and J. Evers, Phys. Rev. A **87**, 043842 (2013).

[202] H. Shpaisman, A. D. Wilson-Gordon, and H. Friedmann, Phys. Rev. A **71**, 043812 (2005).

[203] O. Firstenberg *et al.*, Nature Physics **5**, (2009).

[204] P. K. Vudyasetu, D. J. Starling, and J. C. Howell, Phys. Rev. Lett. **102**, 123602 (2009).

[205] O. Firstenberg, M. Shuker, N. Davidson, and A. Ron, Phys. Rev. Lett. **102**, 043601 (2009).

[206] S. Sharma and T. N. Dey, Phys. Rev. A **96**, 053813 (2017).

[207] J. A. Andersen *et al.*, Phys. Rev. A **63**, 023820 (2001).

[208] D.-S. Ding *et al.*, Optics Communications **285**, 1954 (2012).

[209] S. R. Chanu and V. Natarajan, Optics Communications **295**, 150 (2013).

[210] Z. Wang and J. Yin, J. Opt. Soc. Am. B **25**, 1051 (2008).

[211] T. Vogt, C. Gross, T. F. Gallagher, and W. Li, Opt. Lett. **43**, 1822 (2018).

[212] H. M. Kwak, T. Jeong, Y.-S. Lee, and H. S. Moon, Optics Communications **380**, 168 (2016).

[213] W. Lee *et al.*, ETRI Journal **39**, 336 (2017).

[214] R. Arora and Z. Lu, IEE Proceedings **141**, 145 (1994).

[215] G. F. Brand, IEEE TMTT **46**, 948 (1998).

[216] G. Turnbull *et al.*, Optics Communications **127**, 183 (1996).

[217] G. F. Brand, IJIMW **21**, 505 (2000).

[218] L. Zhang and J. Evers, Phys. Rev. A **89**, 013817 (2014).

[219] O. Firstenberg *et al.*, Phys. Rev. A **76**, 013818 (2007).

[220] O. Firstenberg *et al.*, Phys. Rev. A **77**, 043830 (2008).

[221] P. R. Berman, J. E. M. Haverkort, and J. P. Woerdman, Phys. Rev. A **34**, 4647 (1986).

[222] S. Singh and G. S. Agarwal, J. Opt. Soc. Am. B **5**, 2515 (1988).

[223] I. Novikova, A. B. Matsko, and G. R. Welch, J. Opt. Soc. Am. B **22**, 44 (2005).

[224] M. A. Kumar and S. Singh, Phys. Rev. A **79**, 063821 (2009).

[225] R. Chrapkiewicz, W. Wasilewski, and C. Radzewicz, Optics Communications **317**, 1 (2014).

[226] R. M. Jenkins, E. E. Mikhailov, and I. Novikova, J. Opt. Soc. Am. B **36**, 890 (2019).

[227] S. Sharma and T. N. Dey, J. Opt. Soc. Am. B **36**, 960 (2019).

[228] H. R. Hamedi, M. Sahrai, H. Khoshsima, and G. Juzeliūnas, J. Opt. Soc. Am. B **34**, 1923 (2017).

[229] K. Islam *et al.*, J. Opt. Soc. Am. B **34**, 2550 (2017).

[230] G. P. Agrawal and D. N. Pattanayak, J. Opt. Soc. Am. **69**, 575 (1979).

[231] Y. Zhou *et al.*, Opt. Lett. **43**, 5263 (2018).

[232] W. Magnus, Communications on Pure and Applied Mathematics **7**, 649 (1954).

[233] T. Kimura, Progress of Theoretical and Experimental Physics **2017**, (2017), 041A03.